BRNO UNIVERSITY OF TECHNOLOGY

VYSOKÉ UČENÍ TECHNICKÉ V BRNĚ

FACULTY OF ELECTRICAL ENGINEERING AND COMMUNICATION

FAKULTA ELEKTROTECHNIKY
A KOMUNIKAČNÍCH TECHNOLOGIÍ

DEPARTMENT OF POWER ELECTRICAL AND ELECTRONIC ENGINEERING

ÚSTAV VÝKONOVÉ ELEKTROTECHNIKY A ELEKTRONIKY

DESIGN AND OPTIMIZATION OF HIGH-TORQUE FERRITE ASSISTED SYNCHRONOUS RELUCTANCE MOTOR

NÁVRH A OPTIMALIZACE FERITY ASISTOVANÉHO VYSOKOMOMENTOVÉHO SYNCHRONNÍHO RELUKTANČNÍHO MOTORU

DOCTORAL THESIS
DIZERTAČNÍ PRÁCE

AUTHOR
AUTOR PRÁCE

Ing. Ladislav Knebl

SUPERVISOR
ŠKOLITEL

doc. Ing. Čestmír Ondrůšek, CSc.

BRNO 2021

Abstract

The high-torque assisted synchronous reluctance machine could be still considered, based on the relatively low amount of publications, as a rather unknown area of research. This and other main advantages, such as low manufacturing cost and a higher torque density of this machine type are driving researchers interest. Even though this machine type has become more interesting in the conventional or high-speed applications, the area of traction applications is slowly getting forward as the machine capabilities are discovered. This thesis is serving just this purpose of developing the ship propulsion driving motor, that is capable of sustaining the high-torque at low-speed. The application is defined by the 55 kW at 150 rpm using the low-cost ferrite magnets aiming to lower final the cost of the machine. The design will be closely tied with optimization algorithms to deliver the best possible performance in the given volume. However the design challenge being difficult task on its own, the thesis is declaring other goals within, that are still very interesting and important. Since the optimization is included in the design process, the first goal, concluding from the given topic is to compare various optimization methods. Not only the two different optimization algorithms, self-organizing migrating algorithm and genetic algorithm, will be compared in the thesis, but even two multi-objective optimization approaches will be compared as well. The preference based and ideal multi-objective optimization techniques comparison will be demonstrated in one optimization scenario with a higher amount of optimized parameters. Other demonstrated goal within the thesis is the comparison of ideal multi-objective optimization with a lower number of parameters. The last goal will be the measurement of the designed and optimized machine, that introduced variety of challenges itself and all of them will be discussed within the last chapter.

Keywords AC machine, Low-speed drive, Synchronous motors, Permanent magnet machine, Finite element analysis, Electromagnetic design, Manufacturing, Measurement, Ferrite, Optimization, Genetic algorithm,

Citation

KNEBL, L. Design and optimization of high-torque ferrite assisted synchronous reluctance motor. Brno: University of Technology in Brno, Faculty of Electrical Engineering and communication, 2021. 91 pages. Supervisor of the dissertation thesis doc. Ing. Čestmír Ondrůšek, CSc. Technical supervisor of the dissertation thesis Ing. Jiří Kurfürst Ph.D.

Pronouncement

I declare that I have written this thesis entitled "Design and optimization of high-torque ferrite assisted synchronous reluctance motor" independently, under the guidance of the advisor and using exclusively the technical references and other sources of information cited in the project and listed in the comprehensive bibliography at the end of the project.

As the author I furthermore declare that, with respect to the creation of this paper, I have not infringed any copyright or violated anyone's personal and/or ownership rights. In this context, I am fully aware of the consequences of breaking Regulation S 11 of the Copyright Act No. 121/2000 Coll. of the Czech Republic, as amended, and of any breach of rights related to intellectual property or introduced within amendments to relevant Acts such as the Intellectual Property Act or the Criminal Code, Act No. 40/2009 Coll., Section 2, Head VI, Part 4.

In Brno _____ _____

author's signature

Acknowledgment

Only one life,
'twill soon be past,
Only what's done
for Christ will last
C. T. Studd

This thesis, as well as the other work that was done during my studies, despite of its current relatively good value, will soon be outdated. What will not deprecate and what is to me of even more value are the character attributes that I've managed to gain or lose and the blessings that I've received not only during the time of studies but also while composing this thesis.
This work, even though it carries my name and a lot of technical data and information, should mainly serve as a proof of the work done by God. He is the provider of the opportunities, strength, courage, patience and the people helping me to achieve the results. Without Him, not a single character would be neither written nor even thought of.
He is the one that should receive all the credit and praise, for He paid for me and also you, dear reader, and now we are able to bring all to Him. He died for us on the cross so we can live and redirect all the glory to Him. He is worthy of all praise!

I'm grateful for the support, insight and help during my Ph.D. studies provided by my supervisor doc. Ing. Čestmír Ondrůšek, CSc. and also technical supervisor Ing. Jiří Kurfürst Ph.D.. I'm honored to be supervised by these inspiring, experienced, smart and hard-working people.
I'm very thankful to the Technology Agency of the Czech Republic and Baumüller company for supporting the development and manufacturing of the electric motor presented in this thesis. Significant impact had a support by the head of the Department of Power Electrical and Electronic engineering doc. Ing. Ondřej Vítek, Ph.D. and other technical staff. Last grateful mention belong to Ing. Viktor Výleta from TM Ratíškovice, for he and the company provided measuring equipment and help during the measurement done in this thesis.

Last but not least I would like to thank to my families for all the support and love shared during the years, when this thesis was composed. Particularly my mother, who supported me financially for many years and encouraged me to finish the work I have started. My gratitude goes to my sister for a lot of funny moments and care and my brother for showing me that hard work has a big significance not only in a job, but also in a personal life. Both blood and spiritual families gain much of a significance to me during the last years. Sincere thank goes especially to my very good friend and a godly man Rosťa Navrátil, that kept me calm with his support, love, prayers and discussions we had on during my studies. It is a blessing for me to know you Rosťa and I'm grateful to God, that we are good friends.

Special thank belongs to my beloved girlfriend Katka, that gave me love and supported me during the last difficult months of my life by prayers and loving attitude. Without her this thesis would lose its quality and some of the meaning.

The last thank belongs to my good colleague but mainly close friend Honza Bárta, who gave me a good base for the machine design but more significantly was a great support and a very good friend. A big thank you goes as well for many laughs and countless precious moments I had during my Ph.D. studies. It was an honor to share an office and our lives together for this period of time.

Contents

List of Figures

List of Tables

1 Introduction

1.1 Motivation

The field of electrical machines has been developing and growing over the last more than a hundred years to a point, where it is practically unimaginable not to use electrical power on a daily basis. Nowadays electrical machines are generating electrical energy in power plants, supplying various home appliances, and with a growing interest in driving electric cars and other commuting vehicles such as scooters, buses, or ships. It almost became easier to find a device powered with electricity, than find a device, that is "man-powered".
Regarding the broad application area of electrical machines, an overwhelming number of machines have been developed during history. The development started with a great interest in current exciting machines and since the 1980s, with the rediscovery of the rare-earth magnet materials which lead to the synchronous machines using a permanent magnet excitation.
New trends are now rediscovered in combining two (or more) types of a motor in one, such an example can be the line-start synchronous machine [1, 2], or combining the electric motor with a mechanical gearbox placed inside [3]. A big interest is also drawn into the machine design for specific applications that are designed to suit industry speed requirements, e.g. high-speed or low-speed. The high-speed machines could be used in applications such as compressors, blowers, or CNC drills. The advantages of high-speed machines are considered to be higher efficiency, higher torque density, and smaller dimensions. Those machines are developed across all machine types, from induction machines [4] through synchronous machines [5–7] to even direct-current machines [8]. The rated speed of such machines is above 10 krpm. Low-speed machines are usually designed in order to develop a high-torque and are used in elevators, pumps, and paper applications. Similar to the high-speed machines, the low-speed machines can be found in various machine types [9–12]. Low-speed machines are considered machines with a speed below 200 rpm. The machines are proportionally bigger, have a high torque-density, unfortunately, have lower efficiency, but are making the gearbox redundant in low-speed drives. Both kinds of machines are shown next to each other in Figure 1.1.

Both kinds of machines can be found in electric vehicles. The high-speed machines are more likely to be used in superchargers [14, 15], while the low-speed machines are used for driving as a part of a drive-train [16] or as an in-wheel application [17].
The thesis is focused on a permanent magnet assisted synchronous reluctance machine as a replacement of a surface permanent magnet in an industrial high-torque low-speed ship propulsion application. Key objectives in the design are the machine dimensions, manufacturing feasibility, and machine cost. The machine will be designed and then optimized by optimization algorithms.
This thesis is structured as follows. Chapter 2 discusses the challenges laying before the syn-

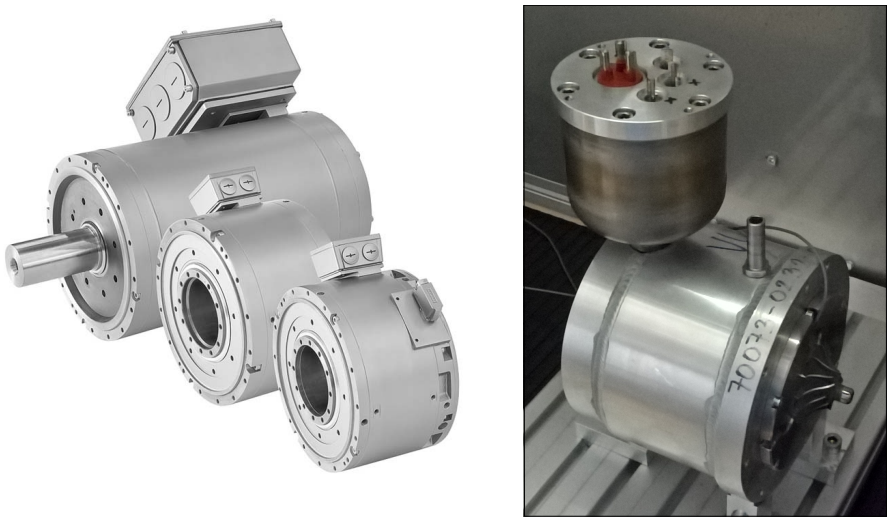

a) b)

Figure 1.1: Examples of a low-speed (a) [13] and a high-speed (b) [4] machine

chronous machines either nowadays or in the near future for machines both with and without a permanent magnets.
The third chapter is dealing with the permanent magnets, principles, history, and the type of magnetic materials used in the electrical machines. Close attention is being paid to the ferrite materials in various applications and then the focus is driven toward the ferrite magnets with the research in the market producers.
The fourth chapter is focused on the synchronous reluctance machines both "pure" (without) and assisted (with) by the permanent magnets. A brief summary of the theory and trends are highlighted along with the paper's research on the traction applications.
The following chapter discusses the optimization algorithms within the theory, the division according to the main principle, and the working principle of the chosen algorithms. A closer look is taken on the algorithms used in the thesis, that is the self organizing migrating algorithm and the genetic algorithm in both preference based and ideal multi-objective optimization.
The practical part of the dissertation of the thesis starts with the sixth chapter and is concerned with the design and research of the ideal slot per pole per phase optimum combination.
Three optimization scenarios are laid down in the next chapter, the first one being the comparison of the preference based and the ideal multi-objective optimization for the one slot pole combination. The second one is the ideal multi-objective optimization of the chosen slot pole combinations and the third one is dealing with the limited optimization scenario, where some restrictions of the optimization are made due to the manufacturing capabilities and the low-cost requirements.
The last chapter is focused on the measurement of the manufactured prototype along with the results, their interpretation, and reasoning. At the beginning of the chapter, the machine control challenges are presented along with the solutions used in the laboratory measurement.

1.2 Thesis goals

The first goal is to present the ferrite magnet's research along with the manufacturing processes involved in the production. To the research of the traction synchronous reluctance machines and to propose the feasible geometry of the ferrite assisted synchronous reluctance machine.
Then to present a manufacturable and ideally optimal solution for the ferrite assisted synchronous reluctance machine. The next goal is to provide the designed machine-measured results and compare them with the finite element analysis results.
The other thesis goals are dealing with the optimization of the machine. The main goal is to compare the self-organizing migrating algorithm with the genetic algorithm in the electrical machines area in both preference based and ideal multi-objective variants.

2 Synchronous machines

In this chapter be the family of the synchronous machines will briefly discussed while the main focus will be on the permanent magnet machines. The current process and challenges of this family of machines as published in the journals and conference proceedings will be concluded.

2.1 Synchronous machine types

The branch of synchronous machines are divided according to the excitation to the three sub-branches as depicted in Figure 2.1.

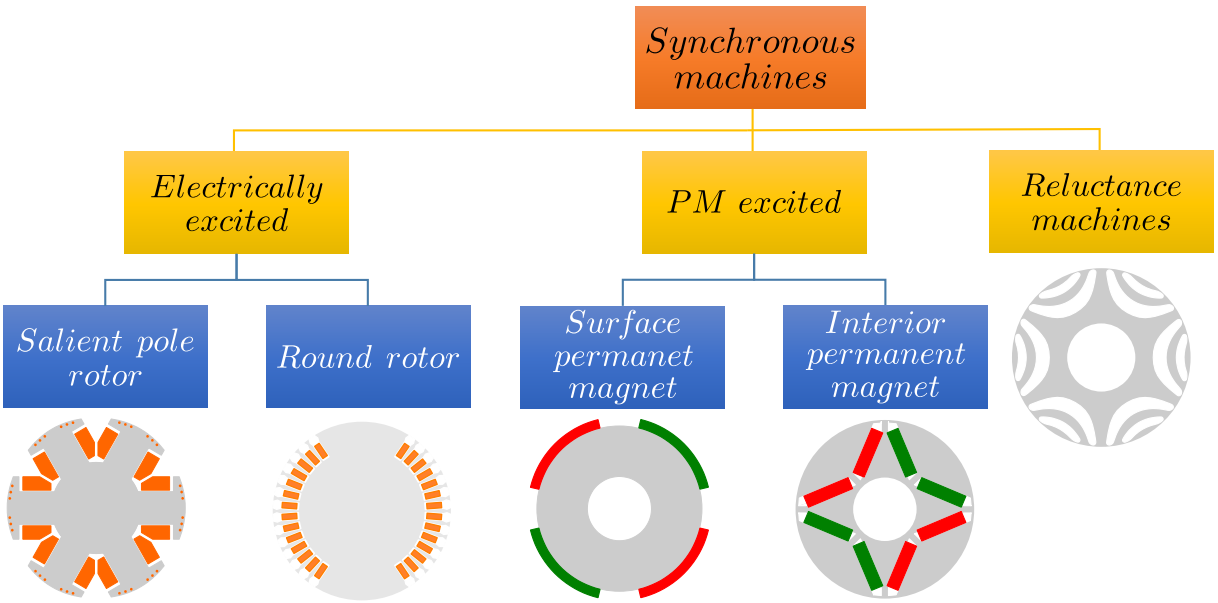

Figure 2.1: Sorting of synchronous machines according to the excitation, adapted from [18].

Hand in hand with the broadening of the application area of the electrical machines (EM) throughout the industry, that was mentioned in the introduction, are the new challenges in the EM design. Nearly every month, the boundaries are pushed further and further across almost all machine types in each machine design perspective (thermal, mechanical, electromagnetic). The branch of synchronous machines is no exception, it has grown from majorly used electrically excited synchronous machines (EESM) to a variety of machines. The general use of the EESM is to generate electrical power in applications such as power plants or cars or in reverse usage (as a motor) in power plants applications (pumping water in hydro plants).
The general use of permanent magnet (PM) excited (PME) machines is on the other hand to

mainly drive the drive train. Although PME machines can be and are with increasing interest used in the power-generating applications [19, 20].

2.2 Synchronous machines design challenges

Regarding the challenges withing the branch of PME synchronous machines can be considered following:

- High torque density machines and gearboxes e.g. Vernier machines [21, 22]
- New PM arrangement and topology such as Halbach arrays [23, 24]
- Line-start synchronous machines (PM and reluctance machines) [1, 2, 25, 26]
- Rare-earth price increase [27]

And those types are described in the following sub-sections.

2.2.1 High torque density machines and gearboxes - Vernier machines

The first of the challenges, that will be discussed in this chapter will be the high torque density machines. This kind of machines is gaining interest, mainly because of the reasons listed in the introduction and are usually designed as a permanent magnet a Vernier machine (PMVE). The vernier machine is a machine, that usually has a high torque density caused by magnetic gearing effect [28]. PMVE has usually two air-gaps, where the iron flux-modulation-pole is inserted between the stator and the rotor as depicted in Figure 2.2. PMVE has two set of pole-pairs - the stator pole-pairs (p) and the rotor p. The p difference creates the magnetic gearing effect, allowing the different electrical and of course mechanical speeds within one machine.

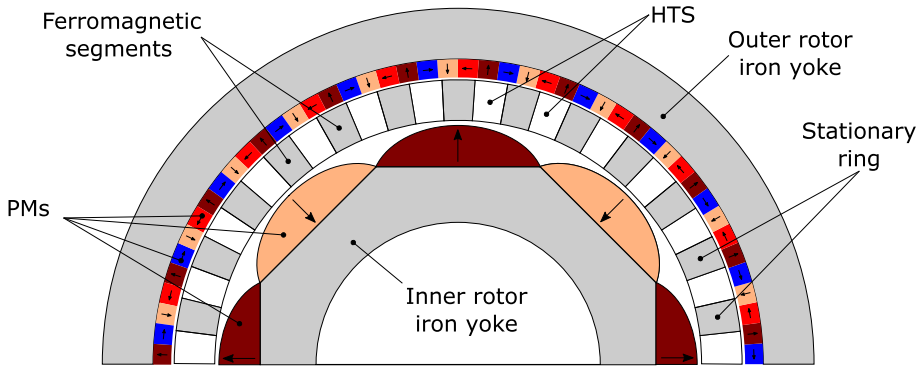

Figure 2.2: Surface permanent magnet Vernier machine with two air-gaps, HTS - High temperature superconductor [28]

PMVE can be found in various PM topologies as a spoke [29], V-shape [30] or surface permanent magnet [28]. And the challenge consists of designing such a machine, that would overcome or at least compensate enough the technological obstacles to a degree, that it would became beneficial to invest resources into the technology. PMVE have also some other drawbacks, beside the manufacturing difficulties, such as a low power factor ($\cos\varphi$), if rare-earth (RE) magnets are not used, no reluctance torque and a high risk of the demagnetization [28].
PMVE are conventionally using the RE magnets, due to above mentioned high demagnetization risk, but lately also some ferrite vernier machines development results have been carried out.

The ferrite versions of PMVE can be found in different arrangements as an outer rotor with one air-gap [31,32] or a spoke inner rotor with one air-gap [33,34] or also as dual-stator ferrite PMVE in [35]. This machine type is along with a increasing interest in specific industry requirements, an exception to show great promises in the future.
It is important to say, that the high-torque machines could be also developed by other types of ferrite machines, such as ferrite assisted reluctance (FASR) machines [36,37], as will be also proved in this thesis.

2.2.2 Special PM arrangement and topology such as Halbach arrays

The second industry PME synchronous machine challenge is the use of the ferrite halbach array (HA) in the electric machine design. The HA is well known phenomenon of a PM arrangement, that decreases the PM flux in the rotor yoke and therefore rotor iron losses. Example of HA arrangement compare with a classical PM arrangement is depicted on an example in Figure 2.3. This type of PM array is used in variety of RE PM synchronous machines from the high-speed [38] through wind turbines [39] to the energy harvesting technology [40]. Publications [41, 42] are providing useful comparison data between the halbach and non-halbach arrays.
Since the HA has been successfully used in RE synchronous machines, it is therefore expected to benefit from its advantages also in ferrite synchronous machines. The ferrite HA arrays were successfully used in various ferrite machine types. The use of HA in ferrite machines allows to increase the loading of such a machine [43], where it was proved on a wind turbine with outer rotor. In [44,45] were RE magnets successfully replaced by a ferrite HA array. Combinations of RE and ferrite HA are used in [46,47] while keeping the same output power and lowering the machine cost.

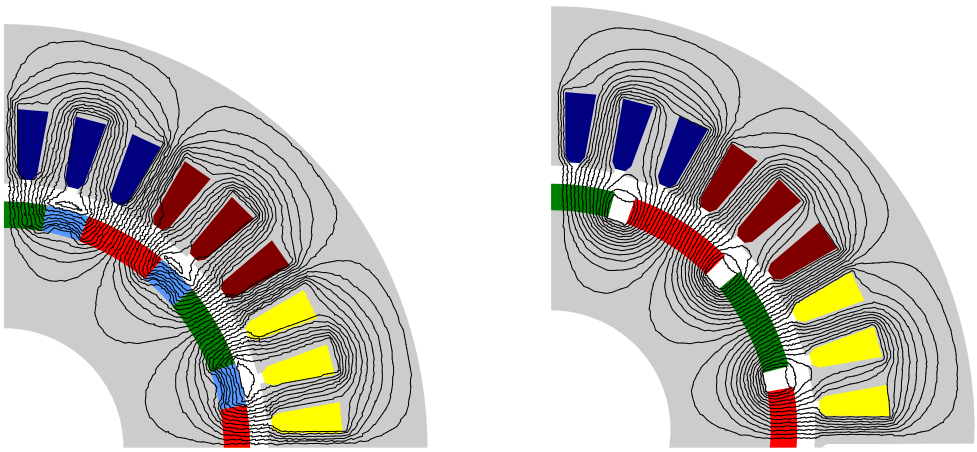

a) b)

Figure 2.3: a) Halbach and b) non-halbach magnet arrangement flux lines comparison

Disadvantages of the HA are higher manufacturing cost, due to the either more challenging PM magnetization or PM assembly. The HA array also presents a big risk of demagnetization for the PM [48,49], the risk reduction is in [49] proposed by the use of a quasi-Halbach arrangement, that is composed of a smaller amount of PM elements. The risk of demagnetization is also mentioned in an impressively useful and well written publication [50] that summarize the critical points of the ferrite machine design. This ferrite PM characteristic is described as the

biggest design challenge. This problem of the ferrite machine design will be addressed later within this thesis.

2.2.3 Line-start synchronous machines

The biggest amount of the energy (almost 40 %) is according to [51] consumed by electric machines, while the most of it is, based on [52], spent by three-phase induction machines (IM). These two facts motivates the electric machine development to either further optimize those machines or propose new machines with higher efficiency, in order to substitute IMs. This is supported by the European union (EU) legislation, where by [53] motors are obliged to meet efficiency requirements of the class IE3 or IE2 (for variable drives) in range 0.75 kW and 375 kW. The new legislation [54] is even more strict, where is required for all motors in range 0.75 kW and equal to or below 1,000 kW to meet IE3 standards by July 2021, respectively IE4 in range 75 kW and 200 kW by July 2024. This legislation also regulates the variable speed drives. One of a Direct-on-Line (DOL) machines, that could eventually replace IMs are Line-start synchronous machines (LSSM). These machines combines two working principles - an asynchronous start-up and a synchronous run at the rated speed.
The LSSM can be further divided in two categories - Line-start permanent magnet synchronous machine (LSPMSM) or Line-start synchronous reluctance machines (LSSRM). Each category in its could be divided again into two categories. LSPMSM could be divided according to the magnet placement either in d-axis (Figure 2.4 a)) or q-axis (Figure 2.4 b)), which could improve or suppress the machine reluctance torque. The LSSRM could be found either with a cage and barriers area divided into separate regions (Figure 2.4 c)) or combining those two regions together (Figure 2.4 d)). The last LSSRM type partially combines squirrel cage and barriers area in Figure 2.4 e). Both LSSM could be developed with a premium efficiency - LSPMSM in [55, 56], LSSRM in [57, 58].

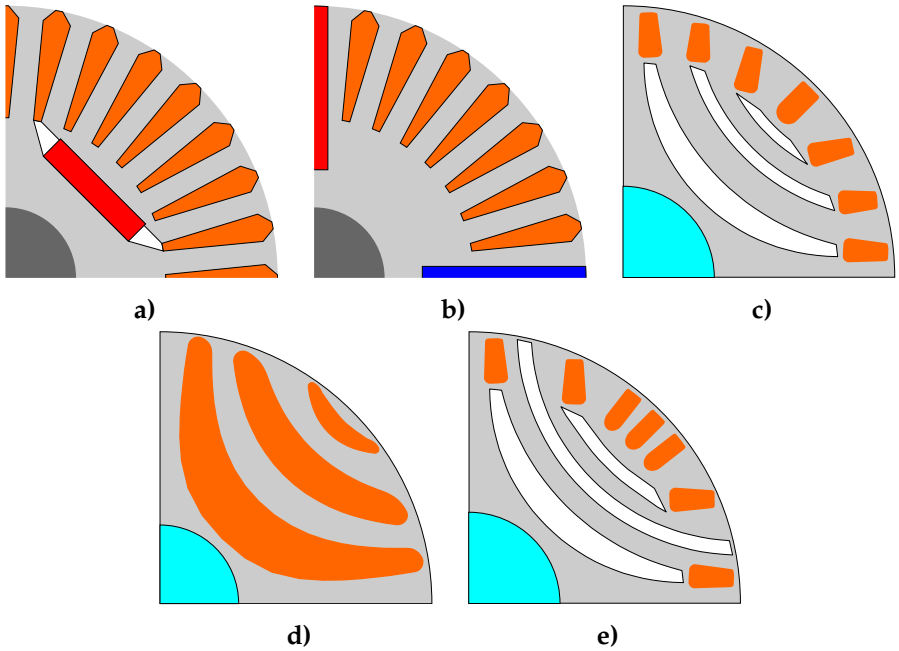

Figure 2.4: Line-start machines overview - a,b) LSPMSM [1] c,d,e) LSSRM

Both LSSM could be found also in a less conventional version such as a LSPMSM two-rotor

machine [59] or as a LSPMSM vernier machine in [60], whilst dual saliency LSSRM is published in [61]. The disadvantages are summed briefly in [55], that mentioned a problematical starting procedure and a higher cost than a IM (due to use of PM). The second disadvantage could be balanced by the use of a LSSRM, while lowering the efficiency [57]. In conclusion both LSSM types shows a great promise for further development.

2.2.4 Rare-earth price increase

The last sub-chapter depicts the RE price problematics that highlight the topic of this thesis. Rare-earth elements (REE) are divided into heavy REE (HREE) and light REE (LREE). In a HREE class are the elements, whose atomic number is between 65 and 71. The elements of terbium, dysprosium and yttrium could be found in this group and could be used for manufacturing of PMs, phosphors and ceramics. The LREE could serve the same purpose plus manufacturing of the battery alloy, LREE consists of the elements with atomic number in range from 57 to 64. The members of this group are as follows: lanthanum, cerium, praseodymium, neodymium, samarium and europium. The rare-earth price of both REE groups are according to [27, 50] highly unpredictable, as is depicted on the price development between the years 2008-2016 Figure 2.5.

The largest portion (36 % according to [62]) of both HREE and LREE oxides could be found in China. The mine production in China went from a monopoly, nearly 87 % in 2014 according to [62] (95,000 tones) to an oligopoly almost 63 % in 2019 [63] (132,000 tones) [64]. The production increase and the market dominance could be explained by the willingness of China accept the associated environmental damage caused by the mining of these materials [27].
Hand in hand with the China mining dominance (even though decreasing) are the financial and political aspects of this dominance. These aspects might be projected into the consideration usage of these materials and might affect the design process of the machine itself. The survey done by [62] in 2019 is depicted in Figure 2.6.

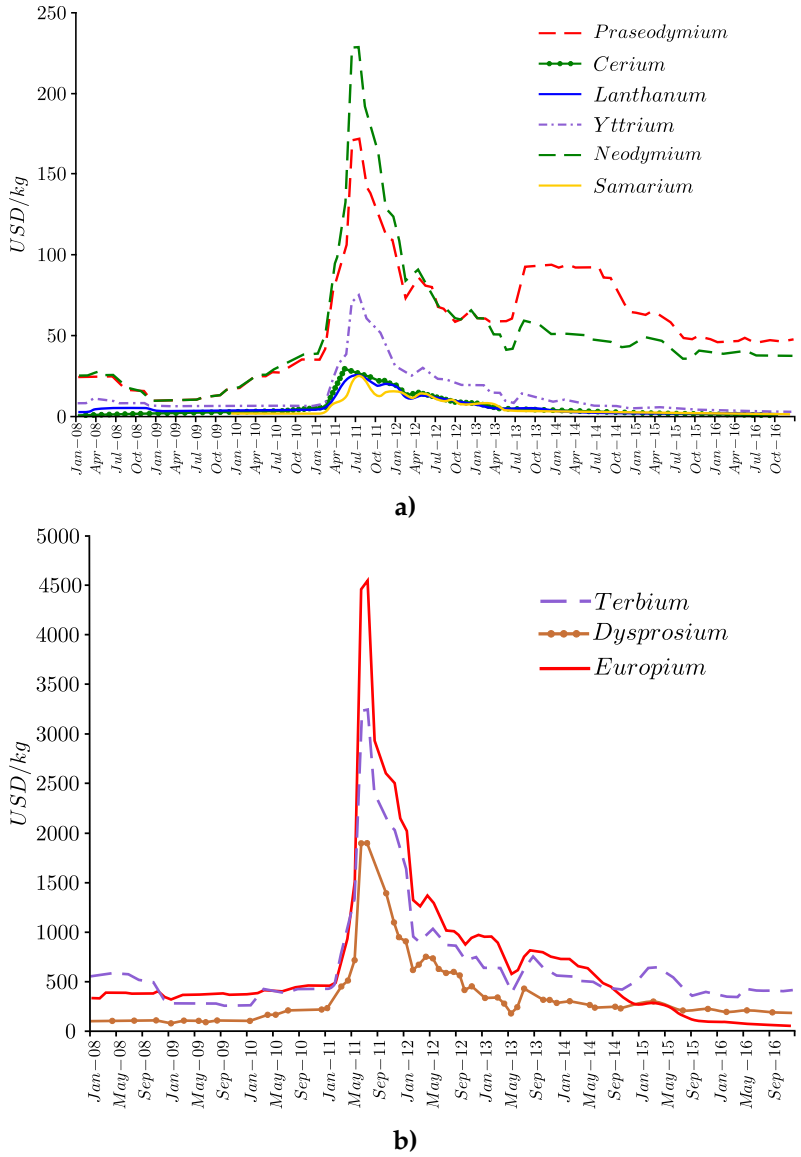

Figure 2.5: Shanghai SteelHome nominal prices of some RE oxides between early 2008 and late 2016. a) LREEs plus yttrium. b) HREEs plus Europium, vectorized from [27]

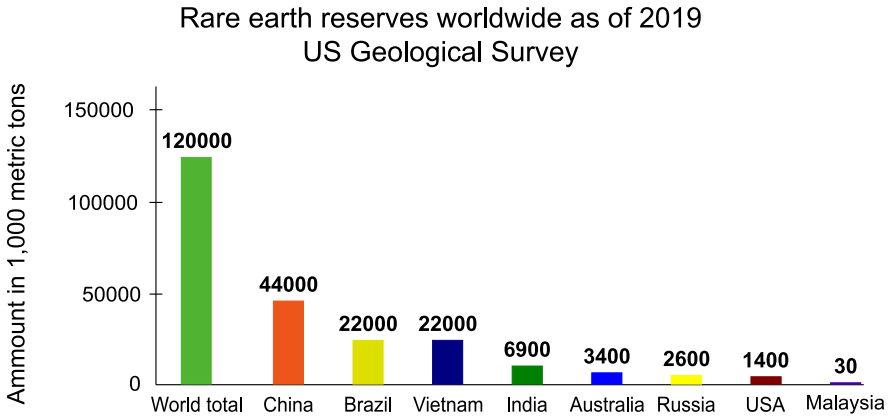

Figure 2.6: Neodymium resources of each major mining country [62]

3 Permanent magnets

This chapter will introduce the ferrite magnets among other magnet types. Types of ferrite magnets will be also introduced in this chapter with the significant characteristics. The chapter will start with a broad overview and finish with a practical application along with the design risks.

3.1 Description and history

The purpose of PM is to store a magnetic field in a particular volume. The PM is in general manufactured from a metal alloy, capable of sufficiently storing magnetic field energy. The energy is put in the material part at the manufacturing process (AlNiCo) or in the process called magnetizing. If handled properly, the magnetic energy stays in the PM ideally for an unlimited amount of time (the magnetism is permanent) [65, 66].
PMs have come a long way from the first large measurement of magnetic susceptibility of a large number of substances over the dimensions of temperature done by Pierre Curie in 1895. The PM application has broadened from a simple needle of a magnetic compass to the key elements of various home applications, industry, automotive, or even space exploration. It is clear that in this period, nearly 130 years long, a lot of inventions and breakthroughs were made. Various metal alloys were discovered, new more efficient ways of magnetizing and processing these materials were researched and new applications with PM adaptation were invented. The evolution of both energy density and coercivity of the PMs in the 20th century, that depicts the PM development and improvements in this field are shown in both sub-figures in Figure 3.1 [65].

3.2 Permanent magnet operation point

As mentioned above, the PMs store the magnetic energy after the magnetization process. After PMs are inserted into the magnetic circuit, their working point is set based on the magnetic circuit properties. Simple BH curve, not considering demagnetization field, of solenoid in the magnetic circuit consisting only of an air-gap is depicted in Figure 3.2.

Firstly the PM is magnetized by the field strength (H), H_1 precisely, that is after the magnetization removed, creating the magnetic flux-density B. The PM then starts to insert the magnetic field into the circuit and the working point is determined by the intersection of the BH loop and the load line C. The slope of the load line is set by the circuit designer and depends on the magnetic circuit properties. The best working point of the circuit is located, where the PM is able to deliver the highest energy product BH. Therefore the maximum BH product, conventionally

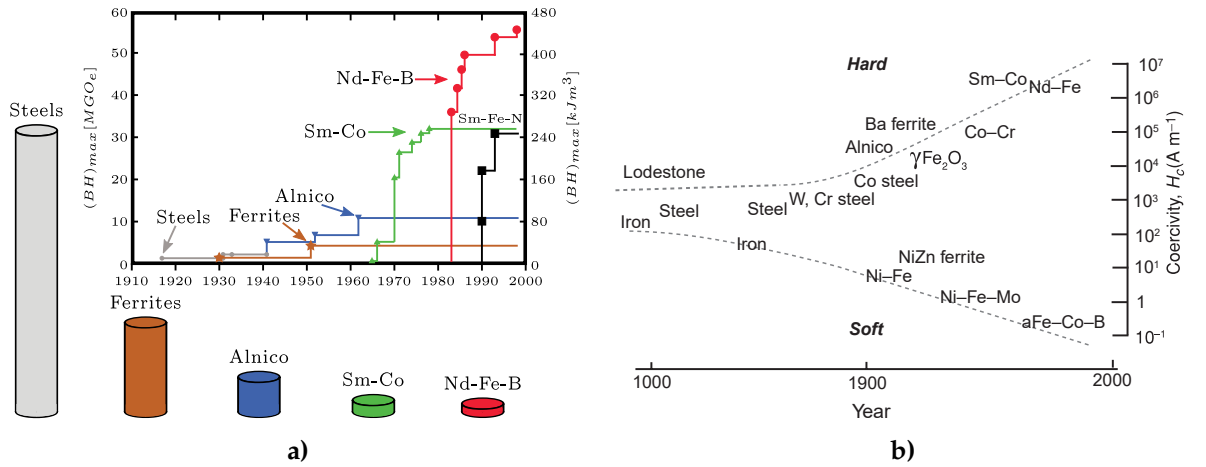

Figure 3.1: a) the PM energy density development, cylinders represent the required volume to store a certain amount of energy and [67] and b) the coercivity in hard and soft PM materials in the 20th century [68]

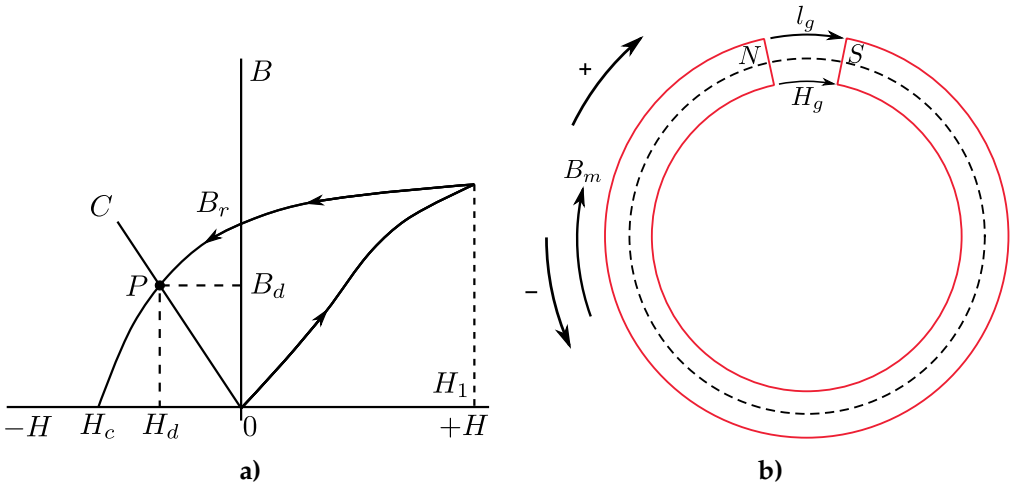

Figure 3.2: a) the example of an operating point of a solenoid and b) a sketch of the magnetic circuit [65]

labeled as BHmax, is usually considered as one of the most important objectives while selecting the PM. The other could be the Curie temperature or the corrosion resistance.
It is important to mention, that in a non-ideal case the flux-density in a material is defined by (3.1)

$$B = \mu_0 M + \mu_0 H. \tag{3.1}$$

Where M is a magnetization of the PM and H is the magnetic field strength, both in $\mathrm{A \cdot m^{-1}}$. It is obvious, that in the case of soft magnetic materials, where range of H is very low, the second part of this equation is negligible. The hard magnetic materials are usually working at much higher field strengths (above $1\,\mathrm{kA \cdot m^{-1}}$), therefore the $\mu_0 H$ part is much bigger. The comparison of normal and intrinsic ("natural") magnetic curves are depicted in Figure 3.3.

Taking a closer look at Figure 3.3, two details could be mentioned. The first one regarding the remanent flux-density B_r, remains the same in both inductions. This comes from the equation 3.1, where location of B_r is where H equals zero, thus only the first part of equation $\mu_0 M$ gives a non-zero value. The other detail is the difference between the intrinsic coercive force H_ci and

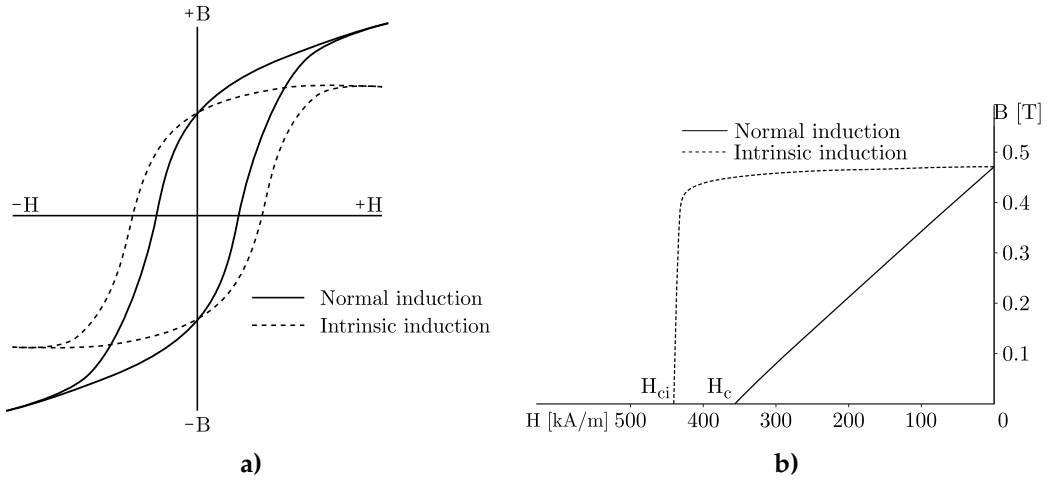

Figure 3.3: a) Difference between normal and intrinsic curves in PM material [69] and b) more detailed view of ferrite Hitachi NMF-15J permanent magnet's BH loops in second quadrant [70]

the normal coercive force H_c. The amount of decrease, which is 80.463 kA $\cdot$ m^{-1} in the case of NMF-15J, is given mainly by the properties of the PM material.
Catalog values of the intrinsic and normal curves are depicted in different units. The typical BH curve values, that are mostly used in a finite elements analysis (FEA) as the input material properties are a flux-density B in Tesla (T) and a magnetic field strength H in kilo-Ampere per meter (kA $\cdot$ m^{-1}). These units are also defined as SI units. Some manufactures are also providing data of a flux-density in Gaussian units as Gausses (G) and Oersteds (Oe), respectively their modifications as kilo-Gausses (kGs) and kilo-Oersteds (kOe). The relationship between SI and Gaussian units, seldom called Gaussian-cgs units or cgs-units is $B_{\mathrm{SI}} = \frac{B_{\mathrm{Gaussian}}}{10000}$ for flux-density and $H_{\mathrm{SI}} = \frac{1000}{4\pi} \cdot H_{\mathrm{Gaussian}}$ respectively for magnetic field strength.

3.3 Permanent magnet alloys

As mentioned above, the PM materials took a big leap in the 20th century. Through this development period, various metal alloys were both invented and overcame by the new and perspective materials. After all, in the 21st century, it comes down to the four groups of the PM materials in various alloy combinations within those groups. The four alloys are - AlNiCo, Ferrites, Samarium-cobalt (SmCo) and Neodymium-iron-boron (NdFeB). The typical BH curves of each PM alloy are depicted in Figure 3.4.

The examples of each PM alloy in various shapes are shown in Figure 3.5.

The PM alloys beside ferrites will be included in the following subsections. Since the ferrites will be used in the machine design, the whole sub-chapter will be dedicated to this PM alloy taking a closer look at the manufacturing and important characteristics.

3.3.1 Alnico magnets

The AlNiCo magnet alloy name is based as an acronym of the elements chemical symbols Aluminum (Al), Nickel (Ni) and Cobalt (Co). This alloy composition was firstly discovered by the Mishima in Japan in 1931, specifically 58 % iron (Fe), 30 % Ni, and 12 % Al had a coercivity of

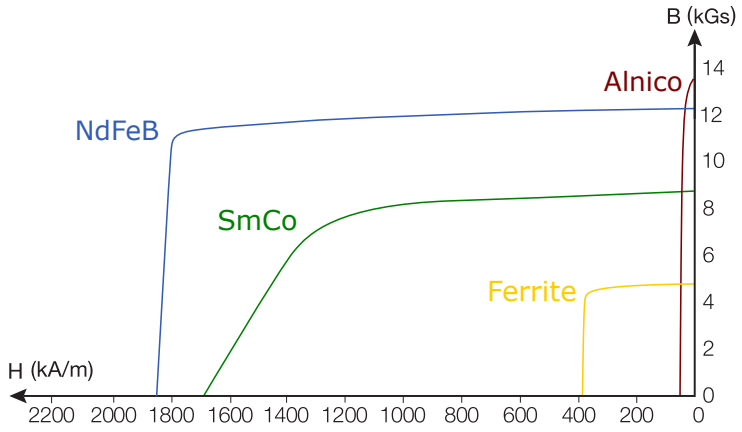

Figure 3.4: The examples of PM BH curves, Neo3520 is labeled as NdFeB, SmCo 18 is labeled as SmCo, Cast AlNiCo 5 is labeled as AlNiCo, all three are from Adams Magnetic Products [71], NMF-15G from Hitachi Metals is labeled as [72]

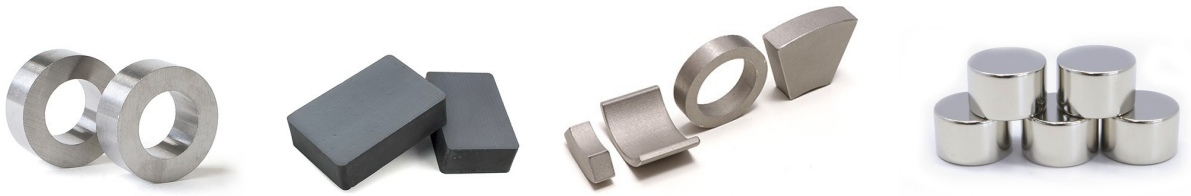

a) **b)** **c)** **d)**

Figure 3.5: Overview of magnets, a) AlNiCo magnets [73], b) Ferrite magnets [70], c) SmCo magnets [74] and d) NdFeB magnets [75]

over 400 Oe [65]. AlNiCo magnets are very hard to process at low temperatures, thus are either sintered or cast with a specific process involving also some light magnetization of the material. Sintered magnets usually have worse magnetic properties, as depicted in Figure 3.6.
According to [65, 71] AlNiCo has relatively high remanent flux-density, Curie temperature and resistance to corrosion, the low-temperature dependence of magnetic properties around the room temperature and the PM cost is also low. The AlNiCo magnets suffer from a low coercivity force, which limits the use of this material in the electric machine design. The AlNiCo magnets are according to [76] used for microphones, sensors, and in the aerospace industry.
The large research and development interest in the AlNiCo magnets has slowly decreased since the 1970s with the discovery of new RE materials. Even though the interest has decreased, the magnets are still offered by the large manufacturers [71, 73, 77]. Nowadays AlNiCo magnets are, in an example from Eclipse magnetics manufacturer, reaching maximum values of BHmax product around 80 kJ/m^3 [78].

3.3.2 Samarium Cobalt magnets

The samarium cobalt (mostly known as SmCo) magnets are one of two RE alloys widely used in industry applications. The SmCo alloy could be found in $SmCo_5$ or Sm_2Co_{17} compounds, while the order reflects the development stages and Sm_2Co_{17} or its variations are preferred nowadays. The SmCo magnets were, according to [65] the first ones to achieve an energy product of 20 MGOe ($\sim$ 160 kJ/m^3). SmCo magnets benefits from two phenomenons, i.e. easy magnetization and a high Curie temperature.

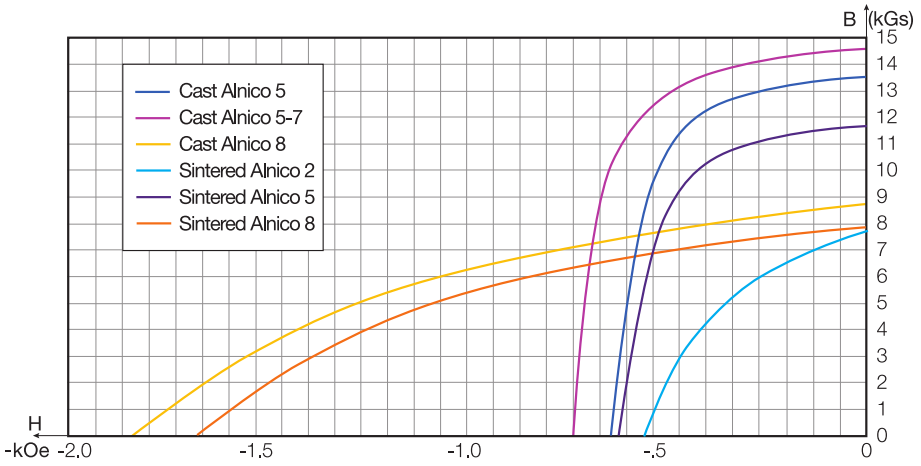

Figure 3.6: AlNiCo second quadrant BH curves [71]

The first benefit comes from the fact, that after the magnetization $SmCo_5$ domains create domain walls during nucleation, which prohibits the material from a demagnetization. In the case of Sm_2Co_{17} the alloy is the demagnetization resistivity caused by the domain wall pining. The domain wall is a thin barrier between magnetic domains [65]. A disproportion between the magnetizing curve in the first quadrant (magnetizing energy) and the second quadrant, where the magnet has it's an operating point is depicted in Figure 3.7.

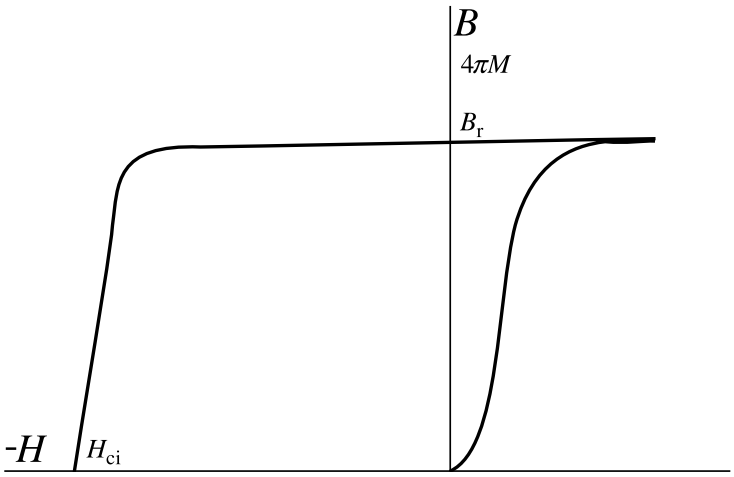

Figure 3.7: SmCo easy magnetization process [65]

According to [79], the SmCo magnets also benefit from the high temperature stability and can be used in extremely cold and hot temperatures. The same source claims, that SmCo magnets are more expensive than NdFeB magnets and are more prone to a corosion. The Arnold Magnetics Technologies [80] is considered to manufacture the top quality of SmCo magnets peaking with energy product at 33.3 MGOe($\sim$ 265 kJ/m^3). BH curve of this manufacturers SmCo magnet is presented in Figure 3.8. The SmCo magnets are widely used in aircraft applications [81, 82], where the temperature varies in great intervals between temperatures below 0 °C and well above 200 °C and in other temperature varying applications as mentioned in [79] or [83].

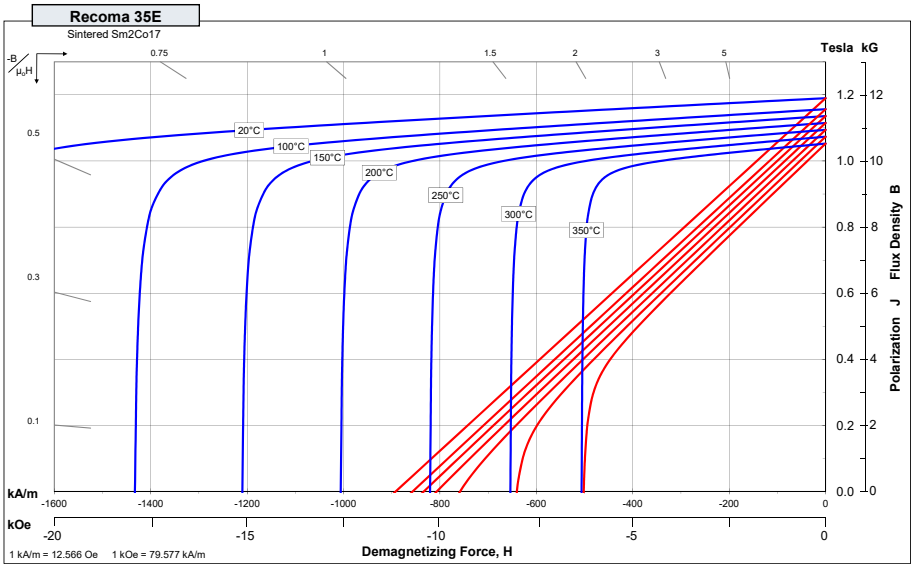

Figure 3.8: BH curve of the high energy product RECOMA magnet from Arnolds [80]

3.3.3 Neodymium magnets

The second widely used rare-earth alloy in industrial applications is the neodymium-iron-boron (NdFeB). This alloy was found in order to find a better and cheaper alternative to the SmCo magnets. It was discovered according to [65] as $Fe_{14}Nd_2B$ by Special Metals Co. in Japan in 1984. The method of manufacturing this compound is very similar to the one used in $SmCo_5$. As the industry applications prove today, the replacement of SmCo magnets with NdFeB was successful mostly in conditions below 200 °C.
The NdFeB elements could be according to [65] altered with other elements resulting in an increase of the Curie temperature and the temperature stability (Co replaces some Fe), the increased coercivity, and the lower magnetization (Nd replaced by other heavy rare-earth elements, usually dysprosium). The NdFeB magnet energy products according to [65] are usually in the range from 20 to 40 MGOe, but nowadays the energy products above 50 MGOe are not exceptions. The largest manufacturer the Eclipse magnetics, the Adams Magnetics and the Arnold Magnetics offer their highest grades of NdFeB magnets with energy products 50 MGOe [84], 54 MGOe [71] and 55 MOGe [85] respectively.
The biggest advantages according to [65,71] are the price (compared to SmCo magnets) and the highest energy products among the other PM materials.
The disadvantages according to the same sources are the relatively low Curie temperature (usually below 300 °C) and therefore the high dependence of magnetic properties on temperature and the corrosion proneness of the magnets. PMs are therefore equipped with some kind of protective coating, which is made of Ni-Cu-Ni plating [84]. The standard neodymium magnet BH curve and its temperature dependency from [71] is depicted in Figure 3.9.

3.4 Ferrites

The conclusion of the previous section 3.3 section could be that there is no clear choice of a PM. Considering all the conflicting objectives, such as the price, the energy product, the Curie temperature, and the corrosion resistance, the decision process becomes indeed complicated.

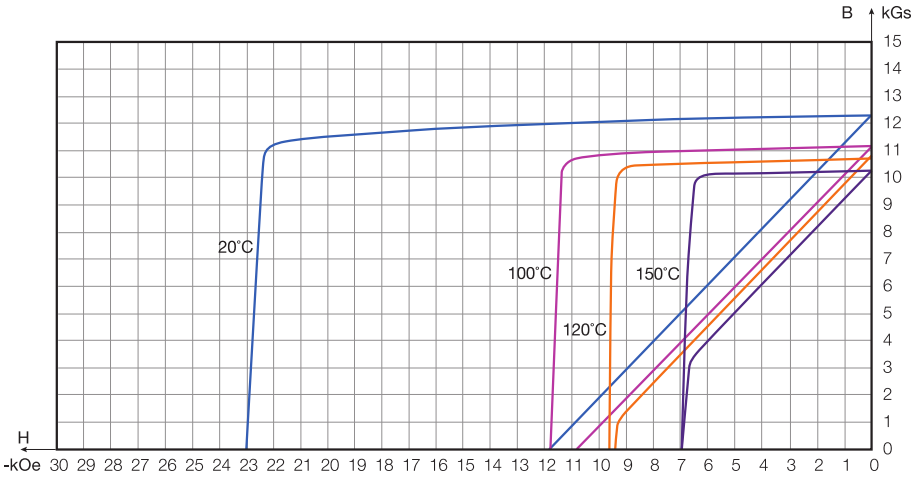

Figure 3.9: NdFeB Neo3520 from Adams, second quadrant BH curves [71]

Even though the best PM alloys are keeping to increase the energy products, the focus is still redirected towards the lower-energy PMs - Ferrites. That is mostly due to the price, that remains, according to [86], only a portion of the RE alternatives.
It is the last alloy mentioned at the beginning of the 3.3 section, the ferrites, that have been chosen for the machine design. There are many categories of ferrites with various applications. Figure 3.10 was presented to clarify the categories containing also the most significant applications. The manufacturing process, manufacturers, and various types of ferrite magnets, all in a hexagonal ferrite category, will be described and listed in the next subsections. It is worth noting, that in this work it is referred to the hexagonal ferrite magnets as ferrites, which is a commonly used term in literature in a field of EM design.

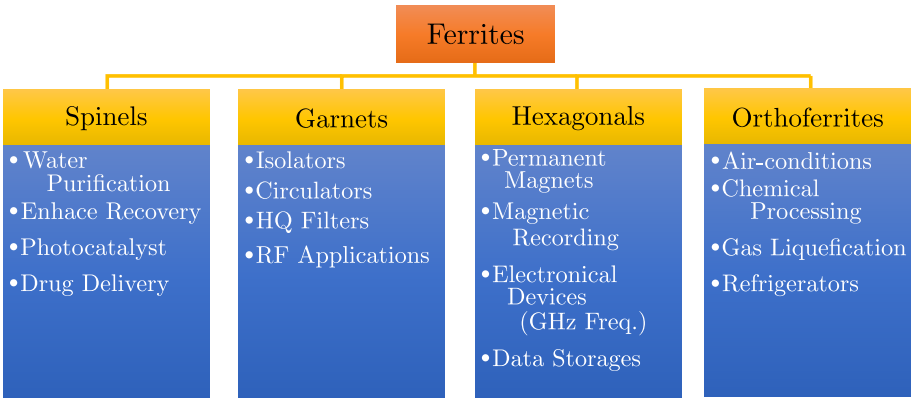

Figure 3.10: Ferrites overview with applications - photocatalysts [87], electronic devices [88,89], hexagonals [90] and air-conditioners/ conditioning [91]

3.4.1 Hexagonal ferrites

As was foreshadowed in the introduction, the hexagonal ferrites are a group of a bigger family of ferrite materials. This group is characterized by the hexagonal crystal structure composing of Fe_xO_y, where x and y refer to a number of atoms in the composition. Hexaferrites, as is seldom referred to the hexagonal ferrites, became very important in various applications and according to [92] over 300,000 tones of the M-type barium hexaferrite (BaM) was globally

manufactured per year. The hexaferrite magnetic properties are all influenced by the crystalline structures and magnetically all the hexaferrite are ferrimagnetic.
As stated in [93] the most important hexaferrites from the perspective of storing the magnetic energy BaM and SrM M-type barium hexaferrites, initially named ferroxdure and M-type strontium hexaferrite. The BaM ferrite was first described in 1925 [94], while the crystal structure was deduced in 1938 [95]. As reported in [93] - the BaM and SrM hexaferrites are very similar from the magnetic perspective and have a very similar crystaline structure. The [96] claims SrM to be slightly lighter with a molecular mass of 1062 g and a mass density equal to 5.11 gcm^{-1} compared to 1112 g and a mass density equal to 5.28 gcm^{-1} of the BaM.

3.4.2 Ferrite manufacture process and research

The ferrite manufacture process is very complicated and involves many procedures involving high-temperature heating of the material. The M-type hexaferrite as a major product of the heating process is manufactured, according to [93], by processing in temperature ranges between 800 and 1200 °C. As stated in [93], there are 12 synthesis methods of specific ferrites plus one method that is used in the industry.
The industry processed M-type ferrited can be obtained from raw materials (α-Fe_2O_3), as stated in [93], as well as from recycled materials depicted in [97, 98], obtaining a BaM ferrite with very good characteristics.
The BaM can be drily milled, which unfortunately results in sacrificing the H_c and the M_s decreasing over the milling time, because it induces stress into the powder and formulates a magnetically weak BaO. The second phenomenon can be lowered by the milling in the low oxygen pressure. Wet milling results in a stress-free powder, with a longer milling time the H_c increases, and the M_s decrease is minimized by adding surfactants fo the liquid [99]. The ball milling is also successfully used, as presented in [100].
Ceramic ferrites, usually granulated (with good results by a vacuum hot steam process) doted with a small amount of calcium pressed in an external magnetic field and then sintered. The SrM powder is added into the powder, achieving a higher B_r, as proved in [101]. BaM ferrites have a high Curie temperature around 450 °C and a relatively high maximum coercivity of 594 $kA \cdot m^{-1}$, reaching nearly half of it by a standard ceramic preparing procedure (max. 255 $kA \cdot m^{-1}$), but not getting much higher with other synthesis methods (at the same temperature). This is due to the relatively large grain sizes of the materials. Great research has been done in a field of BaM ferrites resulting in relatively high both coercivity and magnetization values [98, 102, 103] at very small grains, but more importantly at high temperatures.
The SrM ferrites have a slightly higher Curie temperature around 470 °C and a slightly lower maximum coercivity at 533 $kA \cdot m^{-1}$, achievable with polycristalline samples, published in [104]. With a standard ceramic procedure value of 286 $kA \cdot m^{-1}$ could be achieved, as provided in [105]. Similarly to the BaM ferrite, a big research has been done and much higher magnetic properties are achieved at higher temperatures [106–108].

3.4.3 Temperature influence on ferrite properties

The basic principles and properties of ferrites are mentioned in the previous sub-chapters. There are still many properties of ferrites, that are influencing the ferrite properties and are therefore needed to be included in the development process of machines using ferrites as a PM. The most important property is the temperature influence on the magnet characteristic.

As depicted above (in case of SmCo and NdFeB magnets), the BH curves of PMs are varying with the temperature (Figure 3.8 and Figure 3.9) and both the coercitive force and the remanent flux-density are increasing with the decreasing temperature (having negative temperature coefficients) as depicted for both the SmCo and the NdFeB in Figure 3.11.

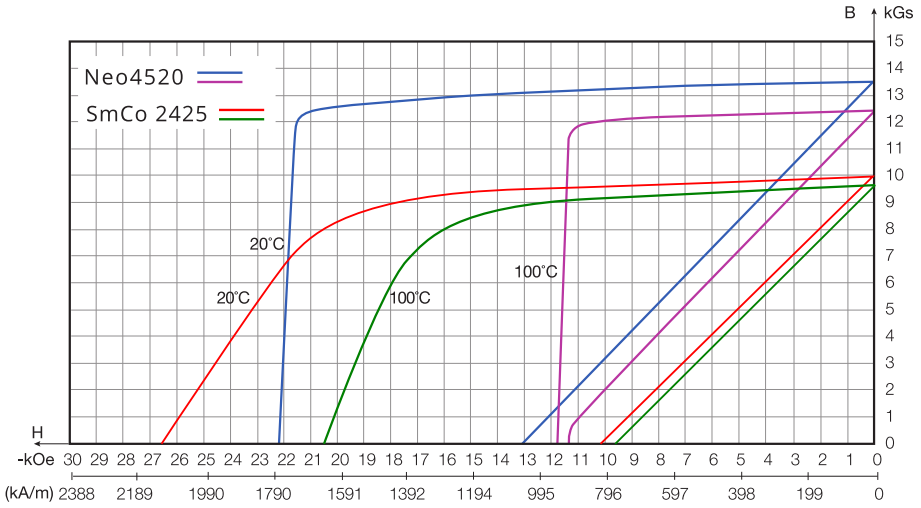

Figure 3.11: The influence of temperature on RE permanent magnets [71]

In the case of RE magnets, the phenomenon can be explained by a faster and more sporadic movement of particles within the atomic structure. Therefore the RE magnets are easier to demagnetize at higher temperatures.
The ferrite magnets behave differently. The temperature coefficient of the remanent flux-density is negative (decreasing flux-density with increasing temperature), but the temperature coefficient of the coercive force is positive (increasing with rising temperature). This fact is making ferrite magnets more prone to demagnetization at lower temperatures and decreasing the possible demagnetization at higher temperatures. The BH curve temperature shift is shown in Figure 3.12.

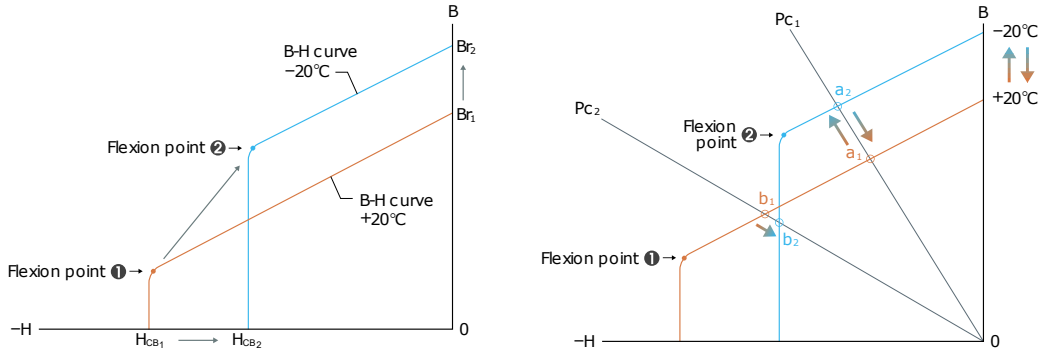

Figure 3.12: The influence of the temperature on ferrite permanent magnets [109]

3.4.4 Commercial ferrite magnets

Regarding the commercially offered ferrite magnets, there has been a greater demand increase over the years. The biggest ferrite manufacturers, according to the research of the commercially presented data-sheets done by the author are following in alphabetical order:

- Adams
- Dura
- Eclipse
- Hitachi
- Mahindra
- Spacemagnets
- TDK

Data from a data-sheet of each manufacturer was gathered and the range of magnet energies delivered by each manufacturers was found. Since around 120 magnet types from all manufacturers were found, only the ranges of magnet energies are depicted in the Figure 3.13.

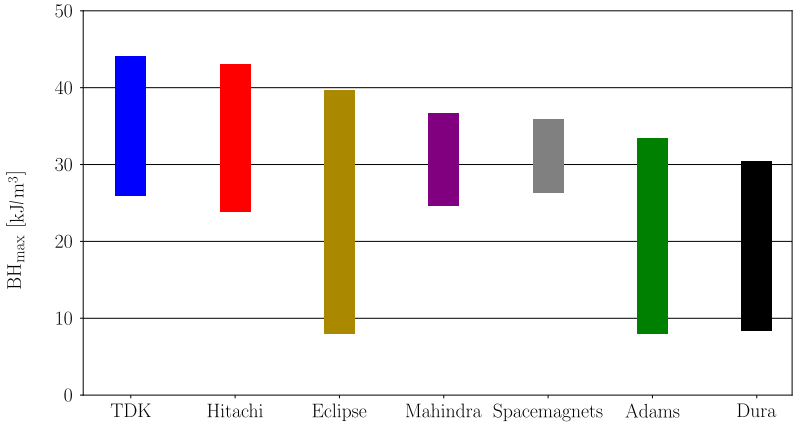

Figure 3.13: The comparison of the stored magnetic energy ranges of the commercially offered ferrite magnets.

The ferrite magnet with the highest energy of each manufacturer is listed in Table 3.1 along with other properties and information about the material and process, if listed by the manufacturer.

Table 3.1: The comparison of ferrite magnets

Mnf.	**Type**	B_r **[T]**	H_c **[kA/m]**	BH_{max} **[kJ/m^3]**	**Material**	**Process**
TDK	FB13B	0.475	340	44	La-Co SrM.	Thin-shape
Hitachi	NMF-15G	0.485	362	43	-	-
Eclipse	Y40	0.45	342	39.65	SrM	-
Mahindra	CB 8B	0.44	246.5	36.6	Anisotrop SrM	Wet
Spacemagnets	HTY-45E	0.425	324	34.25	-	-
Adams	Ceramic8c	0.43	214	33.4	SrM	-
Dura	Ceramic 8B	0.40	240	30.4	-	-

Even though not all the materials and processes are listed in the data sheets, it is reasonable to assume, that strontium ferrites are most likely being used in most of the listed magnet samples, since the SrM material has (as mentioned above) stronger magnetic properties.
Out of the compared manufacturers and magnet types, the best manufacturers seem to be TDK and Hitachi with their high coercive force, remanent flux-density, and also magnet energy. As an interesting factor could be pointed out, that even though TDK magnet has lower B_r and H_c, its stored energy is listed to be higher than the best Hitachi ferrite magnet.

4 Synchronous reluctance machines

The two versions of synchronous reluctance machines will be presented in this chapter and compared with respect to the torque and power factor. This chapter also contains brief research of the current state of the synchronous reluctance and permanent magnet-assisted synchronous reluctance machines.

4.1 Pure synchronous reluctance machine

The synchronous reluctance (SynRel) machine, a predecessor of a PMASR machine, was firstly developed and published by J.K Kostko in 1923 reporting very poor performance characteristics e.g. the efficiency, the torque ripple and the cos φ [110].
The SynRel is a machine, where the torque is developed by the intentionally designed magnetic saliency ξ between the direct (d) and the quadrature (q) axes of the machine. Nowadays, a machine benefits from high efficiency, a very low manufacture cost, good manufacture feasibility, but is still hindered by a low cos φ and a low torque density per volume (TRV).
The first possible solution, that could lead to the minimization of conventional SynRel machine drawbacks, mainly the low torque-density and cos φ, was the proposal, of a fluid geometry in [111] used for example in [7] or [112]. The flux-barrier shape comes from a flux-lines distribution in a solid iron while supplying the winding with q-axis current only as depicted in Figure 4.1.

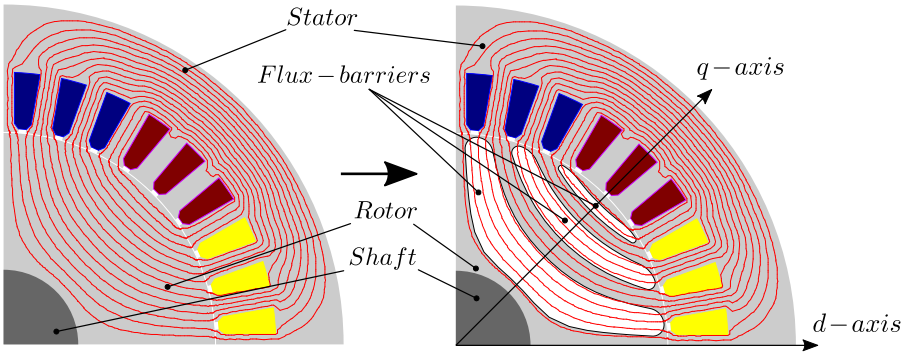

Figure 4.1: Fluid geometry generation with the d-axis and q-axis alignment, firstly published in [111].

In SynRel machine the torque is developed, as mentioned above, by the rotor magnetic saliency. The magnetic saliency is defined by the equation (4.1)

$$\xi = \frac{L_{\mathrm{d}}(i_{\mathrm{d}}, i_{\mathrm{q}})}{L_{\mathrm{q}}(i_{\mathrm{d}}, i_{\mathrm{q}})} \tag{4.1}$$

, where the inductances in the direct L_d and quadrature L_q axes depend on the currents applied in the both axes but also on the magnetic reluctance in each axis, which is delivered by $L_{d,q} = \frac{N^2}{R_{md,q}}$. Where the N is number of turns and the R_m is the magnetic reluctance of the circuit in corresponding axes. Which is more easily shown in the reluctance networks [113] or in an analytical model [114]. By using the fluid geometry, the reluctance in the d-axis is lower, because the flux-lines are distributed equally and naturally, while increasing the d-axis inductance. In the q-axis it is the exact opposite, the reluctance in the q-axis is increased by the placement and the shape of the flux-barriers causing the smaller inductance in the q-axis path. The magnetic saliency increase results in the cos φ and torque increase, that are estimated by the equation (4.2) and (4.3) respectively [115].

$$T = \frac{3}{2} p (L_d - L_q) i_d i_q \tag{4.2}$$

$$\cos \varphi = \frac{\xi - 1}{\xi + 1} \tag{4.3}$$

The second is to mitigate the SynRel machine drawbacks by the introduction of the PMs into the rotor geometry. This solution will be discussed in the next section.

4.2 Permanent magnet assisted synchronous reluctance machine

The PMASR machine is considered to be a hybrid between a pure reluctance machine (without a PM) and the interior permanent magnet (IPM) machine. The rotor of such a machine is excited by the PMs, but the main part of the developed torque, if the low-energy magnets are used, still comes from the rotor saliency. The PMs are inserted into the flux-barriers (see Figure 4.2) and are usually fixed by the iron bridges (ribs), or by other designed iron segments as shown in Figure 4.2. The last commonly used PM configuration in the PMASR topology is to insert the PM also in the barrier sides and fix them with the iron segments similar to type shown in Figure 4.2 b). The use of the PM is twofold, firstly the PM flux develops an electromagnetic torque and the second is the machine cos φ increase.

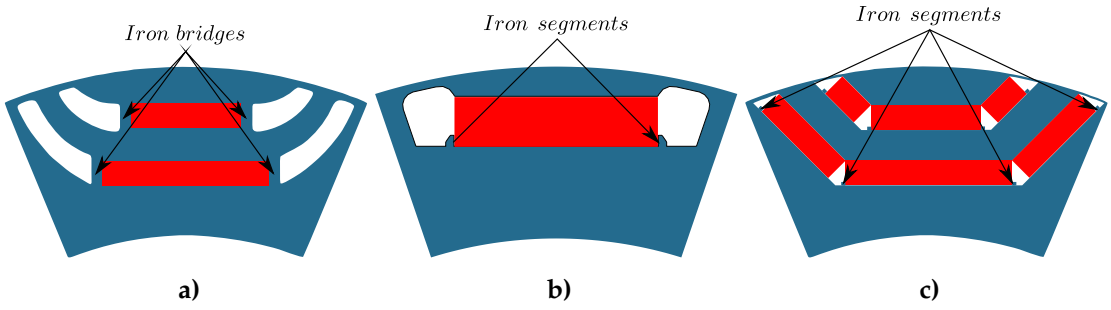

Figure 4.2: Examples of the PM mechanical fixation within the PMASR geometry

The portion of torque, that is developed by a PM in the PMASR machine depends on the PM-flux, or the type of magnets (neodymium based magnets, ferrite, samarium-cobalt alloy) respectively on the amount magnets used in the rotor. The torque in PMASR motor and also in other IPM machines, where the q-axis is aligned with the PM, is derived by the equation (4.4).

$$T = \frac{3}{2} p \left[\psi_{PM} i_d + (L_d - L_q) i_d i_q \right] \tag{4.4}$$

, where the second part of the torque equation (L_d-L_q)$i_d i_q$ is usually higher in case of FASR machines compared to the IPM machines. Because in the IPM machines, the torque is mainly

developed by the PM flux instead of a magnetic saliency.
The cos φ increase is the most evident from the vector diagrams. The stator voltage equations in steady state, that can be delivered from the machines equivalent circuits for both SynRel and PMASR machine, are presented in equations (4.5) and (4.6) respectively.

$$\widehat{V}_\mathrm{t} = R_\mathrm{d} I_\mathrm{d} - \omega L_\mathrm{q} I_\mathrm{q} + jR_\mathrm{q} I_\mathrm{q} + j\omega L_\mathrm{d} I_\mathrm{d} \tag{4.5}$$

$$\widehat{V}_\mathrm{t} = R_\mathrm{d} I_\mathrm{d} - \omega L_\mathrm{q} I_\mathrm{q} + \omega \lambda_\mathrm{PM} + jR_\mathrm{q} I_\mathrm{q} + j\omega L_\mathrm{d} I_\mathrm{d} \tag{4.6}$$

The vector diagrams, that are based on equations (4.5) and (4.6) are presented in Figure 4.3.

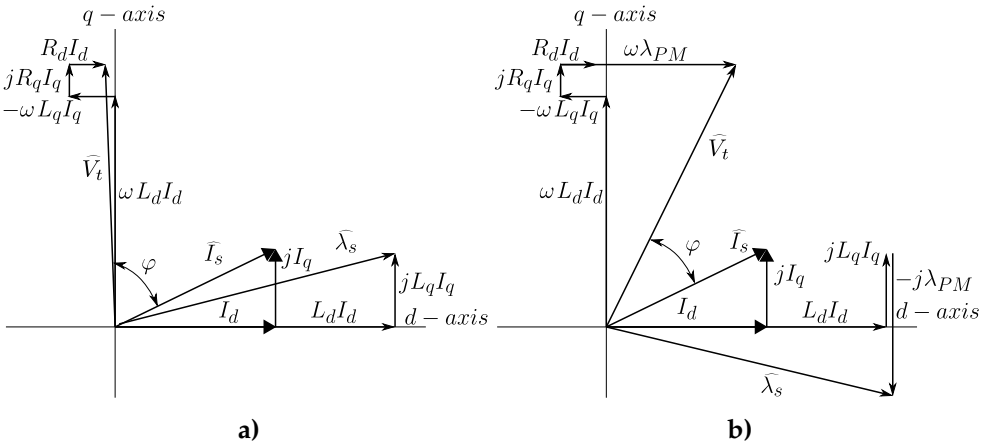

Figure 4.3: a) SynRel and b) PMASR vector diagrams from [116]

4.3 A state of art in traction applications of SynRel and PMASR

Since the primary focus of this thesis is on a traction application of the PMASR machines, therefore this section is presenting an overview of both the SynRel and PMASR machines in such applications.
The two summarizing publications [117, 118], focused on the RE-free traction machines, that were published in recent years are proposing a relatively good overview of such a machine alternative. In the publication [117] gives a good comparison depicted in Figure 4.4 of both the torque densities and machine constants of various traction motors.

The rising interest in the RE-free alternatives in traction is also supported by various papers presented in this field. The SynRel motors have found a way in elevators [119], a railway traction [120], electric vehicles in electrical transmission [121], as a drive component in an automotive [122–124], a scooter application [125] or as a general traction study [118, 126]. The PMASR traction applications are also well studied and used in EVs in [127–129] with ferrites and combinations of ferrites and RE magnets in [130, 131] and in low-speed applications [9, 36]. The outcomes from the mentioned papers could be summarized by following statements:

- It is possible to use PMASR or SynRel machines in the traction.
- The biggest advantage of SynRel machines is no risk of the demagnetization.
- A careful design is needed when the ferrite magnets in FASR are used.
- PMASRs have a higher TRV than SynRels.
- PMASR machines should have about 30 % longer stack-length to achieve the same output power compare to the SPM.

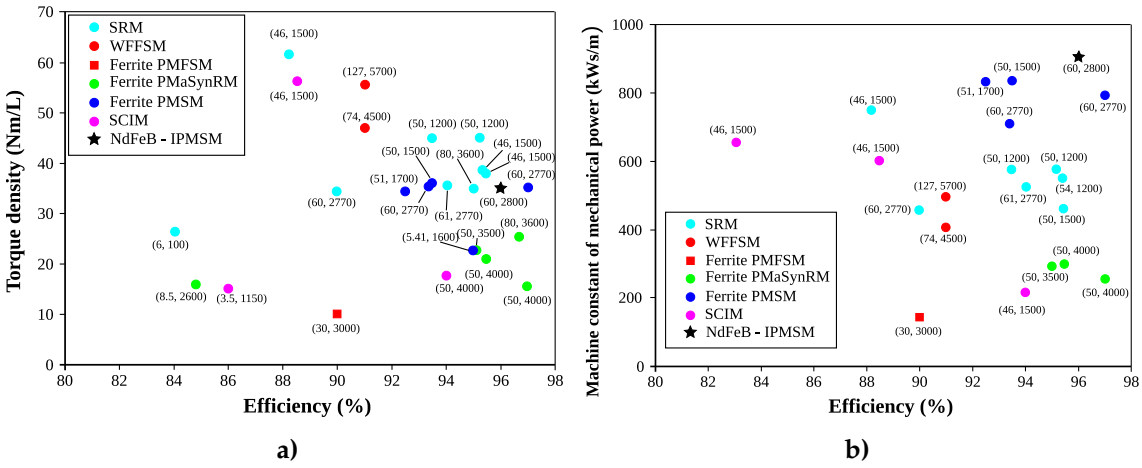

Figure 4.4: Torque density and machine constant comparison based on research presented in [117]. SRM - synchronous reluctance machine, WFFSM - wounded field flux switching machine, PMFSM - permanent magnet flux switching machine, PMaSynRM - permanent magnet assisted synchronous reluctance machine, PMSM - permanent magnet synchronous motor, SCIM - Squirrel cage induction motor, IPMSM - interior permanent magnet synchronous motor; vectorized from [117], values in parenthesis inform about the machine machine mechanical output power and the base speed.

- The [118] claims, that the PMASR with the same ξ have around 14 % higher output power than the SynRel in the similar size.

The main advantages and disadvantages of the SynRel and PMASR machines compared to IPMs are presented in Figure 4.5.

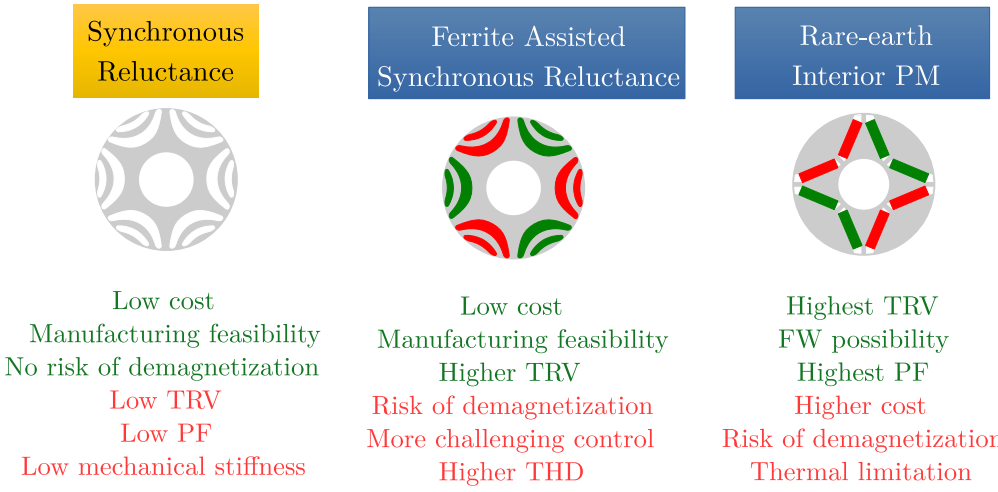

Figure 4.5: Comparison of the pros and cons of SynRel, PMASR and IPM machines

The possible PMASR design and the replacement of RE machine will be presented in the following chapters of this thesis.

5 | Optimizing algorithms

This chapter briefly introduces the optimizing methods used in the electrical machine design process. Firstly the algorithms will be divided according to their nature and then some of them will be presented more thoroughly. One algorithm candidate will be chosen from each category and will be explained in further detail along with the application example. All of the algorithms that are foreseen to be used for machine optimization will be also presented and highlighted within this chapter.

5.1 Definition of optimizing algorithms

Based on performed benchmarks, there has been a huge rise of much powerful processing components, both central processing units (CPU) [132] and graphics processing unit (GPU) [132] in recent decade. Those components are also becoming cheaper, so it can be said, that the amount of computation power per price is radically increasing [132]. The development of the CPU performance, by the average data, is achieved by the benchmarks described in [132].
Therefore it is more affordable and faster than before to use optimization algorithms to optimize various tasks. The optimization algorithm (OA) is according to [133] a programmable process or a function, that takes some sort of an input parameter or a value that modify characteristics of the device or function to find the minimum or maximum value of a result, an output or a cost. A simple illustrative figure of an optimization is depicted in Figure 5.1.

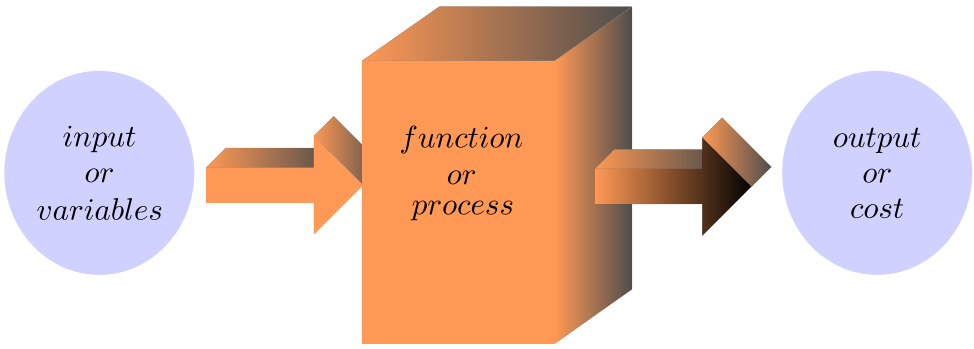

Figure 5.1: Types of OA, adopted and modified from [134]

In the mathematical definition can be the optimization described as a search for an optimal (maximal or minimal) value of a function f(X) within the (usually) constrained input variable X

from [135] is in (5.1).

$$\begin{aligned} &\text{Minimize/Maximize} && f_m(x), && m = 1,2,...,M; \\ &\text{subject to} && g_j(x) \geq 0, && j = 1,2,...,J; \\ & && x_{\min}^{(n)} \leq x^{(n)} \leq x_{\max}^{(n)} \end{aligned} \tag{5.1}$$

The solution x is a vector $x = x_1, x_2, .., x_n$, while $x_{\min}^{(n)}$ and $x_{\max}^{(n)}$ are the lower and upper boundaries of a specific variable in the vector.
In a very simplistic view, it can be said, that everything, that could be modeled or characterized with some input variables and can have objectively evaluated outputs or has a known function can be optimized.
In a world of optimization, many algorithms or functions have higher or lower efficiency. The algorithms are of great interest especially in the practice, where the optimal solutions are desired to be obtained and thus either save input energy (increase the efficiency of a system) or decrease the environmental impact of a process (reduce the processing time).
If an optimization problem, that is modeling some real case physical system, is evaluated only by one objective, then it is called the single-objective optimization. An example of such a problem could be the well-known traveling salesman problem. The algorithm in this case is supposed to search for a solution, where the salesman is traveling the shortest distance to visit all the cities in a given list and come back to the origin city. The obvious objective of such a problem is the traveling distance and the objective should be minimized, while the input of this system is the order of the cities, which the man is visiting. The problem is shown in Figure 5.2 a), where the different colors are showing the different solutions and the values are depicting the specific path lengths.

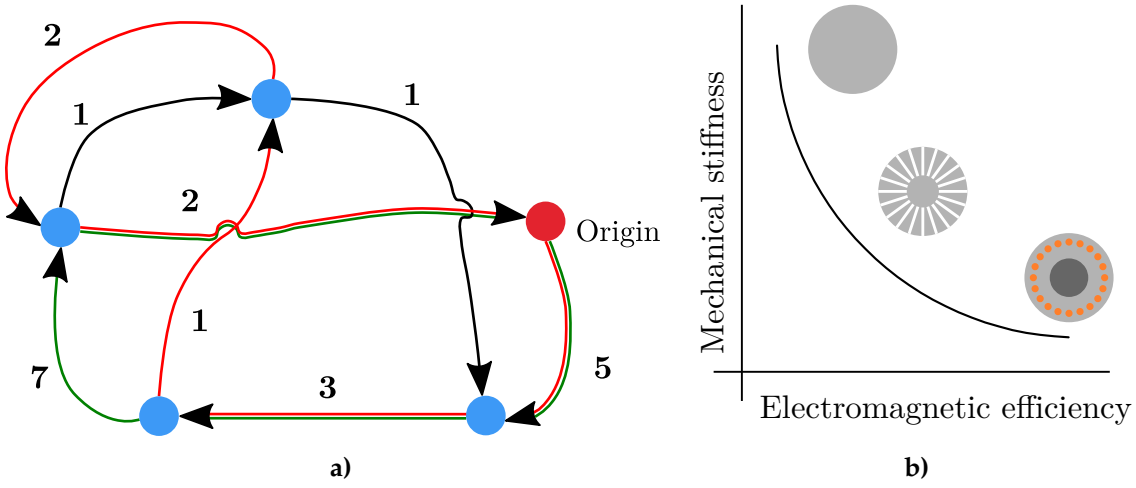

Figure 5.2: Example of a) single-objective (Traveling salesman) and b) multi-objective (Induction motor topology) optimization problem

On the other hand, most of the optimization problems in the real world are more complex and thus preferable to model and evaluate with multi-objective optimization (MOO). Multi-objectives could quantify the quality of such a physical model, those objectives could be in a direct opposite. An example of a physical problem, where the objectives, in this case, the electromagnetic efficiency and mechanical stiffness, are in direct contradiction is the choice of the induction motor topology. There are, in this case, two solutions that are significantly better in one objective, but it comes with the sacrifice in the other objective. The best efficiency can be

found in the squirrel-cage motor solution, but it has the lowest mechanical stiffness. The other ideal solution from the mechanical point of view is the solid-rotor topology, unfortunately, it has the worst electromagnetic efficiency. The best trade-off could be found somewhere between those two solutions, where for example the axially slitted induction motor is found as a good compromise regarding both objectives in this geometry. The vital information, that needs to be said, is that there is rarely only one optimum (optimal solution) but rather a set of optimal solutions. This optimization problem is depicted in Figure 5.2 b).

5.2 Multi-objective optimization

In the realm of the MOO the two multidimensional spaces are located - the N-dimensional decision space based on the number of input parameters and the M-dimensional objective space shaped by the evaluating objectives. The optimal solution(s) can be found in both multi-dimensional spaces. The set of optimal solutions in the case of the ideal MOO is called the Pareto front (PF). The example is shown in Figure 5.3.

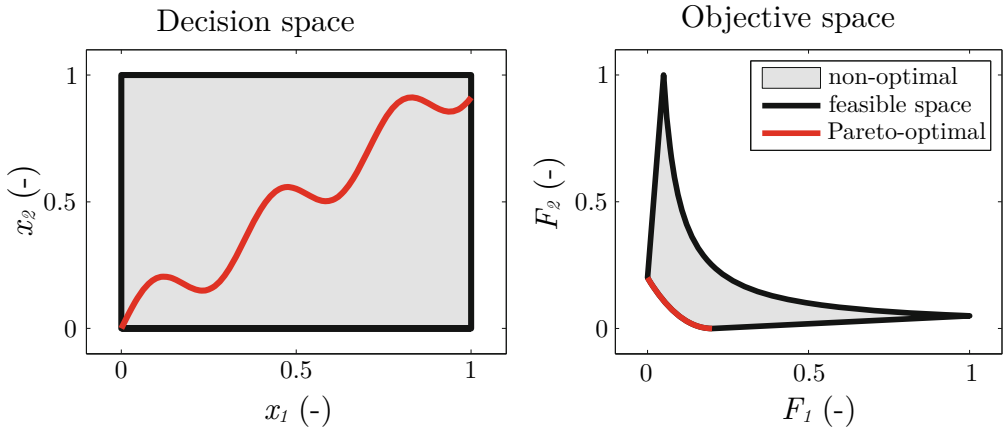

Figure 5.3: PF depicted in the decision and objective spaces in the optimization problem with two input parameters and two objectives

Since the area of the MOO is much broader and include also the EM design optimization process, the following chapters will be focused on this kind of optimization. According to [135] are there basically two approaches, how to solve a MOO problem:

- Preference based MOO (PBMOO) procedure
- Ideal MOO (IMOO) procedure

5.2.1 Preference based multi-objective optimization

The PBMOO procedure is historically the more preferred one. It was used more in the past mainly for one simple reason - the simpler single-objective optimizer.

5.2.1.1 Preference based vector

As it was mentioned at the beginning, the optimizer is supposed to find some sort of compromise between the chosen set of objectives. In this approach, as the name implies, the user

needs to define the preference based vector (PBV), that prefers one objective before the other one before the optimization starts. The vector consists of the set of weight coefficients ($w_1, w_2, ..., w_x$), that are specifying the user preferences of the specific objective. Theoretically, a different set of weight coefficients should give a different solution from the set of optimal solutions of the problem. The optimization flow diagram is presented in Figure 5.4.

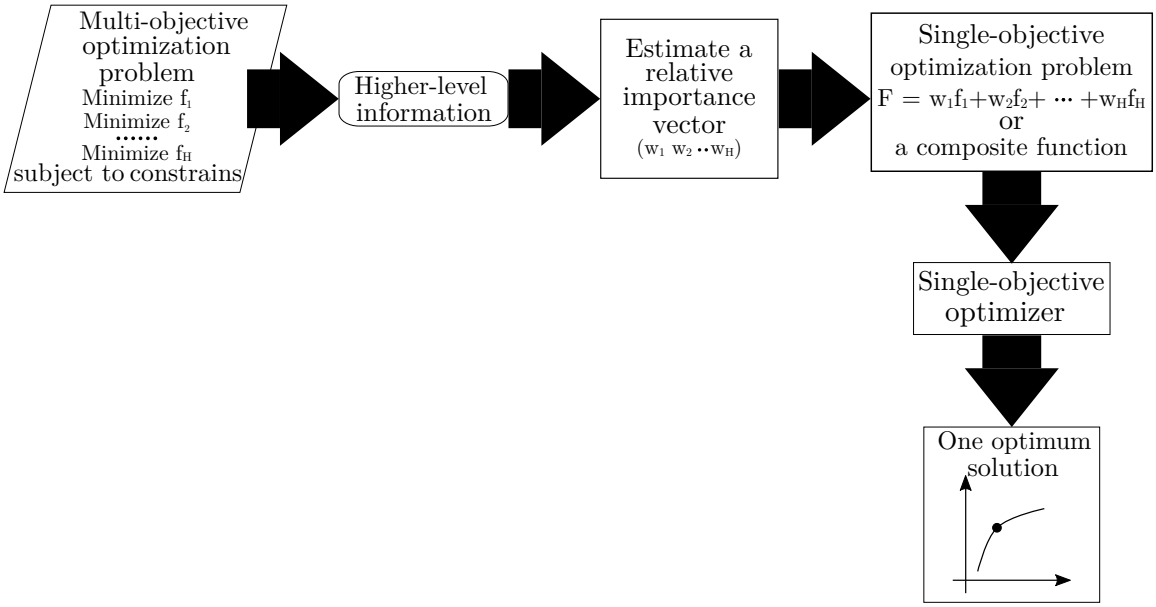

Figure 5.4: Preference based MOO flow scheme [135]

The problem that could come up, according to [135] with this optimization process is that a higher level of information enters the optimization as an input before the optimization begin. The higher level of information is a set of information, that could not be quantified by the objectives, e.g. manufacture feasibility, construction problems. Therefore the optimization results become very subjective and depend on the designer's point of view. Even the decision of the weight coefficient values themselves is a very complicated process. Usually, it is difficult to decide if the algorithm should focus on the e.g. motor total efficiency twice as much as on the temperature in the stator winding.
As an example the PBV could be in case of two objectives - the electromagnetic torque and the torque ripple (TR), where the torque is supposed to be maximized (assigned with the negative sign) and the TR is expected to be minimized, written in (5.2):

$$PBV = w_{\text{elmagT}} \cdot (-)T_{\text{elmagT}} + w_{\text{ripple}} \cdot T_{\text{ripple}} \tag{5.2}$$

, where w_{elmagT} and w_{ripple} are the weight coefficients for the electromagnetic torque and TR and the T_{elmagT}, T_{ripple} are the corresponding objective values.
The theoretical issue that might come up with such a definition of the PBV is that, while considering the weight coefficients to be dimensionless, the equation is summing up the two values with different units. Therefore the objectives need to be transformed into dimensionless coefficients as well. In this case, it needs to be decided if the objective is supposed to be minimized or maximized. For the optimally maximized objective e.g the above-mentioned torque, the formula has a form written in (5.3):

$$Obj\_Torque = \left| 1 - \frac{Torque}{Torque\_ref} \right| \tag{5.3}$$

where the *Torque* is an actual value of the objective and *Torque_ref* is a reference value for the objective. It is supposed to be chosen in a range that the resulting fraction does not exceed the value of 1, usually, it is the value of the objective desired by the user.
The second example is, that the objective value is supposed to be minimized, for e.g the losses in order to increase the efficiency or to satisfy the thermal requirements. The equation (5.4) becomes:

$$Obj\_Losses = \left| \frac{Losses}{Losses\_ref} - 1 \right| \tag{5.4}$$

where similarly to the first case, the *Losses* value is the actual amount of losses created in a machine, and the *Losses_ref* are the losses that are desired by the optimization.
The special case of an objective is the objective, where the specific value is expected to be reached by the optimizer. It could be for example the induced voltage by the PM. In this case, the equation (5.5) for the objective calculation becomes:

$$Obj\_voltage = \left| \frac{Desired\_voltage}{Voltage\_ref} - \frac{Voltage}{Voltage\_ref} \right| \tag{5.5}$$

The objectives transformed into dimensionless numbers are then combined with the coefficients into a PBV. Ideally, all the objectives are optimized and the cost function is minimized during the optimization run.

5.2.1.2 Penalty function

According to [136] it is beneficial to convert constrained problems into unconstrained along with introducing the penalty for the constraint violation. This is addressed by the penalty function, where the correlating objective values are transformed by various transform curves. An example of the polynomial transformation curve, used in [137] is shown in equation (5.6). All transformation curves, including function 5.6, which is in Figure 5.5 labeled as "Curve 1", that were successfully used in the practical EM design in [137], are shown in Figure 5.5.

$$f_1(x) = 8.89x^6 - 33.75x^5 + 48.09x^4 - 33.03x^3 + 11.46x^2 - 0.68x + 0.01 \tag{5.6}$$

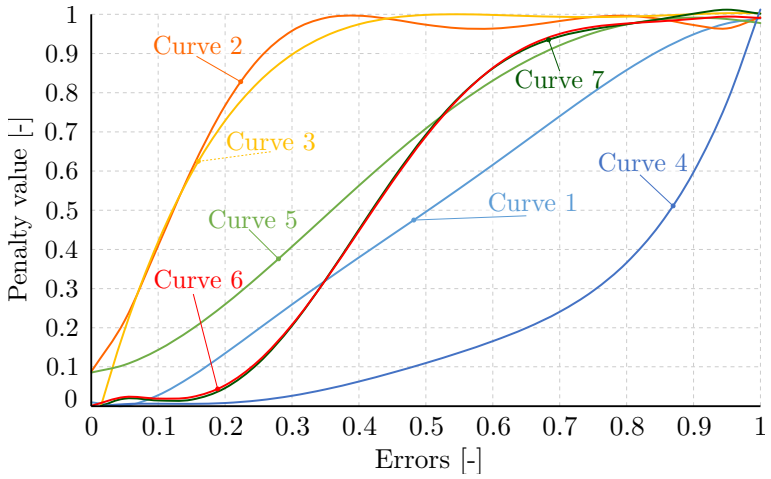

Figure 5.5: Penalty functions introduced and employed successfully used in [137]

5.2.2 Ideal multi-objective optimization procedure

Besides the first preference based MOO there exists an alternative approach called the IMOO procedure. This solution is defined as a two steps process. The process is shown in Figure 5.6.

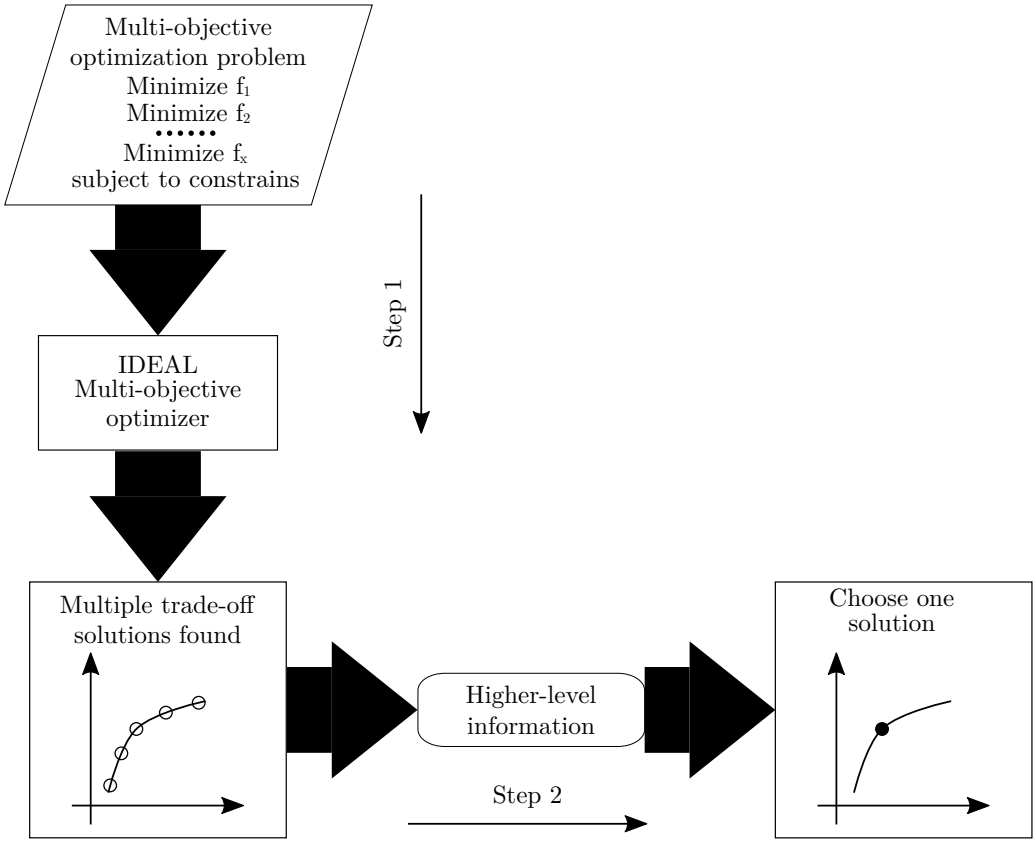

Figure 5.6: Preference based MOO flow scheme [135]

The process stands on the definition of the optimization objectives as the only input into the multi-objective solver in the first step. The multi-objective optimizer is, as mentioned above, in principle a more sophisticated algorithm. When compared to PBMOO approach there is no need to recalculate the objectives to a dimensionless form, but rather to keep the values in the original form with the dimensions (e.g. Nm, %, W). And even further not to form some objective combinations and their corresponding weight coefficients. The outputs of the first step are the multiple trade-off solutions, that are found optimal along the multiple objectives chosen by the user. The multiple trade-off solutions, that are ideally spread over the optimal solutions curve are called the PF solutions.
The second step is the place, where the user's higher level of information is involved. Instead of defining, in some cases, relatively vague coefficients, the user chooses from the previously estimated best trade-off solutions. This gives the user a big advantage of choosing the optimal solution and balance the objectives.
The multi-objective optimizer, besides being able to optimize more objectives, needs to involve some special functions, that are not considered in the preference based optimizing procedure. Two of these functions, that are common in MOO algorithms, used in this thesis, that were introduced in the [138], are:

- Non-dominant sorting
- Crowding distance

5.2.2.1 Non-dominant sorting

This idea was firstly introduced in [139]. The book has introduced the terms: dominant and non-dominant solutions. The dominant solutions are defined by either having gain in all objectives against other individuals or having a significant gain in at least one objective. The non-dominant solutions are defined as being dominant in at least one objective while being "worse" in the other objectives. As an example of the non-dominant and dominant solutions serves Figure 5.7.

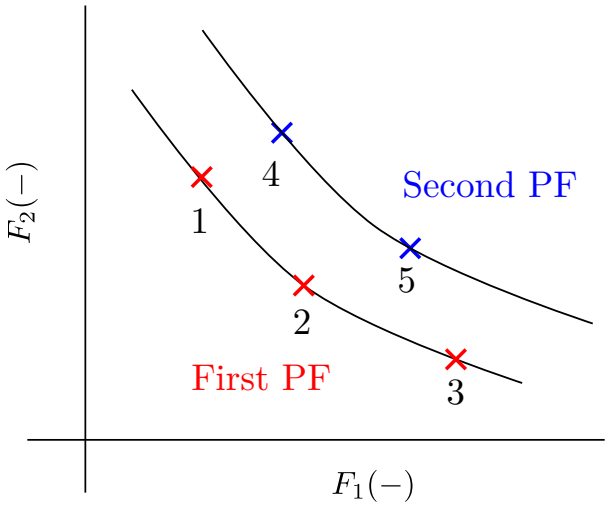

Figure 5.7: Dominant and non-dominant solutions

Figure 5.7 illustrates the situation, where the solution 1 is considered to be non-dominant to solutions 2 and 3 and vice versa and those three solutions creates the PF. There lays the simplest definition of the PF, that is a set of non-dominant solutions. In Figure 5.7 two sets of non-dominant solutions (PF) are depicted - the First PF and the Second PF. The members of the First PF dominates the members of the Second PF. The mathematical expression of such a diversion is presented in [139] by (5.7):

$$(x <p\ y) \Leftrightarrow (\forall_i)(x_i \leq y_i) \wedge (\exists_i)(x_i < y_i) \tag{5.7}$$

, where the x and y are considered to be vectors and the relation symbol $<p$ expresses partially fewer relations between those two vectors.

5.2.2.2 Crowding distance

The crowding distance was introduced in [138], where it is also labeled as the "density estimation", and is helping an algorithm to spread evenly trade-off solutions on PFs. This helps to maximize the portfolio of possible and equally distributed solutions in the objective space. This step should allow the user to choose the optimal trade-off solution from the PF and help the algorithm to focus on the less crowded areas of the PF. The crowding distance usually follows the non-dominant sorting procedure, therefore into this process come the sorted vectors of objective values. The mathematical description of function is in (5.8) and (5.9).

$$c(I_m(i)) = \sum_{m=1}^{M} c_m(I_m(i)) \tag{5.8}$$

where

$$c(I_m(i)) = \frac{f_m(I_m(i+1)) - f_m(I_m(i-1))}{f_{m,max} - f_{m,min}} \tag{5.9}$$

where $I_m(i)$ is the i-th index from the m-th vector of indices, the $f_{m,max}$ and $f_{m,min}$ are the maximal and minimal values of the m-th objective in the current front, respectively, as presented in [140]. The method is depicted in Figure 5.8.

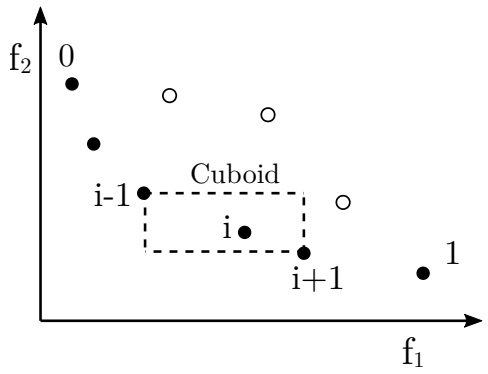

Figure 5.8: Crowding distance explanation [138]

This function is generally used with success used in many MOO algorithms, such as the differential evolution algorithm [141] or in the particle swarm optimization [142], due to its simple and effective purpose. In [143] this method was replaced because of its computational demand. But since it is expected that the calculations of the EM designs are significantly more demanding, the time required for the crowding distance estimation time becomes almost negligible in the whole optimization process, therefore the algorithms in this thesis will take advantage of this method.

5.3 Sorting of optimization algorithms

Besides the OA sorting based on the number of objectives, there is the second perspective one can take - the algorithm principle. The majority of the well-known algorithms could be used in the single and multi-objective variants. The same could be said about the algorithm versions for the PBMOO and IMOO. The comparison of the same algorithm with a different MOO approach is one of this thesis aims.
Probably hundreds of OAs can be found in the literature. Always some trade-off has to be met between the complexity of the algorithm and its efficiency of finding the best solution (global optimum). Although those two objectives could be in direct opposition, some algorithms have found a suitable trade-off to partially satisfy both conditions. The general categories of the OA can be found in [134] and the modified overview is shown in Figure 5.9, while the category named "With the added level of sophistication" is added.

In the following subsections will all OA categories be described along with the applications in the literature and one algorithm example (usually the best known) will be selected and explained more thoroughly.
The category of the combined OA will be mentioned last since both the self-organizing migrating algorithm (SOMA) and genetic algorithm (GA) fall into this category and those algorithms will be all described in detail.

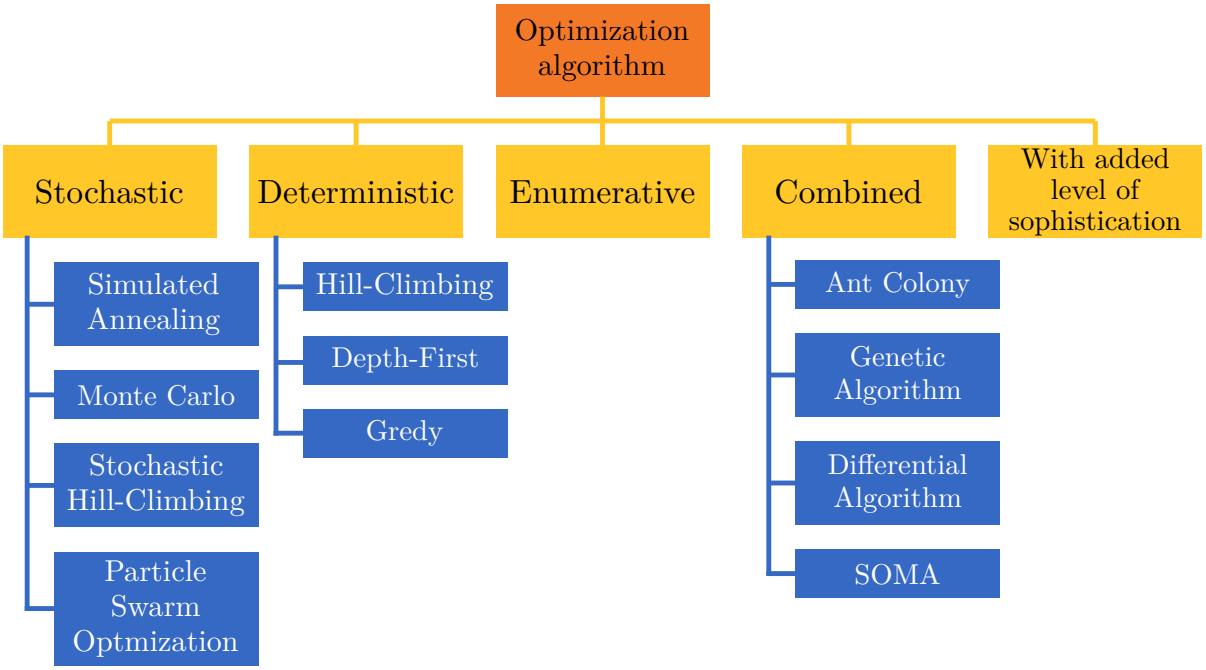

Figure 5.9: Types of OA adopted and modified from [134]

5.3.1 Stochastic algorithms

The stochastic algorithms (SA) are based on using the randomness of the system to maximize or minimize the objectives. Over the years, the SA became important to various science [144], engineering [145], economy [146] and other fields, where optimization is used. The randomness employment, the key SA characteristic, could also be implemented to other algorithm types, according to [147] and [148] usually by some random parameters or constrains. The characteristics of the SA are by [134]:

- Slow
- Suitable for small objective spaces

5.3.1.1 Particle swarm optimization

The particle swarm optimization (PSO) is the best known and the most used algorithm in the SA category, based on the number of papers published in the recent years. Since a lot of the development time was devoted into it, the PSO has many modifications, that are briefly summarized in Figure 5.10.

The PSO principle was introduced in 1995 by J. Kennedy and Russell Eberhart in [150]. The first algorithm idea was based on the collision-proof birds and was trying to imitate their behavior while searching for food, mates, or ideal environmental parameters, such as the temperature. The main motivation was to introduce a simple and effective OA, with the least amount of control variables. The original paper considered at first just three input variables, while two variables were found relevant the first being the size of the swarm and the other one was the inertia weight labeled ω. The parameter called craziness, which influences bigger stochastic behavior, was removed. The algorithm particles behave in a certain way based on their current position vector $X_i^t = (x_{i1}, x_{i2}, x_{i3}, ..., x_{in})^T$ in a hyperspace and a velocity vector $V_i^t = (v_{i1}, v_{i2}, v_{i3}, ..., v_{in})^T$ for every i-th particle at the time t, control parameters setting and the randomness of the system

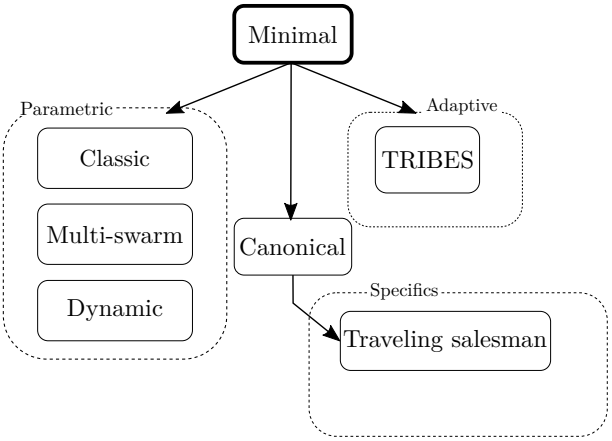

Figure 5.10: Types of the PSO [149]

in a dimension j as introduced in (5.10).

$$V_{ij}^{t+1} = \omega V_{ij}^{t} + c_1 r_1^t (pbest_{ij} - X_{ij}^t) + c_2 r_2^t (gbest_j - X_{ij}^t) \tag{5.10}$$

and (5.11)

$$X_{ij}^{t+1} = X_{ij}^t + V_{ij}^{t+1} \tag{5.11}$$

, where the $i = 1, 2, ..., P$ and $j = 1, 2, ..., n$ (P is the amount of particles and n is the number of objectives). The first term is based solely on the particle initial speed and the inertia weight factor. If ω is equal to one, the particle motion is fully influenced by the previous motion, by decreasing the parameter, the influence is reduced. This variable influences the algorithm tendency towards the global instead of a local optimum.
The second term is called the individual cognition term and depends on the particle best (*pbest*) position during the optimization, the parameter c_1 is therefore called the individual-cognition parameter. The parameter r_1 is a random parameter in range $[0, 1]$ introducing the randomness to the system.
The last part of the equation is the social learning one. This part forces the particle to travel towards (so far) the best solution found by all particles *gbest*. This is again controlled, this time by the social learning parameter c_2 and random parameter r_2, that has the same range as the parameter r_1.
The algorithm is in [151] described as follows:

1. Initialization
   - 1.1. For each particle i in a swarm population size P:
     - 1.1.1. Initialize $\boldsymbol{X_i}$ randomly
     - 1.1.2. Initialize $\boldsymbol{V_i}$ randomly
     - 1.1.3. Evaluate the fitness $\boldsymbol{f(X_i)}$
     - 1.1.4. Initialize $\boldsymbol{pbest_i}$ with a copy of $\boldsymbol{X_i}$
   - 1.2. Initialize $\boldsymbol{gbest}$ with a copy of $\boldsymbol{X_i}$ with the best fitness
2. Repeat until a stopping criterion is satisfied:
   - 2.1. For each particle i:
     - 2.1.1. Update $\boldsymbol{V_i^t}$ and $\boldsymbol{X_i^t}$ according to equations (5.10) and (5.11)
     - 2.1.2. Evaluate the fitness $\boldsymbol{f(X_i)}$
     - 2.1.3. $\boldsymbol{pbest_i} \leftarrow \boldsymbol{X_i^t}$ if $\boldsymbol{f(pbest_i)} < \boldsymbol{f(X_i^t)}$
     - 2.1.4. $\boldsymbol{gbest_i} \leftarrow \boldsymbol{X_i^t}$ if $\boldsymbol{f(gbest_i)} < \boldsymbol{f(X_i^t)}$

Note: The equations from the original text are relabeled with the labels used in this work.

The steps at the time t (a)) and $t+1$ (b)) are depicted in Figure 5.11.

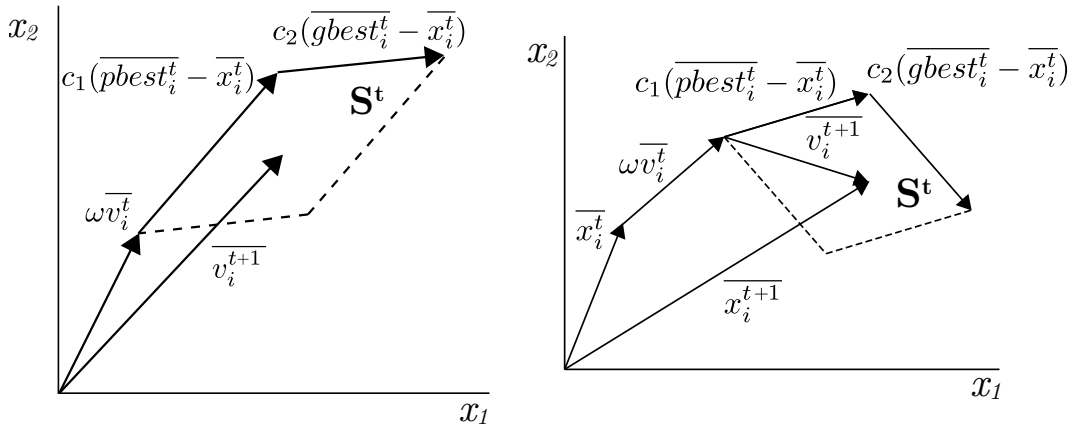

Figure 5.11: a) The velocity vector at the time t being the composed from components, b) The updated position vector at the time t composed from the components [151]

5.3.2 Deterministic algorithms

The deterministic algorithms (DA) are on the contrary to SA based only on the exact mathematical functions and expressions. The DA approaches rely on linear algebra since they are usually based on gradient computation with their advantages and disadvantages. The advantages are, according to [134], obviously a very fast convergence in comparison with the SA, with a lower number of fitness function evaluations (FFE). The biggest disadvantage is that the DAs tend to converge into the local optimum instead of the global optimum. Such algorithms need to have some predetermined parameters and have some assumptions of the problem before the optimization process starts, assumptions of the problem could be [134]:

- Linearity of a problem,
- convexity of the problem,
- small objective space.

The DAs are also being developed and optimized towards the best efficiency and applicability in various fields such as the finance [152], the chemical engineering [153] or the engineering design [154]. The DA is by definition just a single objective, therefore it cannot be used in the EM design process, but the example of the DA will be shown regardless of this fact.

5.3.2.1 Hill-climb algorithm

The hill-climbing algorithm is one of the best known DAs. Since it is based on the specific mathematics description it is very fast, as was mentioned in the deterministic subsection. The principle is inspired by following the increasing elevation of a person climbing up the hill to reach the top. It is very computationally efficient since the algorithm evaluates only the current position till no increased value in the neighborhood of the current algorithm position is found. In Figure 5.12 below are depicted the possible "risky" algorithm positions [155].

The first issue could be found, when it reaches the plateau, in Figure 5.12 named as shoulder or the "flat" local maximum, where the increased values are eventually no longer around the

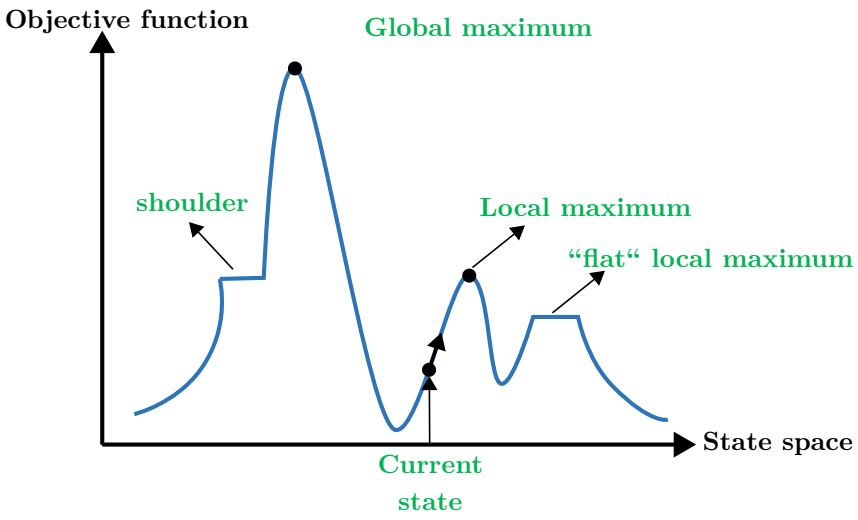

Figure 5.12: Hill climbing algorithm, adopted from [155]

positions. The algorithm becomes stuck in these positions not finding the global optimum, which is the optimization goal. The other position, where the algorithm can end the searching process is the local optima. This position is similar to the previous ones in not having a higher value in the neighboring positions, while still not reaching the highest (global) optimal solution. All of these solutions are addressed for example in the smart hill-climbing algorithm [156], where the Latin Hypercube Sampling is applied. This improves the decision space sampling coverage. The hill-climbing algorithm optimization was compared with the genetic algorithm in [157] with relatively good results in the traveling salesman problem, which was in this thesis introduced in section 5.1. The use of the hill-climbing algorithm in the area of the credal network, that is a graphical structure, is shown in [158].

5.3.3 Enumerative algorithms

The principle of enumerative methods is an estimation of all possible characteristics combinations of a problem. This method is suitable for problems, where the characteristics are discreet and the amount of characteristics combinations is relatively small [134].

5.3.4 With the added level of sophistication

The last considered OA type is the one with the added level of sophistication. This algorithm is using a neural network as a training model, which is being evaluated and trained by the computation of a real physics model, e.g. an electric machine in [159]. After the training procedure, the model is used to find the optimal solution, which is verified again by the initial physics model. This type of optimization claims to significantly speed up the optimization process, especially when the afterward trained model is used in other analyses, such as tolerance analysis, as demonstrated in [160]. The surrogate time-saving optimization procedure is shown in Figure 5.13

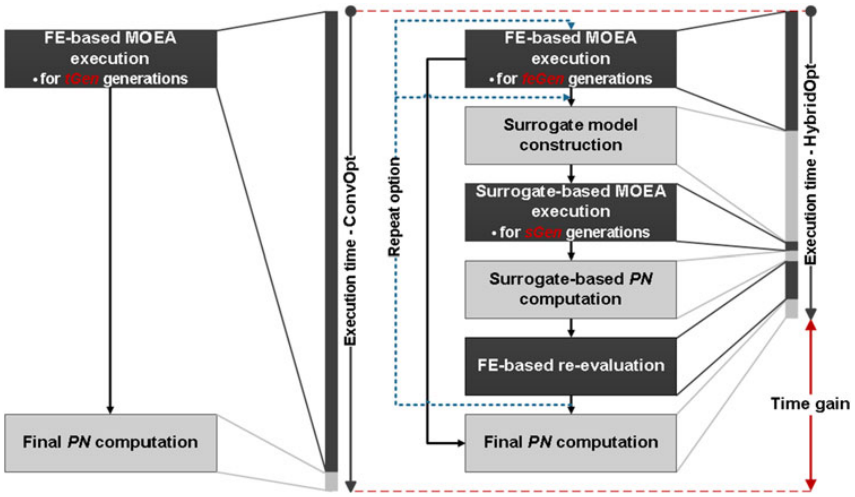

Figure 5.13: Surrogate optimization procedure [159]

5.3.5 Combined algorithms

Slightly more sophisticated algorithms are named combined. The combined algorithms are, as the name implies, a combination of two types of OAs to achieve the best performance. Usually, the stochastic and deterministic OAs are combined. A major part of the combined OA that is also widely used, but not only, in a EM optimization is called the evolutionary algorithms (EA). The combined algorithms could be characterized by the following characteristics [134]:

- Robust - Optimal solution is found regardless of the initial condition setting,
- effective and powerful,
- can find more optimal solutions within one searching process.

According to [135] the combined, more precisely EA, are the most widely used algorithms for the MOO. Even though the book was written in 2002, this claim becomes even more true nowadays. Because of the listed characteristics, algorithms that are suitable with the highest probability to find the optimal solution and are used in this thesis, are all from the EA category. Both algorithms will be described in a separate section.

5.4 Optimization algorithms used in this thesis

The OAs used in this thesis, were two EA - GA and SOMA in both the PBMOO and IMOO versions. This decision is expected to derive two comparisons. The first is, that the MOO is more versatile and robust, thus more suitable for the EM optimization and the second is to compare the multi-objective variants of both GA and SOMA algorithms.

5.4.1 Genetic algorithm

Genetic algorithms are heuristic search approaches [161]. The GA was first, according to [161], introduced in [162][1] in the 1975 and was based on the binary string representations. D. Goldberg was able to solve with this algorithm the difficult problem of gas-pipeline control in his dissertation thesis [139]. Over the years was this algorithm used in various applications

[1] Note: Cited was the second edition of the book, due to the missing citing info on the first edition of this book

from the biomedical domain [163], architecture [164], engineering [165], EM [166] and machine learning applications [167].

5.4.1.1 History

The whole idea of evolution is based on the Darwinian theory of evolution [168]. But the whole study of genetics, in his case of a pea plant, began, as noted in [133], with Gregor Mendel. His studies focused on how the traits of one plant generation were passed onto the next one. The idea of passing parents certain traits *pheonotype* onto the offspring *genotype* (combination of *alleles* - traits of both parents) have roots in the Mendel's work. The two laws, that Mendel introduced were the principle of segregation - there must be factors inherited in pairs; and the law of independent assortment - the passing of one trait is independent of the other trait.
Darwin took this theory of passing traits under certain circumstances and added a natural selection and evolution, resulting in one more complete theory. A simple diagram of this theory is presented in Figure 5.14.

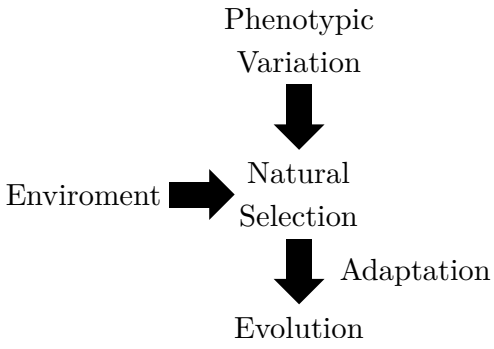

Figure 5.14: Principle of the Darwin evolution theory [168]

5.4.1.2 Preference based multi-objective algorithm version

The basic GA (further references as a GA) is the algorithm, that is based on a belief in an evolution theory and its sufficiency to find an optimal solution from either random [137] or improved initial population strategy [169]. The GA is based on PBMOO and includes all processes from the Darwinian theory. Considering the PBMOO technique, as prior to the whole optimization is the "initialization process" - the definition of the cost function and weight coefficients along with the definition of the objectives. After the algorithm initialization process beginning the initial population is generated and evaluated by the fitness function. As an ideal initial population is considered such a population, that is distributed along with the whole decision space, to cover most of the space and therefore increase the efficiency of finding the global optimal solution. Sequential to the fitness evaluation is the production of the new offspring and processes connected to it - the crossover and mutation. The algorithm the basic GA process is as described in [133] and is shown in Figure 5.15.

Directly after the initial population evaluation comes to the **selection of the mates**, that will perform a crossover. The popular approaches to the selection of the mates are the tournament selection and pool selection.
The **tournament selection** is based on the random selection from the individuals. The probability of picking an individual is the same for all individuals. When the picking part is complete,

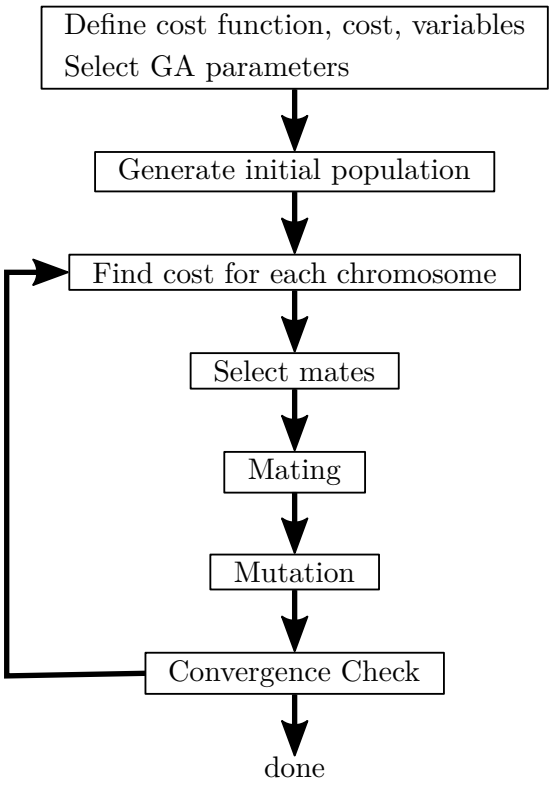

Figure 5.15: Basic GA algorithm [133]

the individuals are compared with regards to their cost function and the best one is selected. The figure depicting the decision process is Figure 5.16 a).
The **pool selection** (sometimes in the literature noted as the "roulette wheel" strategy) is based on the claim from [162], that an individual who is twice as good should have double the probability of being chosen. The principle is usually demonstrated on the pool, hence the pool selection name, where are the individuals placed corresponding to their fitness value and the individuals are randomly taken out from the pool. The probability of choosing the most populated individual in the pool is the highest. Following the roulette, an analogy is the roulette arc lengths divided by the fitness values, and the roulette is spindled and finishes the spinning at a certain position. Again the probability of roulette finishing its spinning at the longest arc, corresponding to the individual with the highest fitness, is the highest. In Figure 5.16 b) is the situation of different fitness scores depicted on the three individuals (labeled as A, B, and C) with different fitness scores in both the pool and roulette scenario.

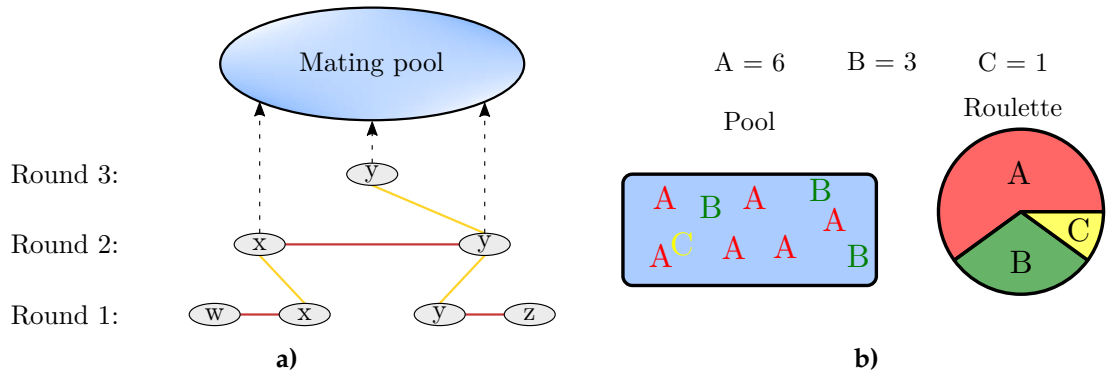

Figure 5.16: a) Tournament selection based on [170], b) The pool and roulette selection [162]

The **crossover** part of the algorithm allows combining the parents of genetic information into the genetic information of the offspring. In nature is the crossover done between two parents, but in the GA can be the crossover extended to more parents [171]. The crossover process can have multiple modifications, it can have one or two fixed or randomly located crossover points. The most common form is in [133] named the crossover between two parents with a randomly located crossover point between the first and the last bit of parent's chromosomes. The example of the crossover with two parents with a highlighted splitting point (crossover point) is in Figure 5.17.

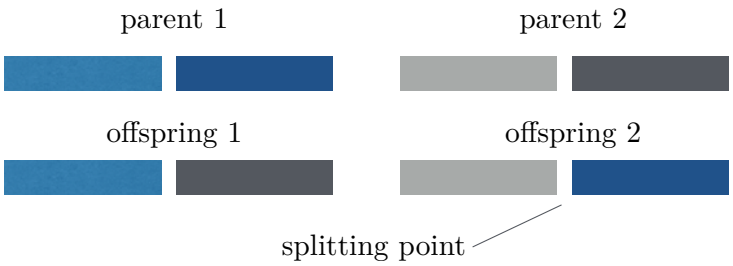

Figure 5.17: Crossover procedure [161]

The last operation is the **mutation**. The mutation introduces two things in the GA - more stochastic behavior and an extension of the initially determined decision space. The mutation is the process in which a randomly chosen part of the crossover chromosome is changed within the previously determined boundaries. The mutation of a parameter is chosen randomly in a matrix $N_{\text{population}} \times N_{\text{parameters}}$. Control parameters of the basic GA are listed in Table 5.1.

Table 5.1: GA control parameters

Parameter	Range	Description
Population size	Varies with a problem	Amount of individuals within each gen.
Mutation rate	$0 \div 1$	Probability of mutation
Selection	$0 \div 1$	Individuals kept from previous gen.
Number of iterations	Varies with a problem	Limit of algorithm iteration

5.4.1.3 Ideal multi-objective algorithm version

This version of the GA is based on an IMOO process leading to multiple Pareto optimal solutions. Therefore the algorithm includes both functions introduced in the subsection 5.2.2. The best known algorithms working on the principle of genetic evolution are the Non-dominated sorting genetic algorithm (NSGA-II) [138] and the strength pareto evolutionary algorithm (SPEA2) [172]. Even though these two algorithms are very similar, the NSGA-II is probably more famous in an EM design [7, 112, 160]. Both algorithms were improved and presented on test functions [143, 173], but not widely used in practical applications and find better efficiency in a higher number of objectives (four or more). Since the NSGA-II algorithm is more popular, it is chosen for the comparison. The NSGA-II principle is depicted in Figure 5.18.

The NSGA-II procedure flow after the initial population estimation is in [135] as following:

1. Combine the parent and offspring populations and create $R_t = P_t \cup Q_t$. Perform a non-dominated sorting to R_t and identify different fronts. F_i, $i = 1.2, ...,$ etc

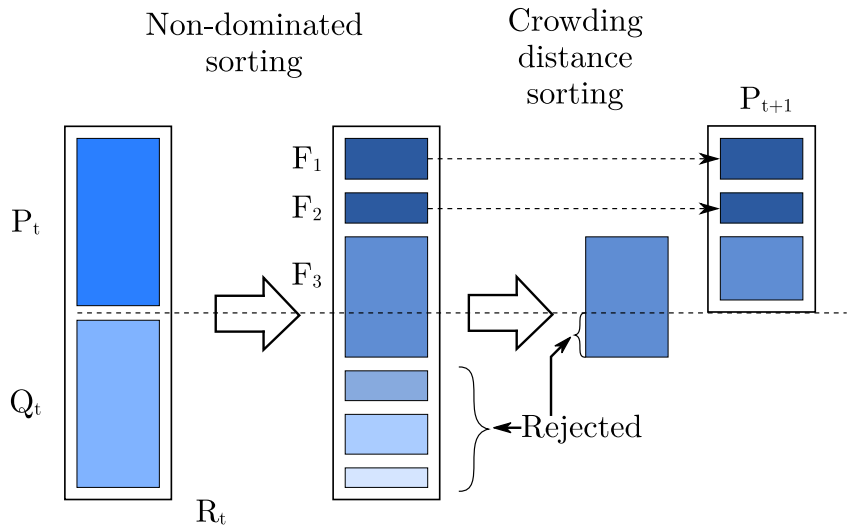

Figure 5.18: NSGA-II principle from [135]

2. Set the new population $P_{t+1} = \emptyset$ and set counter i = 1. Until $\mid P_{t+1} \mid + \mid F_i \mid < N$, perform $P_{t+1} = P_{t+1} \cup F_i$ and $i = i + 1$.
3. Perform the crowding-sort ($Fi <_c$) procedure and include the most widely spread ($N - \mid P_{t+1} \mid$) solutions by using the crowding distance values in the sorted F_i to P_{t+1}.
4. Create offspring population Q_{t+1} from P_{t+1} by using the crowded tournament selection, crossover and mutation operators.

The crossover, tournament selection, which is not only dependent on the fitness value, but also on the crowding distance and mutation process is similar to the ones used in the GA algorithm.

5.4.2 Self-organizing migrating algorithm

The second algorithm, that will be used and compared within this thesis is the SOMA. This algorithm, similarly to the GA, falls into the EA category, although not working on a principle of evolution, and by its nature is located in the combined algorithms. The algorithm was developed by prof. Zelinka in 1999 [134] and was proven successful in many applications such as a chemistry [174], programming [175], EM [137, 176]. The modified SOMA to a team approach in [177] and with self-adaptive parameters modification in [178].

5.4.2.1 Preference based multi-objective algorithm version

This algorithm version is again focused on a single-objective optimization or PBV type of multi-objective optimization. It is based on the idea from [134] and is based on the natural behavior of an animal group, thus competitive-cooperative strategies and by this, as mentioned in [134], falls right between the memetic and swarm algorithms (introduced in subsection 5.3.1.1. The memetic algorithms are, based on [179], an extension of the GA equipped with the local search technique to reduce a premature local convergence.
A group of animals, that have a predator instinct, are driven by their needs to find prey. An example widely use in SOMA literature is a group of wolves, this image is also used in [134]. One member of the pack has to be the closest one to the prey and the other members follow him. The closest member to the food is in the algorithm terminology called the leader. The

other members while traveling towards the leader in epochs, called in SOMA migrations, could become even closer to the prey. In the next migration is this member assigned with the honor to become the new leader and the other members are again changing their direction to him instead of the previous leader. This type of cooperation is beneficially used in this algorithm.
The algorithm steps of the AllToOne version are depicted in Figure 5.19.

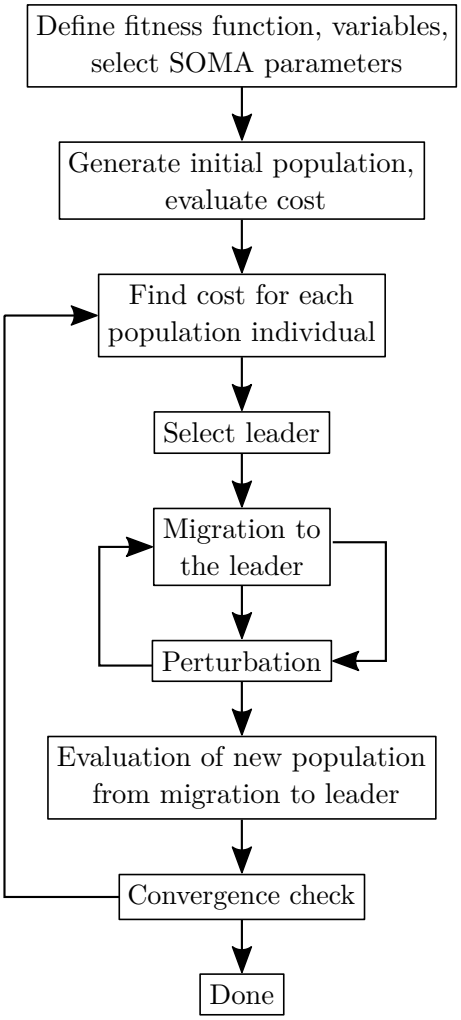

Figure 5.19: SOMA AllToOne principle [137]

As foreshadowed in Figure 5.19, the SOMA algorithm has multiple versions, that differ in the goals of the migration. SOMA versions are:

1. AllToOne - The "basic" strategy, all individuals, except the leader, are traveling towards the leader, who remains at the same position. This strategy is depicted in Figure 5.20 a).
2. AllToAll - No leader is selected, all individuals are traveling to the other individuals. It is more computationally demanding. This version is shown in Figure 5.20 b).
3. AllToAll Adaptive - Similar to the previous AllToAll version, but the individuals after the migrations stay at their best-found position.
4. AllToRand - Leader is chosen randomly and other members are traveling towards him.
5. Clusters - Hyperspace is divided into clusters and each individual population is tested in this cluster.

Similar to the GA the SOMA also has a set of control parameters, that could be tuned and modified. The parameters are along with the recommended range and suggested optimal setup for the EM design in [137] listed in Table 5.2.

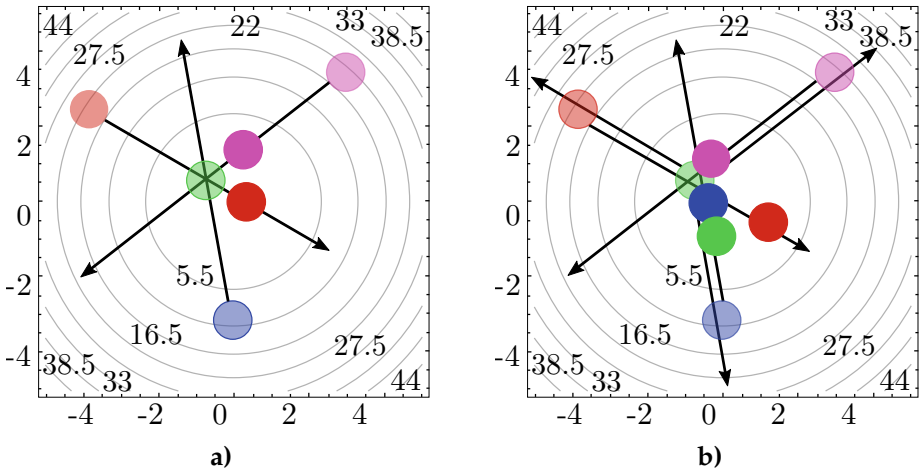

Figure 5.20: a) SOMA AllToOne strategy, b) SOMA AllToAll strategy; Members before the migration are distinguished by the decreased opacity [134]

Table 5.2: SOMA important control parameters

Parameter	Range from [134]	Used in EM design [137]
PathLength	[1.1, 5]	2.1
Step	[0.11, PathLength]	0.11
PRT	[0, 1]	0.3
PopSize	[10, up to user]	20
Migrations	[10, up to user]	10

The **PathLength** size defines how far each individual has to travel on a way to the Leader, while value 1 means, that the individual stops at the Leader position. **Step** value defines how many steps are sampled during the traveling. **PRT** parameter, usually in a form of a vector of a size equal to the number of parameters, distorts the straightforward way of individuals moving on a way to the leader, explained in Figure 5.21. The number of the individuals (members of the herd, in an animal metaphor used in the subsection introduction part) and the number of migrations of an algorithm is influenced by **PopSize** and **Migrations** respectively. All parameter values influence the conversion and the final cost function value is presented in [134]

5.4.2.2 Ideal multi-objective algorithm version

This version was proposed by P. Kadlec and Z. Raida in [134] and was successfully used in the design of electromagnetic components [180] and also compared to other conventional methods in [181]. The idea behind the multi-objective self-organizing migrating algorithm (MOSOMA) is to adopt the intelligent traveling individuals principle to the multi-objective objective space instead of traveling in a decision space hyper-plane. Instead of moving towards the member with the lowest cost value or randomly towards another member or all other members, the MOSOMA algorithm chooses the members closest to the so-called "True Pareto front". The true PF is assumed to be the best possible Pareto set of optimal solutions. This strategy is in [134] named "AllToMany". The algorithm run in these steps [134]:

1. The control parameters and the definition of the objectives.
2. Initial population generation and objectives evaluation.

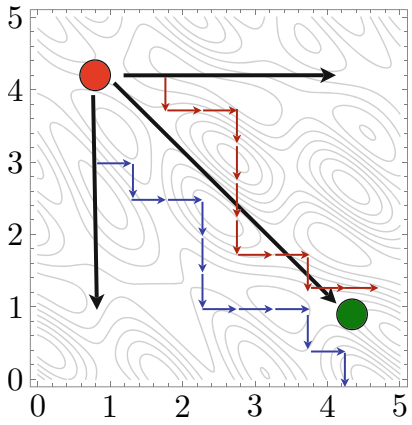

Figure 5.21: PRT vector influence on a member traveling, the solid black diagonally facing line implies the straightforward traveling, other trajectories are showing the way when the PRT vector is recalculating after each step the individual took. The other two lines are depicting the member's travel path influenced by the PRT vector, not recalculating after each step [134]

3. Choosing the "Many" (migrating agents) members, that the other will travel towards.
4. Perform the traveling migration and select the new agents for the next migrations.

The procedure is also depicted in Figure 5.22, where are two stages depicted. The first one is labeled with x_{-1} and represents the previous generations, EXT is the external archive (the "Many") to whom are the individuals traveling. The x represents the current generation, that got closer toward the "True Pareto", over the EXT archive, represented with the solid black line.

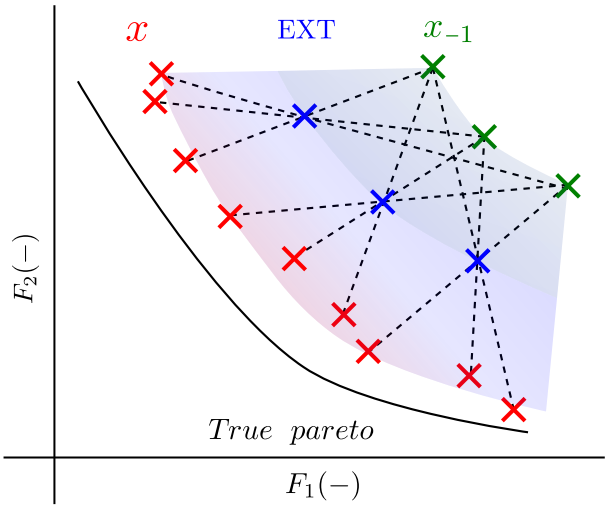

Figure 5.22: MOSOMA principle from [180]

As the algorithm stopping condition was either considered the desired number of members in the external archive or the performed number of migrations, similarly to SOMA. The MOSOMA also considers the functions originally presented in the NSGA-II algorithm - non-dominant sorting and crowding distance. All algorithm parameters are listed with a description in Table 5.3.

There are three new parameters with regards to the SOMA added in the MOSOMA. In order to control the process between migrations - the parameter T. The second one defines the

Table 5.3: MOSOMA parameters and optimal values

Label	Optimal value range	Description
$\|P(1)\|$	$\langle 5;12\rangle$*	Initial population size
T	$\langle 5;10\rangle$*	Number of migrating agents
ST	$\langle 2;5\rangle$	Number of steps in one migration
PL	$\langle 1.1;1.7\rangle$	Relative length of path in one migration
PRT	$\langle 0.1;0.4\rangle$	Probability of the perturbation
$N_{\text{ex, min}}$	$\langle 1/3;2/3\rangle$**	Minimal size of the external archive
FFE	User's choice	Number of fit. function evaluations

Note:
* Range is divided by the number of objectives, e.g. $|P(1)|$ range for a two objective problem is $\langle 10;24\rangle$
** Range is divided by the $|P(1)|$, e.g for $|P(1)|$ equal to 30 is the optimal $N_{\text{ex,min}}$ value range $\langle 10;20\rangle$

stopping conditions - the FFE number and the third is the minimal size of the external archive $N_{\text{ext, min}}$.

6 PMASR design

This chapter will present the performance requirements on a permanent magnet assisted synchronous reluctance machine design along with the author's design choices and sacrifices, that were needed to be done in order to achieve manufacture feasibility in a reasonable time. An output of this chapter will be the optimal solution or a set of candidates for optimization.

6.1 Design requirements

As was foreshadowed in the Introduction, the PMASR machine should serve as a low-speed high-torque SPM machine replacement. The motor topology is also considered to use ferrite magnets, therefore the design should result in a high-torque ferrite assisted synchronous reluctance (HT-FASR) machine operating in a low-speed application. The machine should aim at the highest possible efficiency while achieving the same output power within the same dimensions keeping the low manufacture cost. These requirements, as conflicting as may seem, are expected to be at least partially satisfied with the certain trade-offs. The original machine torque-speed characteristic is depicted in Figure 6.1, with two specified working points listed in Table 6.1 a) and b) respectively.

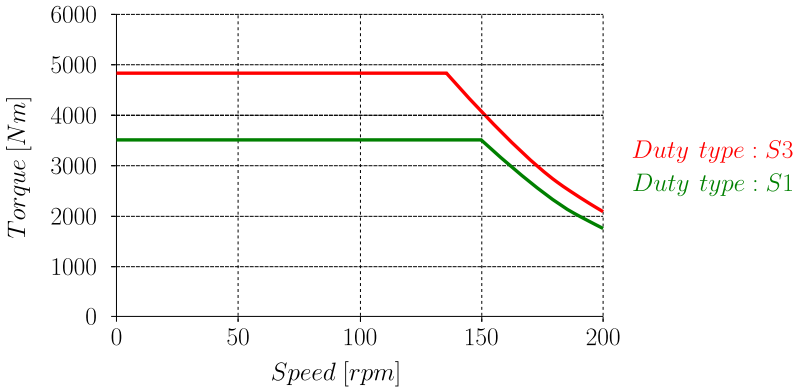

Figure 6.1: Torque-speed characteristics of the SPM machine

6.2 Proposed geometry

The design requirements are aiming for the high-torque machine. According to the chapter 4 can the HT-FASR develop this torque with two principles - either by the PM torque principle

Table 6.1: a) Characteristics of the nominal working point and b) other defined desired point on the torque-speed characteristics

(a)

Parameter	Symbol	Value
Nom. Torque	T_N	3500 Nm
Nom. Voltage	$U_{L\text{-}L}$	400 V
Speed	n_N	100 min^{-1}

(b)

Parameter	Symbol	Value
Nom. Torque	T_N	3500 Nm
Nom. Voltage	$U_{L\text{-}L}$	400 V
Speed	n_N	150 min^{-1}

or the reluctance torque principle. Due to the material characteristics, limited rotor space, and mechanical strength the reluctance torque part is limited to some extent. As mentioned in the fourth chapter, the main part of the FASR machine torque is developed by the reluctance torque. But because of the high torque requirements, the proposed geometry should be aiming for a high PM torque as well. The HT-FASR proposed geometry in the literature [37] or [36] considers the PMs only in the q-axis aiming for the highest magnetic saliency ξ. The proposed geometry by this thesis is using the "full" barrier of PMs risking a partial demagnetization at the barrier ends. The geometry is shown in Figure 6.2.

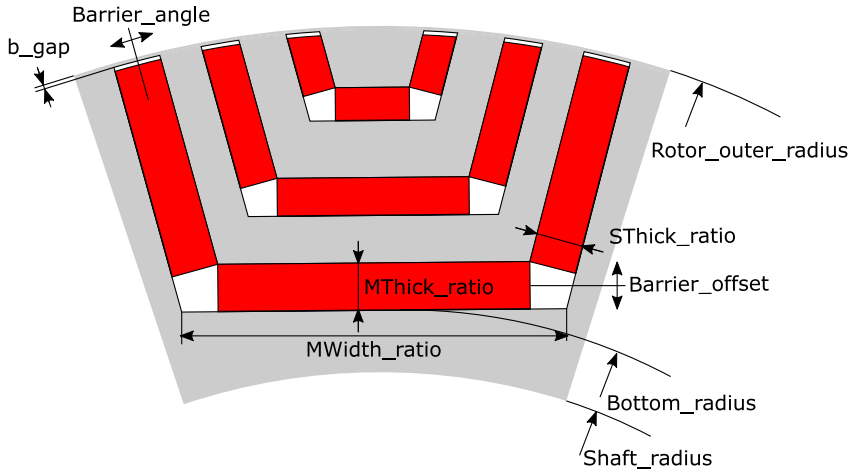

Figure 6.2: Proposed parametric geometry for a HT-FASR analysis and optimization

The proposed geometry has a certain set of parameters specified for each barrier. To achieve a more versatile geometry in terms of dimensions and to lower the probability of barriers colliding in the optimization, dimensionless parameters in the form of ratios were proposed. Parameters labeled as *MThick_ratio* and *SThick_ratio* could be found in the interval $0 \div 1$ and the dimensions of the main and side magnets in the i-th barrier layer are given by the equations (6.1) and (6.2):

$$Main\ magnet\ thickness_i = MThick\_ratio_i \cdot \frac{(Rotor\_outer\_radius - Bottom\_radius)}{Barriers\ number} \tag{6.1}$$

$$Side\ magnet\ thickness_i = SThick\_ratio_i \cdot \frac{(Rotor\_outer\_radius - Bottom\_radius)}{Barriers\ number} \tag{6.2}$$

Similarly to the magnet dimensions, the barriers widths are for the i-th barrier layer expressed by:

$$Flux\ barrier\ width_i = \prod_{n=1}^{i} MWidth\_ratio_n \cdot \frac{(2\pi Bottom\_radius)}{2p} \tag{6.3}$$

The i-th flux-barrier end angle is estimated by:

$$Flux\ barrier\ angle_i = \sum_{n=1}^{i} Barrier\_angle_n \tag{6.4}$$

The other depicted parameters in Figure 6.2 (b_gap and $Barrier\_offset$) are definitive values expressed in millimeters. The proposed parametric geometry has other parameters, such as a number of pole-pairs p and a number of barriers to establish a "rough" geometry, that will serve as an input in the optimization process.

6.3 Search for the ideal slot-pole combination

The slots per pole and phase ratio (q) are some of the most important topology parameters of the electric motor. The optimal value of a q could lead to optimal performance characteristics, such as a high average torque with a low TR or a low total harmonic distortion (THD). Likewise the bad value of q will result in a bad electric motor performance as stated in [182, 183].
Therefore to find an optimal q can be crucial for the whole design process. Since only a small portion of possible combinations was investigated in [37], it was decided to investigate more slot-pole combinations and summarize the whole search throughout the various winding types such as the fractional concentrated winding, both the single-layer fractional slot (FSCW-SL) and the dual-layer fractional slot winding (FSCW-DL) configuration, fractional slot distributed winding (FSDW) and integral slot winding (ISW).
The aim was also to prove the currently investigated combinations in [37], but also to possibly discover new combinations, especially in the concentrated winding types, that could have sufficient characteristics. The advantages of such a combination in concentrated windings (CW) are obvious - a shorter coil overlap and a higher possible slot-fill factor. Both those benefits could lead to the decrease of the Joule losses, which will play a major role in the HT-FASR design losses. The advantages, as are mentioned in [18] is the newly introduced harmonics, that could cause additional losses and a TR reduction. As mentioned in [184], the FASR machines, since combining two torque development principles, while a CW is used in RE type PM excited machines and an ISW is used in SynRel machines, the decision of an optimal winding configuration could be a challenging task. Materials were chosen based on the current price and availability. All models had the same material configuration as listed in Table 6.2.

Table 6.2: List of materials used in the HT-FASR machine design FEA simulations

Part	Material
Stator lamination	M470-50A
Rotor lamination	M330-35A
PM material	PZK 454, Br = 0.34 T at 80°C
Stator winding	Copper at 140°C
Shaft	Stainless steel

6.3.1 Investigated winding types

The comparison windings conditions are:
- Only the randomly wounded stranded winding will be considered.
- Windings must satisfy the coil-overlaps limits (limited housing).

6.3.1.1 Fractional slot concentrated winding (tooth-coil winding)

The fractional slot windings in general could be described by the following equation (6.5):

$$q \notin N \tag{6.5}$$

, where N is a set of integers. The FSCW-DL winding type usually profits from an increased slot filling factor and shorter coil-overlaps, because the coil sides lie in the neighboring slots. Significant amounts of copper could be saved and the manufacturing process of coils could be simplified, as stated in [185], due to the reduced coil-overlap length.
Additionally, to the benefits above stated for the FSCW-DL winding, the FSCW-SL reduces the short-circuit possibility between the phases, since only one coil side is in one stator slot, thus no phase-phase insulation is required in the slot. This could also lead to a further slot-fill factor increase. The FSCW-SL is, unfortunately, a source of higher winding harmonics, that could cause additional Joule and iron losses. Due to the limited dimensions, the investigated number of poles is up to 16 poles and the number of slots is constrained to 24 slots.

6.3.1.2 Integral slot winding

The ISW is characterized by following the equation (6.6):

$$\frac{Q}{mt} = \frac{Q}{mp} = 2q \in N_{even} \tag{6.6}$$

, where the Q is a number of slots, m is the phase number, p is the number of pole-pairs and t is the largest common divider of Q and p. The ISW is, as mentioned above, used with a good results in the SynRel but also in the HT-FASR machines [36, 37]. Therefore it is expected to achieve satisfactory characteristics also in applications considered in this application.
The limited dimensions allow the number of poles up to 16 poles and the number of slots up to 72 slots.

6.3.1.3 Fractional slot distributed winding

The FSDW has been used with the good results in various SynRel or FASR applications such as servo applications [186] or air-conditioning compressors [187]. The motor in [186] uses ferrite magnets and a FSDW winding with The FSDW can be similarly as FSCW-SL and FSCW-DL windings, expressed by equation (6.5). The tested configurations are considered up to 16 poles and 75 slots.

6.3.2 Comparison objectives

The comparison objectives were chosen as follows - the average electromagnetic torque, the TR, the saliency ratio ξ. One additional objective, that has an informative character is called the

reluctance torque ratio (k_{rel}). To reason why were these objectives chosen to this comparison, following equations (6.7) and (6.8) are shown. The electromagnetic torque is for FASR machines, where the q-axis is aligned with the PM described by (4.4) in chapter 4, for easier orientation shown again in (6.7).

$$T = \frac{3}{2} p \left[\psi_{\text{PM}} i_{\text{d}} + (L_{\text{d}} - L_{\text{q}}) i_{\text{d}} i_{\text{q}} \right] \tag{6.7}$$

, where the ψ_{PM} is the PM flux-linkage, L_{d} and L_{q} are machine inductances in the dq-coordinate system, while i_{d} and i_{q} are expressing the currents in the same coordinate system. The TR is evaluated:

$$TR = 50 \, \frac{T_{\text{pk2pk}}}{T} \tag{6.8}$$

, where the T_{pk2pk} is the peak-peak value of the torque behavior.
The coefficient, labeled as the reluctance torque ratio is defined for this paper and further informative comparison. The ratio is in (6.9) and is expressing the portion of the reluctance torque related to the total electromagnetic torque, thus:

$$k_{\text{rel}} = \frac{T_{\text{rel}}}{T} = \frac{(L_{\text{d}} - L_{\text{q}}) i_{\text{q}}}{\psi_{\text{PM}} + (L_{\text{d}} - L_{\text{q}}) i_{\text{q}}} = \frac{(L_{\text{d}} - L_{\text{q}}) i_{\text{q}}}{\psi_{\text{PM}}} + 1 \tag{6.9}$$

The FASR saliency is estimated as the ratio of d-axis and q-axis inductances (6.10):

$$\xi = \frac{L_{\text{d}}(i_{\text{d}}, i_{\text{q}})}{L_{\text{q}}(i_{\text{d}}, i_{\text{q}})} \tag{6.10}$$

6.3.2.1 Rotor and stator in the investigation

The [188, 189] claims, that the geometry topology configuration has a big influence on the machine performance. Therefore to achieve an objectively comparable non-biased comparison, it would be necessary to run a parametric optimization or at least some parametric analysis with an optimal current angle to compare the optimal solutions for each combination. This would clearly introduce an enormous computational and time burden to the process, thus it was decided to use the same rotor topology for the same pole combinations. The optimal current angle, to achieve the maximum-torque-per-ampere (MTPA) control for every slot-pole combination was found. The investigation is done for 4 rotor combination - 10, 12, 14 and 16 poles, all the combinations are depicted in Figure 6.3.

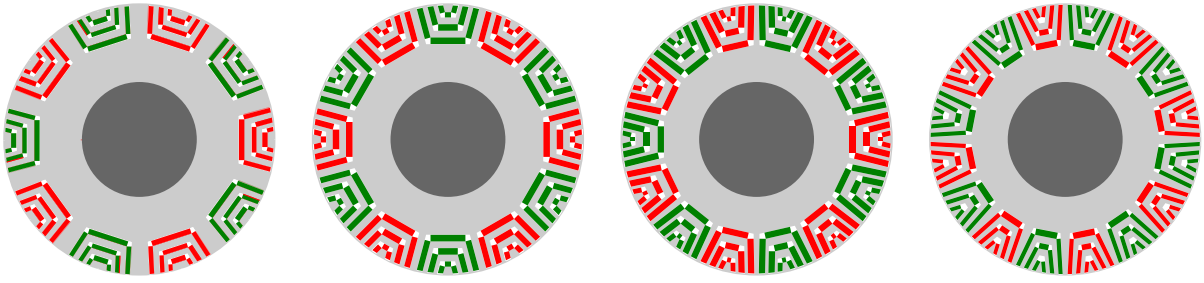

Figure 6.3: Cross-section of the rotor lamination of a) 10 poles rotor, b) 12 poles rotor, c) 14 poles rotor and d) 16 poles rotor.

The winding configurations were chosen based on the demands and limits listed in subsection 6.3.1 and the requirement of a relatively good winding factor. Each configuration has fixed

input energy, the magneto-motive force (MMF), that is derived from the initial SPM machine. The stator geometry is expected to keep the same flux-density B in the important geometry parts, from the design perspective - stator tooth and yoke, as the initial machine (1.8 T, 1.2 T respectively). It can be noted, that the stator EM model does not include the water jacket cooling holes that will later further reduce the stator yoke. The winding combinations are depicted in Table 6.3.

Table 6.3: List of the tested slots and pole HT-FASR combinations with the corresponding q in the brackets

Winding type	Tested combinations (Slots/poles)
FSDW	45/10 (1.5), 54/12 (1.5), 63/14 (1.5) 72/16 (1.5), 75/10 (2.5)
ISW	36/12 (1), 42/14 (1), 48/16 (1) 60/10 (2), 72/12 (1)
FSCW-SL	12/10 (0.4), 15/10 (0.5), 18/14 (0.429) 18/16 (0.375), 24/16 (0.5)
FSCW-DL	12/10 (0.4), 15/10 (0.5), 15/14 (0.357) 18/14 (0.429), 18/16 (0.375), 24/16 (0.5)

6.3.3 Optimal slot-pole combination

The results are structured by the parameters in the relevant tables, where the gray areas are non-tested configurations. The quality of each tested configuration's parameter is also depicted by the color of the cell (correlation), with the displayed objective value.
The first objective is the average torque T and the results are listed in Table 6.4. There are good results between the 36 and 60 slots, while the highest average torque, $T = 3198$ Nm, is found in the FSDW 45/10 combination. Other solid results are found in FSDW and ISW combinations in the range of between 68.6 and 90.5 % of the torque developed by the SPM machine. Among the FSCW-SL and FSCW-DL combinations the developed torque is in the lower range from 49.7 to 72.8 %. In [190] is implied that the torque difference between RE and ferrite machines is around 20 %. The presented comparison demonstrates a smaller torque difference than found in the [190], this could be explained by a different power and speed in both comparisons (in [190] both are conventional).

The results for the TR objective are depicted in Table 6.5. The correlated results are suggesting two approaches, that the designer could take in order to achieve a low TR design. The first is to take a rather conventional approach and choose the higher q number (higher number of slots and lower number of poles), which will result in slot-pole combination, where the working harmonic of the system is identical with the first harmonic. The number of pole-pairs of such a combination is corresponding with the number of coil groups in the stator. The second approach would lead the designer to less conventional configurations, where the number of coil groups is different from the number of pole pairs. The number of coil groups is lower than the pole pairs, therefore the rotor first harmonic has to work on higher stator harmonics. For example, the 18/16 combination has 2 coil groups and 8 pole pairs, therefore the rotor's first harmonic has to "cooperate" with the stator's fourth harmonic, which could be lower than the first harmonic,

Table 6.4: HT-FASR mean value of the electromagnetic torque, while the same configurations of the FSCW-SL and FSCW-DL winding are present, the SL variant is above the DL value.

	Number of poles												
Slots	12	15	18	24	36	42	45	48	54	60	63	72	75
10	1844 1765	2306					3198			2980			2424
12			1757		2994				2756			2591	
14		2235	2052 1901			2599					2455		
16			2575 2369	2432 1971				3167				2562	

resulting in the electromagnetic torque. This would also explain the relatively weak average torque in the first comparison.
An important thing to mention regarding the TR comparison is, that the results are highly dependent on the rotor topology, mostly on the positions of the flux-barrier ends as presented in [191]. Therefore, as mentioned in the introduction of the comparison, the geometry optimization would make this comparison fairer and the differences could be leveled. On the other hand, the higher TR values above 20 % could be with higher probability caused by the bad slot-poles combinations rather than by the non-optimized geometry (with the exception of the barrier count).

Table 6.5: HT-FASR TR comparison, while the same configurations of the FSCW-SL and FSCW-DL winding are present, the SL variant is above the DL value.

	Number of poles												
Slots	12	15	18	24	36	42	45	48	54	60	63	72	75
10	11.79 14.58	20.92					10.51			8.44			4.43
12			16.34		24.21				4.02			45.82	
14		3.24	3.89 4.28			24.76					11.03		
16			4.49 3.13	14.26 18.58				22.71				3.204	

As the last considered objective is the machine ξ presented. The saliency is defined in equation (6.10) as the inductances ratio between the d-axis and q-axis. A design goal is in a case of IPM machines to maximize the machine saliency, that could lead to the reduction of a PM amount to achieve the same torque. The saliency ratio ξ is mostly found comfortably above 1 with few exceptions found in FSCW-SL and ISW windings. The best results are mostly found in FSDW and ISW windings, while the best one is found in 60/10 combination with the saliency ratio $\xi = 5.841$. There is no visible correlation in the results within the poles and in every pole

combination the relatively good results are found (with ξ above 3.5). All results are depicted in Table 6.6.

Table 6.6: HT-FASR saliency ratio, while the same configurations of the FSCW-SL and FSCW-DL winding are present, the SL variant is above the DL value.

	Number of poles												
Slots	12	15	18	24	36	42	45	48	54	60	63	72	75
10	5.521 2.413	2.347					3.039			5.841			3.09
12			2.434		2.242				4.934			2.141	
14		1.486	2.315 3.694			1.639					2.653		
16			3.604 4.359	1.302 3.741				5.294				2.209	

Following the logic steps and understanding of the SynRel machines would lead to the conclusion, that the high saliency ratio has to lead to the higher portion of the torque developed by the machine ξ. The reluctance torque ratio coefficient was therefore stated in (6.9) to support and to offer simple a mathematical expression for this claim. In Table 6.7 are the k_{rel} ratios for all winding combinations listed and correlated.

Table 6.7: HT-FASR ξ, while the same configurations of the FSCW-SL and FSCW-DL winding are present, the SL variant is above the DL value.

	Number of poles												
Slots	12	15	18	24	36	42	45	48	54	60	63	72	75
10	0.382 0.427	0.402					0.874			0.477			0.577
12			0.444		0.442				0.280			0.281	
14		0.230	0.533 0.632			0.439					0.365		
16			0.452 0.317	0.427 0.406				0.423				0.225	

Interestingly there is no visible correlation between the Table 6.6 and Table 6.7 at all. Relatively high saliency ratios (e.g. 18/14 DL version) lead to one of the highest torque ratios, while the best saliency ratio found in 60/10 combination lead to a mediocre k_{rel}. As an explanation could serve the possible high PM-flux, the winding combination, and the influence of the winding factors. Therefore the comparison of winding factors as depicted in Table 6.8 to support such a claim.

Even if the winding factor influence is considered, there is still no relation found between the saliency ratio and the amount of the reluctance torque difference, therefore it can be explained

Table 6.8: Winding factor comparison of tested winding combinations from Emetor tool [192]

	Number of poles												
Slots	12	15	18	24	36	42	45	48	54	60	63	72	75
10	0.966 0.933	0.866					0.945			0.966			0.951
12			0.866		1				0.945			0.966	
14		0.951	0.902 0.902			1					0.945		
16			0.945 0.945	0.866 0.866				1				0.945	

by the different suitability of the winding configuration for such an application. The highest k_{rel} is found in the 45/10 combination while all other combinations deliver less than 65 % reluctance torque in the total electromagnetic torque.
The most favorable winding configurations from each winding type were selected and their toque behavior was depicted in Figure 6.4.

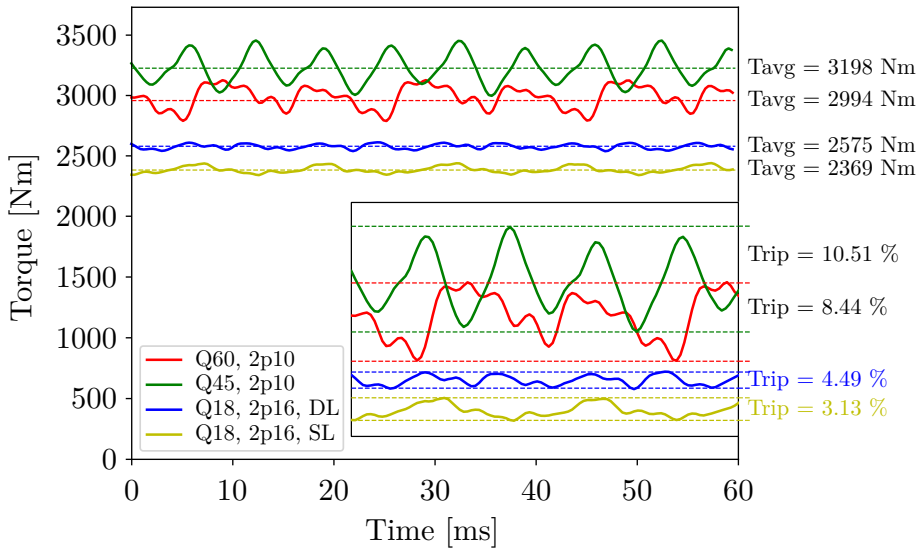

Figure 6.4: Torque behavior of the best geometries from each winding category.

After this comparison, the two decisions were settled. The first one was, that only the FSCW-SL winding will be considered for further design optimization. The second one was to consider the variety of poles in the comparison along with the time-consuming optimization process demand taken into an account.
Therefore the four winding combinations were initially considered:

- FSCW-SL with 18 slots and 16 poles.
- FSDW windings with 45 slots, 10 poles and 54 slots, 12 poles.
- ISW with 60 slots and 10 poles.

The characteristics of these chosen optimization candidates are depicted in Table 6.9 below. Let us note, that none of these machines has been optimized by the OA. The mechanical

Table 6.9: Comparison of the HT-FASR machines with FSDW, ISW and FSCW-SL windings

Model/Objective	**FSDW1**	**FSDW2**	**ISW**	**FSCW-SL**
Number of slots	54	45	60	18
Number of poles	12	10	10	16
Number of stator coil turns	40	40	60	80
Phase current, A	53.0	24.8	22.6	93.1
Magneto-motive force, A	15271	13580	15820	22344
Stator outer diameter, mm	584	584	584	584
Stator inner diameter, mm	485	485	485	470
Stator and rotor stack lengths, mm	374	374	374	374
Electromagnetic torque, Nm	3642.7	3615.6	3528.1	3575.7
Torque ripple, %	6.0	9.4	7.9	5.7
Efficiency, %	84.4	83.0	82.9	78.7
Joule losses, W	9163.9	10392.5	10071.8	13415.5
Core loss, W	840.0	672.0	805.5	1224.3
Phase voltage, V	176.8	183.0	169.2	170.3
PM area, mm^2	27860	25093	25093	40877

losses were estimated as 1% of the output power, as stated in [18]. The cross-sections of chosen machines are depicted in Figure 6.5.

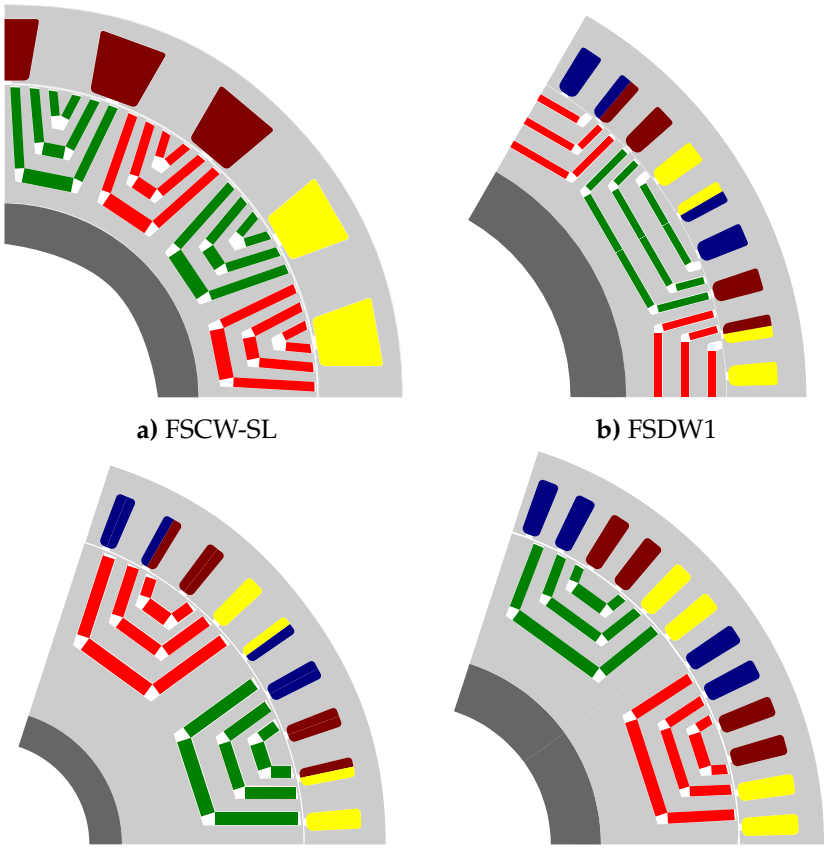

a) FSCW-SL **b)** FSDW1

c) FSDW2 **d)** ISW

Figure 6.5: Cross-section of the compared machines

7 Design optimization

This chapter presents the design optimization of three kinds. The first optimization demonstration will be focused on the comparison of two optimization techniques - the preference based and Ideal multi-objective optimization, tested on two optimization algorithms - the self-organizing migrating algorithm and the genetic algorithm. The second demonstration will be on the previously selected candidates and this optimization will be focused solely on the efficiency and torque ripple. The third optimization will be focused on efficiency and cost, not as an objective, but rather by defining optimization constraints, that are assumed to decrease the manufacturing cost.

7.1 Introduction

In order to simplify the evaluation and optimize the calculation process (shorten the computation time) is to reduce the number of elements in the model. The portion of the model, that is evaluated is guided by the periodic condition. This condition is assuming the field correspondence between two boundary lines (usually two) of the model, while one is chosen as the "Master" (primary line) and the other one as the "Slave" (secondary line). These conditions are assuming some kind of repetition and the evaluated results are multiplied by the number of fractions (a portion of the full model) in the full model. The even and odd periodicity with the highlighted boundary lines are presented on a synchronous reluctance motor in Figure 7.1 [193].

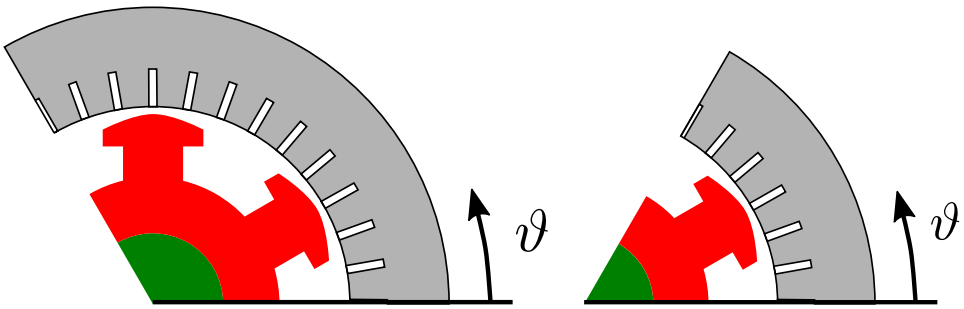

a) Even periodicity **b)** Odd periodicity

Figure 7.1: Examples of a periodicity on synchronous reluctance motor [193]

Due to the further model simplification, therefore radically decreasing the required optimization time, only the significant parts from the EM perspective are modeled (the stator and the rotor) without any mechanical or manufacturing modifications. These modifications will be included in the final machine model.

7.1.1 Optimization work flow

The optimization algorithm workflow is very simple and effective. The whole algorithms are written in the Python programming language for multiple reasons. The first one is, that this language introduces various libraries (in Python terminology called modules) that helps programmers to use e.g. mathematical operations effectively and to export data to external files. The general flow, that is used in all algorithms in this thesis is presented in Figure 7.2.

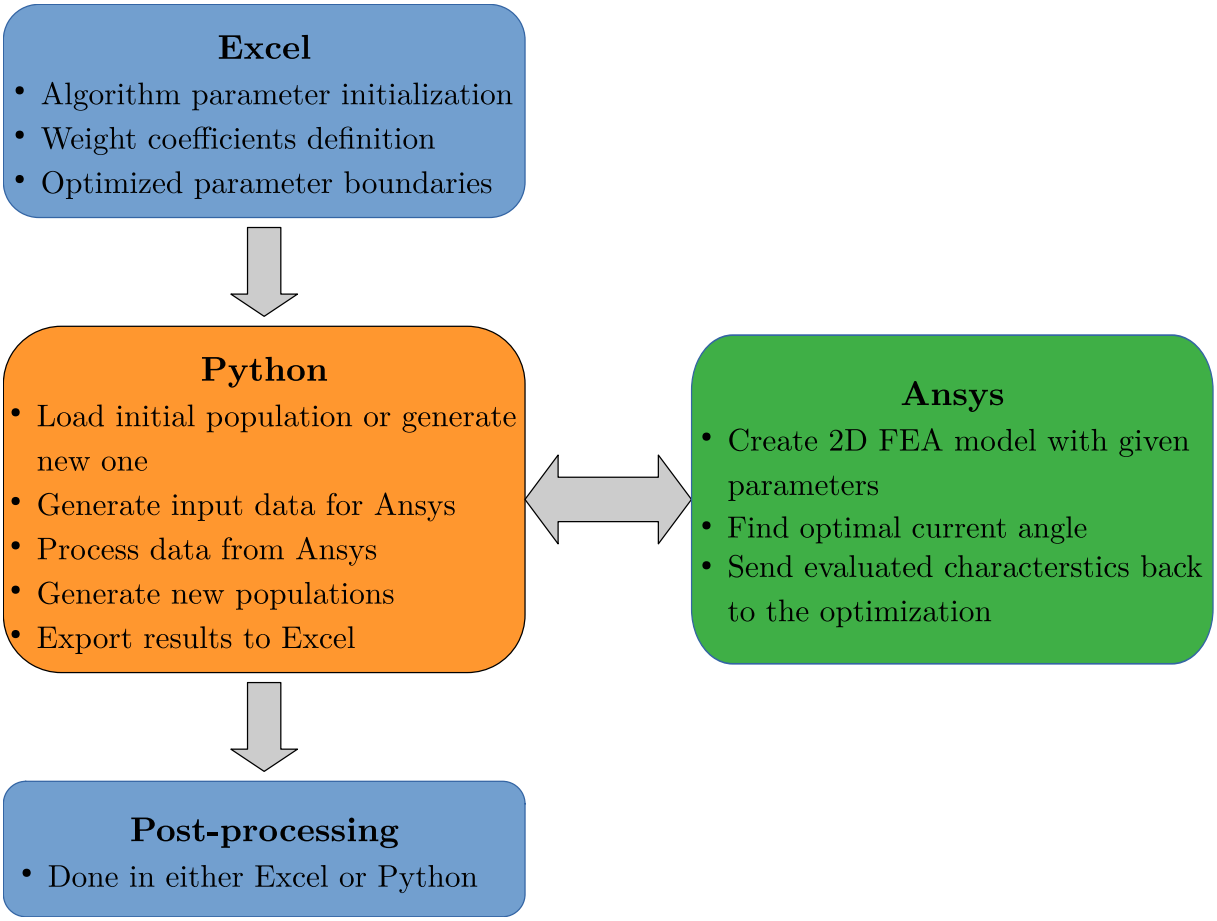

Figure 7.2: Optimization work flow

The parallel calculations are included in the computation procedure, while the Excel file communication is used for easier visualization and post-processing of the data. The current angle is investigated between 40 and 60 °el, where the current angles for the non-optimal models are found.
The main problem of the PBMOO optimization process comes from the principle of the weight coefficients initialization. In order to make a comparison with the ideal MOO procedure more fair, it is convenient to assign weight coefficients with the same value, to "draw" the optimization aim equally to all objectives.

7.2 Preference based versus Ideal multi-objective optimization

The purpose of this chapter is to demonstrate on the electrical machine optimization the claim given in chapter 5. The claim stated, that despite using the same optimization algorithm

on the same optimization problem, the technique (the PBMOO and IMOO) makes a significant difference in searching for an optimal solution. Therefore two algorithms, SOMA and GA, because they can be found in both the PBMOO and IMOO variants, were chosen for the demonstration. The ISW chosen candidate from the previous chapter was chosen, because it is the least computationally demanding model of all the chosen winding combinations (using the symmetry only $1/10$ fraction of the machine is evaluated). The water cooling will be considered in this optimization and will limit the stator outer diameter from the previously considered diameter in the comparison (584 mm) to 627 mm with the cooling.
From all four algorithms, one optimal solution will be chosen. In the case of the PBMOO simply as a solution with the (optimally) lowest cost function value and from the IMOO the decision will be done by the designer with the ideal compromise along with the important objectives. The objectives were chosen - the average torque, TR and the $\cos\varphi$. The TR is defined by the (7.1):

$$TR = 50\,\frac{T_{\text{pk2pk}}}{T}, \tag{7.1}$$

, where the $T_{\max}$ and $T_{\min}$ are the maximum and minimum value of the developed torque. The third objective, $\cos\varphi$, is defined by the (7.2):

$$\cos\varphi = \frac{u(t)\cdot i(t)}{U_{\text{RMS}}\cdot I_{\text{RMS}}}, \tag{7.2}$$

, where the $u(t)$ and $i(t)$ are the instantaneous values of the voltages and currents, U_{RMS} and I_{RMS} are the effective values of the same voltage and current waveforms.
The PBMOO method optimization results will be implemented as the cost function value development over the iterations, while the IMOO will be interpreted with PFs. Since the terms migration and generation are in the GA and SOMA algorithms differently sized (generation is the size of the whole population and migration has the size of the whole population besides the leader multiplied by the number of steps of each migrating individual), and the time to perform the optimization is different as well, the x-axis will be labeled with the FFE.
The first tested scenario is the optimization of all the rotor parameters without any stator parameters. The optimized parameters boundaries and the OA parameters initialization are listed in Table 7.1 and Table 7.2 respectively.

Table 7.1: Optimized parameters ranges first scenario

Parameter	Flux-barrier 1	Flux-barrier 2	Flux-barrier 3
MWidth_ratio, -	$0.2 \div 0.85$	$0.2 \div 0.85$	$0.2 \div 0.85$
MThick_ratio, -	$0.2 \div 0.5$	$0.2 \div 0.5$	$0.2 \div 0.5$
SThick_ratio, -	$0.2 \div 0.5$	$0.2 \div 0.5$	$0.2 \div 0.5$
Barrier_offset, mm	$-5 \div 5$	$-5 \div 5$	$-5 \div 5$
Barrier_angle, deg	$10 \div 22$	$-3 \div 3$	$-3 \div 3$
Bottom_radius, mm		$165 \div 190$	

The PBMOO and IMOO algorithms will be compared to each other - the MOSOMA with the NSGA-II and the SOMA with the GA. The optimization results are fitted into the figures in Figure 7.3 in a form suitable to the optimization technique. Each OA method figure is depicted with the optimal geometries cross-section for a direct results comparison. The cross-sections

Table 7.2: OA parameters initialization

(a)

OA/Parameter	SOMA	MOSOMA	Note.
$\|P(1)\|$	50	50	Initial population
T	-	15	Migrating agents (in the SOMA all members)
ST	20	10	Number of steps taken during the migration
PL	2.1	1.7	Migrating path length
PRT	0.3	0.1	Perturbation
FFE	20,000	20,000	Number of the fitness function evaluations

(b)

OA/Parameter	GA	NSGA-II	Note.
$\|P(1)\|$	50	50	Initial population
Crossover	0.5	0.5	-
Mutation rate	0.2	0.2	-
FFE	20,000	20,000	Number of the fitness function evaluations

are depicted without the cooling holes due to the special cooling arrangement, that cannot be presented to protect the Baumüller product design. The model has the same current loading to have the PBMOO fair comparison the loading was set by the NSGA-II model where the best solution is found.

The optimized results from the PBV are depicted as a development of the cost function value over the individual count, whereas the IMOO algorithms figure depict distributed solutions in the objective space. The optimal solutions are highlighted in all figures with the value of the corresponding objective. The GA algorithm changed the "leader"/best member after each generation, while the SOMA does the same after the whole migration, which is the reason for the visible cost values steps in the figure.
All algorithms except the SOMA algorithm evaluated 20,000 FFE, the SOMA algorithm met the convergence criteria sooner, therefore the algorithm finished. The results clearly show the advantage of the IMOO optimization procedures over the PBMOO approach. Both of the IMOO algorithms sufficiently found solutions, that meet the desired objectives, while the NSGA-II algorithm delivers evenly distributed solutions on and between the PF. The PBMOO algorithms failed to find an optimal solution in this application, the reason could be the high number of optimized parameters, which obviously favors the IMOO solvers.
In the case of the GA algorithm, the model with the lowest cost value was not chosen as the optimal solution, but the model with the higher average torque and the higher TR was chosen instead. In the SOMA algorithm was this "possibility" was not beneficial, therefore the optimal solution was used in the further comparison. This manual process only proves the disadvantage pointed out in the previous chapter, that the optimal solution claimed by the algorithm does not have to be the same optimal solution that the user wants.
The more thorough comparison of the optimal solutions is listed in Table 7.3.

As it is visible from the table, the best solution was clearly found by the NSGA-II algorithm, closely followed by the MOSOMA solution and then the by the user-chosen GA model. The SOMA algorithm, as stated above, found poor results within the set of optimization boundaries.

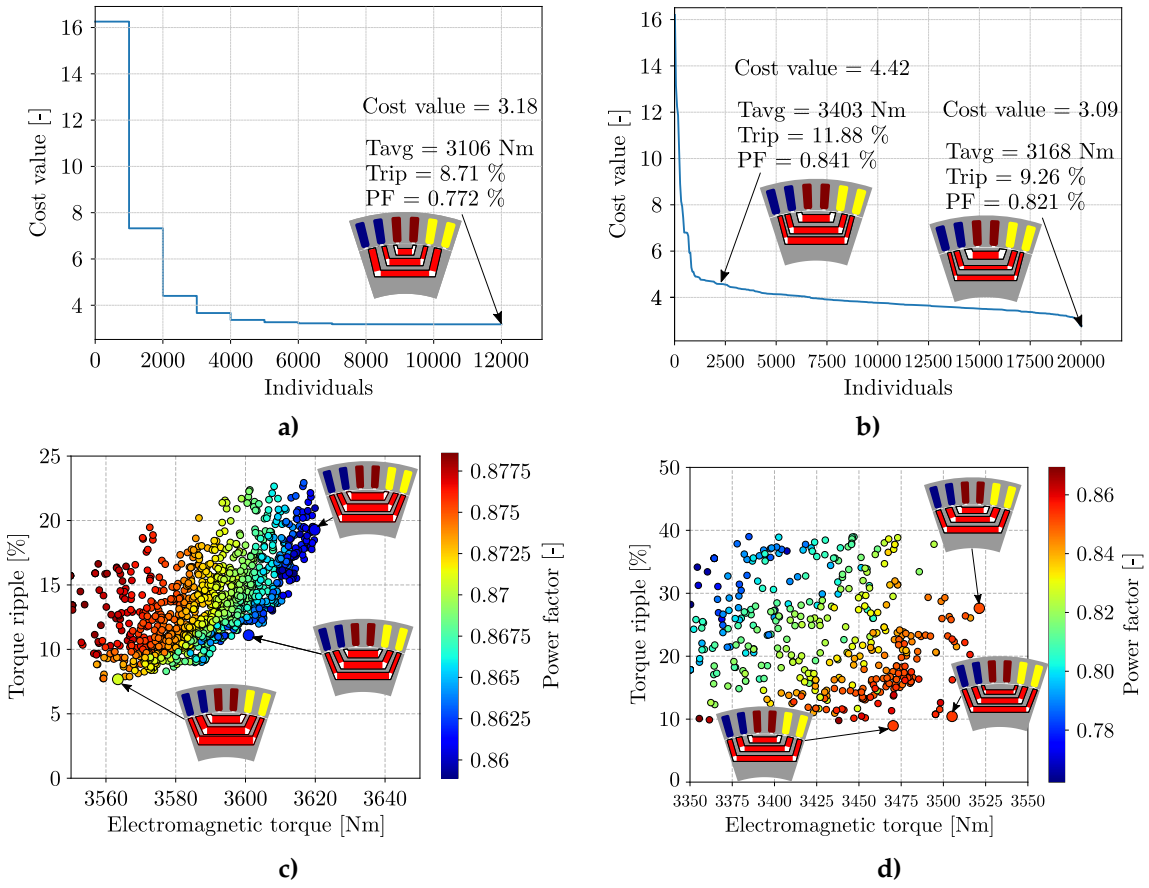

Figure 7.3: Comparison of a) SOMA, b) GA, c) MOSOMA and d) NSGA-II optimization output comparison

Table 7.3: Comparison of SOMA, GA, MOSOMA and NSGA-II optimal solutions

Model/Objective	**GA**	**SOMA**	**NSGA-II**	**MOSOMA**
Electromagnetic torque, Nm	3397.0	3106.5	3601.5	3505.4
Speed, rpm	150	150	150	150
Electromagnetic power, kW	53.4	48.8	56.6	55.1
Torque ripple, %	13.19	8.71	11.11	10.45
Efficiency, %	84.83	83.88	85.64	85.20
Power factor, -	0.84	0.77	0.88	0.87
Joule losses, W	8075.9	8075.9	8075.9	8075.9
Core loss, W	937.7	811.9	851.2	947.7
Phase voltage, V	191.24	190.17	191.38	189.74
Inductance in q-axis, mH	16.13	13.46	18.33	17.58
Inductance in d-axis, mH	38.39	37.81	38.35	38.07
Magnetic saliency, -	2.38	2.81	2.09	2.17
Total line-line voltage harmonic distortion, %	6.25	4.32	7.39	7.58
PM area, mm^2	26442	25297	36259	30525

The best solution found by the NSGA-II is probably caused by the higher amount of the PMs and the higher possible PM-torque in the model, because of the model lowest ξ. The other models have a higher ξ due to the lower inductance in the q-axis, the d-axis inductance and the

saliency ξ are found in the comparison almost identical in all models. Due to the highest torque developed in the NSGA-II optimized model outperforms this solution and the others also in the efficiency and the cos φ objectives.
The worst SOMA results could be possibly caused by the very high (16) number of optimized parameters, which probably caused the algorithm to find only a local optimum instead of the global one. It is vital to say, that due to the unsatisfactory results the PBMOO algorithms had to run multiple times to reach similar results as its IMOO competitors. This fact also speaks for the favor of the IMOO algorithms, that performed very well in this scenario and the results listed in Table 7.3 were found in the first algorithms run.

7.3 IMOO of chosen PMASR geometries

The previous chapter dealt with the optimal slot-pole combinations for the chosen PMASR application. This optimization serves the purpose of designing the machine within the limited volume. The four models, that were chosen are:

- 60 slots, 10 poles
- 45 slots, 10 poles
- 54 slots, 12 poles
- 18 slots, 16 poles

In contrast to the previous section, where only the rotor parameters were optimized, also the stator parameters are included in the process. Stator parameters that were newly introduced were - the stator inner diameter, the tooth width, and the stator yoke height. Due to the linking of the rotor geometry parameters with the main rotor dimensions and poles, the parameter boundaries remain identical throughout the slot-pole combination. The last crucial parameter, that was not linked to the other geometry parameters was the bottom radius. This parameter will be changed according to the stator inner diameter and the controlling parameters. Therefore the stator optimized parameters (k_x ratios) and the bottom radius will be linked with the other dimensions in the following equations (7.3), (7.4), (7.5) and (7.6):

$$k_{stat} = \frac{Stator\_in}{Stator\_out} \tag{7.3}$$

$$h_{\text{slot}} = \frac{Stator\_out - Stator\_in}{2} \cdot k_{hslot} \tag{7.4}$$

$$w_{\text{slot}} = \frac{2 \cdot pi \cdot Slot\_radius}{N\_slot} \cdot k_{slot} \tag{7.5}$$

$$Bottom\_radius = k_{\text{bot}} \cdot (Stator\_in - Airgap). \tag{7.6}$$

Where the $Stator\_in$, $Stator\_out$ are the stator inner and outer diameters respectively and the h_{yoke} is the yoke height. The N_slot is the number of slots and the $Slot\_radius$ is the radius at the bottom of the slot (stator inner radius combined with the slot opening height). The $Airgap$ is the radial length of the gap of air between the stator and the rotor. The ratios k_{stat}, k_{hslot}, k_{slot} and k_{bot} are parameters in the range between $0 \div 1$ defining the other stator dimensions. Since the current model setup would lead to maximizing the stator core area (leading to the lowest magnetic reluctance) and minimizing the slot area, it is necessary to modify it. The decision,

that was taken is to fix the slot current density to the maximal possible current density limited by the water-cooling (7.5 A/mm^2).
Due to using the dimensionless coefficients, the optimized machine parameters are the same for all slot-pole combinations, as depicted in Table 7.4.

Table 7.4: Optimized parameters ranges, second scenario

Parameter	Flux-barrier 1	Flux-barrier 2	Flux-barrier 3
MWidth_ratio, -	$0.2 \div 0.85$	$0.2 \div 0.85$	$0.2 \div 0.85$
MThick_ratio, -	$0.2 \div 0.85$	$0.2 \div 0.85$	$0.2 \div 0.85$
SThick_ratio, -	$0.2 \div 0.85$	$0.2 \div 0.85$	$0.2 \div 0.85$
Barrier_offset, mm	$-3 \div 3$	$-3 \div 3$	$-3 \div 3$
Barrier_angle, deg	$10 \div 22$	$-3 \div 3$	$-3 \div 3$
		Main dimensions	
k_bot, -		$0.75 \div 0.85$	
k_slot, -		$0.4 \div 0.7$	
k_hslot, -		$0.5 \div 0.9$	
k_stat, -		$0.6 \div 0.8$	

Because of the required optimization power and the insufficiency of the MOSOMA in the previous optimization case and an even higher number of optimized parameters the slot-poles combination was optimized only by the NSGA-II algorithm. Especially in the case of the 18/16 slot-pole combination the required optimization power and the time increase to nearly a month of optimization of 20,000 FFEs, which would dramatically increase the comparison time demands.

7.3.1 Optimization objectives and conditions

The objectives estimation will be based on non-linear transient FEA calculations of the PMASR in the steady-state operation due to the use of the AC drive for a smooth start-up operation. The optimization objectives were chosen based on the important performance parameters in the steady-state operation - the electromagnetic torque, the electromagnetic efficiency, the TR, and the $\cos\varphi$.
The first objective is defined as the output electromagnetic power divided by the input electric power.

$$\eta = 100 \cdot \frac{P_2}{(P_2 + P_{Cu} + P_{iron} + 0.01 \cdot P_2)}, \tag{7.7}$$

, where the P_1 is the input electrical power and the P_2 is the output electromagnetic power. The iron losses are increased by the coefficient respecting the manufacturing influence, such as a laser cutting stress induction or a punching stress empirically estimated to 1.5, explained more thorough in [18]. As the second objective, the TR is evaluated from the torque characteristics using (7.1). The third objective that will be taken into account is the $\cos\varphi$, defined similarly as in the previous scenario by the equation (7.2).

7.3.2 Optimization results

Each optimized result will be presented in two figures, thus the eight figures in total. The first set of subfigures in Figure 7.4 depicts the electromagnetic torque versus the TR versus the efficiency objective space with the PF. The three geometries from the PF, a member with the lowest TR, with the highest TR and the member where the compromise is met are highlighted. Along with the highlighted points (bigger markers) are geometry miniatures presented to see the trend that is required to minimize or maximize one objective. The efficiency objective is in the 2D figure depicted by the marker gradient color.

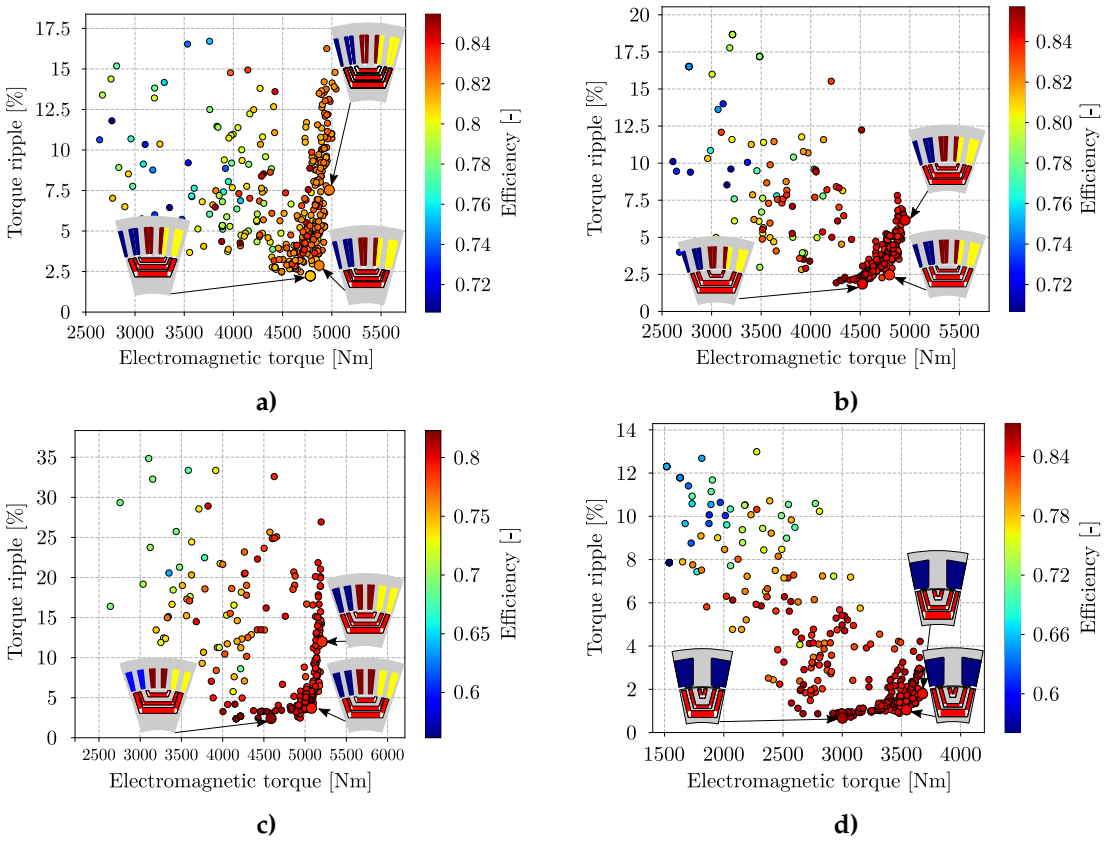

Figure 7.4: The first set of the PF of the optimized slot-pole combinations a) 54 slots and 12 poles, b) 45 slots and 10 poles, c) 60 slots and 10 poles d) 18 slots and 16 poles

The optimization presented some interesting insight into the comparison. From the brief "first look" comparison is obvious, that all models achieve a lower TR and relatively high torque. The efficiency objective comparison is currently not very objective due to the significant difference between the models. The figures are therefore depicting the trend of efficiency, where the higher objective values are found close to the first PF and are decreasing with the lower torques. The maximal TR for the optimal model in each slot-pole combination was limited to 15 %. In the case of FSDW and FSCW-SL models is this condition satisfied even with the models, that were labeled as the "highest TR" within the first PF. In the ISW case some "compromise" was needed to be found, but because of the PF's shape was the difference between the "highest TR" and the optimal model torque relatively small. To the chosen models for the comparison will be referred to as the optimal models. Considering the same current density in the stator slot the highest electromagnetic torque of the optimal model is found as the ISW model. The optimal model achieves 5219 Nm of torque, which is about 5 % higher than the 45/10 FSDW

combination (4958.4 Nm), nearly 7 % than the 54/12 FSDW combination (4817.7 Nm) and 29.1 % higher than the FSCW-SL (3700 Nm). The highest efficiency is at the same current density found in both the FSDW. The optimal models are recalculated for the nominal torque (considering some safety margin of 200 Nm), which is achieved by the FSCW-SL model in the optimization. The different shapes of the geometries on the first PF are found in all ISW and FSDW optimizations due to both the reluctance torque and the PM-torque combination, that is suppressed in the case of FSCW-SL models highly in favor of the PM-torque. The models on the first PF differ mainly in the stator inner diameter, flux-barrier/PM thicknesses, and in the width of the third (outer) flux-barrier, which highly influences the TR behavior.
The second set of figures depicts similar figures replacing the efficiency with the cos φ objective. The second set is shown in Figure 7.5.

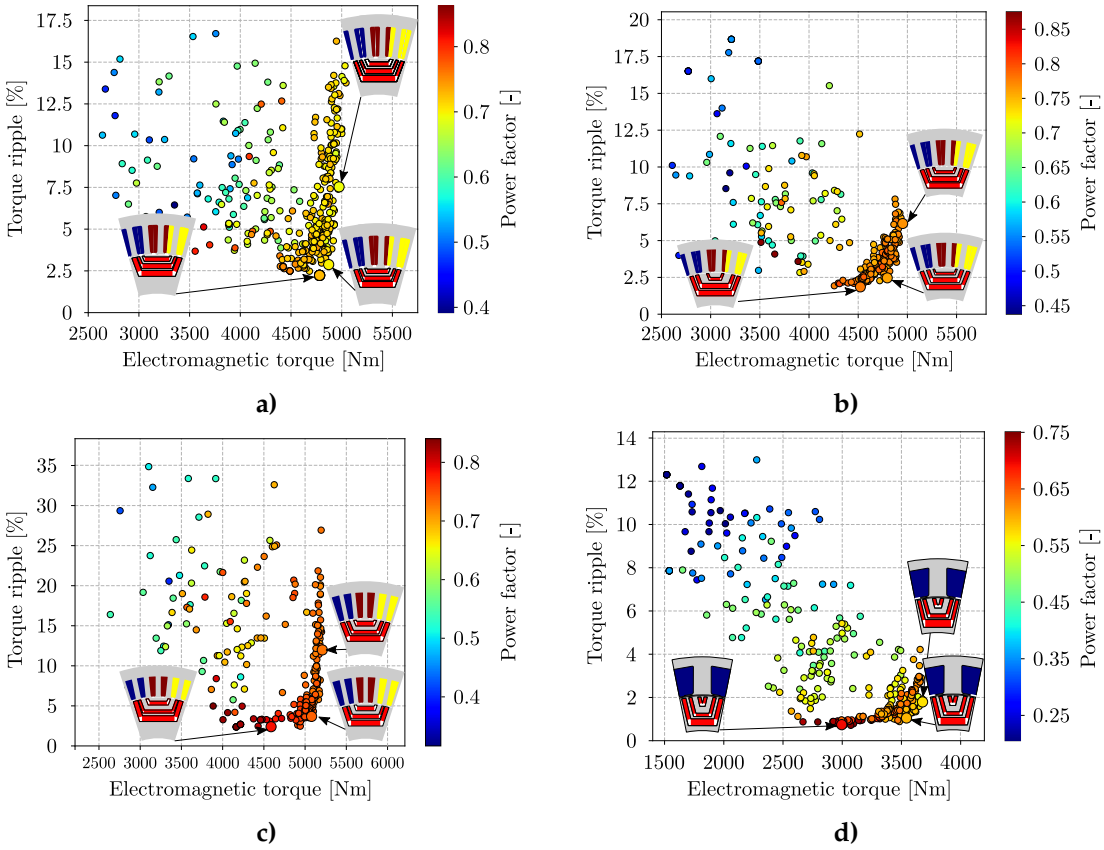

Figure 7.5: The second set of PFs of the optimized slot-pole combinations a) 54 slots and 12 poles, b) 45 slots and 10 poles, c) 60 slots and 10 poles d) 18 slots and 16 poles

The cos φ shows a similar trend to the efficiency objective. All the ISW and FSDW models have a relatively high cos φ, while slightly higher values are found in the case of ISW. The lower cos φ is found in the FSCW-SL models, because of the lower ξ and higher fundamental working frequency (using the third harmonics to develop a electromagnetic torque, mentioned in chapter 5). The rest of the optimized models have satisfactory cos φ values - above 0.8.
The optimal models had to be recalculated, as mentioned above, modifying the current density to achieve the desired torque. The recalculated models along with other important objectives are listed in Table 7.5. To differ the two FSDW combinations, will be to the 54/12 referred to as the FSDW1 and to the 45/10 will be labeled as the FSDW2.

The table depicts only the first harmonic of the supplying voltage, thus the reserve of nearly

Table 7.5: Comparison of HT-FASR machines with FSDW, ISW and FSCW-SL windings

Model/Objective	**FSDW1**	**FSDW2**	**ISW**	**FSCW-SL**
Number of stator coil turns	52	60	85	80
Phase current, A	24.88	24.72	17.85	59.49
Magneto-motive force, A	15664	14832	15190	19158
Stator inner diameter, mm	405.2	398.3	397.3	442.4
Electromagnetic torque, Nm	3753	3726.8	3754.3	3700
Speed, rpm	150	150	150	150
Electromagnetic power, kW	58.95	58.54	58.97	58.13
Torque ripple, %	3.15	5.4	4.0	5.0
Efficiency, %	89.4	89.5	90.1	84.9
Power factor, -	0.79	0.89	0.88	0.47
Joule losses, W	8776	7963	8387	11579
Core loss, W	791.6	811.9	513.5	1056.0
Phase voltage, V	171.9	179.6	171.2	178.5
Inductance in q-axis, mH	6.6	10.3	18.4	9.3
Inductance in d-axis, mH	9.5	36.5	72.0	11.9
Magnetic saliency, -	1.44	3.53	3.92	1.29
Total line-line voltage harmonic distortion, %	4.25	7.87	6.31	26.44
PM area, mm^2	21287	25093	26498	29850
Copper weight, kg	78.7	79.3	88.9	76.4

50 V considered for the potential presence of the higher harmonics in the system.
The table comparison paints a better and broader picture of the whole optimization comparison. Given the same desired torque equality/similarity are the results more comparable and the previously estimated efficiency and the cos φ objectives suddenly become more objective. Even though in the previous figures the ISW model was lacking both the efficiency and the cos φ the model has currently the highest efficiency and a slightly lower cos φ and has the lowest THD. The cons for such geometries could be considered a relatively higher amount of copper and magnets, which could lead to the potentially higher price.
The FSCW-SL model brings the worst performance into the comparison. As the biggest disadvantage is the efficiency, which is almost more than 5 % lower than found in the other models, this, of course, leads to higher losses that need to be removed from the machine by the cooling when delivering the same output power. The algorithm draws the FSCW-SL model to higher rotor outer dimensions increasing not only the volume of PM but also the rotor inertia. The other FSDW geometries introduce very comparable results as the ISW counterpart. These models achieve a higher cos φ, a lower saliency ratio ξ with a smaller volume of PM and copper to be potentially cheaper than the ISW machine, considering only these two commodities.

7.4 Limited optimization scenario

In a contrast to the previous chapter, showing the potential limits of the machine follows the limited case optimization scenario.
The limits were introduced after the previous optimization was performed and were introduced to reduce the testing prototype price. The limits were as follows:

- Fixed stator to the manufacturer standards
- Fixed PM height

The company that was responsible for the manufacturing was Baumüller. Baumüller is a German manufacturer with headquarters located in Nürnberg offering the broadest portfolio of electric motors both with or without the PMs. Since the Baumüller company produces only one stator with the same number of slots from the previous comparison, it was decided to optimize the ISW combination considering the limits. The cooling, that is considered in the machine remained the same as for the standard unit. The Joule losses, that the cooling is sufficient to remove from the stator were based on the previously manufactured units and were slightly (around 10%) increased to deliver the desired power. Without the current increase, the difference compares to the initial SPM machine would be even bigger.
The PM height had to be at the moment fixed to the standard height due to the limited amount of time for production and other manufacturing restrictions.
Therefore there had to be the new optimization parameters restricted to the parameters listed in Table 7.6.

Table 7.6: Optimized parameters ranges thirds scenario

Parameter	Flux-barrier 1	Flux-barrier 2	Flux-barrier 3
MWidth_ratio, -	$0.2 \div 0.85$	$0.2 \div 0.85$	$0.2 \div 0.85$
Barrier_offset, mm	$-5 \div 5$	$-5 \div 5$	$-5 \div 5$
Barrier_angle, deg	$10 \div 22$	$-3 \div 3$	$-3 \div 3$
k_bot, -		$0.75 \div 0.85$	

Since the number of parameters has decreased due to the limitations, it was possible to use both the MOSOMA and the NSGA-II algorithms. Therefore the third scenario will be focused on the comparison of the two IMOO algorithms with a smaller amount of parameters (10) compared to the first scenario (16). The algorithm settings are shown in Table 7.7.

Table 7.7: MOSOMA and NSGA-II optimization parameter values

Label	MOSOMA	NSGA-II	Note.
$\|P(1)\|$	50	50	-
T	15	-	-
ST	10	0.5	Crossover in NSGA-II
PL	1.7	-	-
PRT	0.1	0.2	Mutation rate in NSGA-II
FFE	20000	20000	-

The optimization delivered non-satisfactory results regarding to the requirements. The optimization was not able to find a solution with the desired torque and efficiency. The nominal torque had to be reduced to the 3390 Nm at the nominal speed of 150 rpm.
The optimization with the limited boundaries finished with the relatively good results, the MOSOMA being faster and found slightly worse results, that confirm the conclusions drawn in [194]. When comparing both optimization results PFs, it is obvious, that the first PF of the NSGA-II algorithm optimization is denser at the front and delivers slightly better results. The

MOSOMA has more distributed results over the searched space. The average torque vs. TR vs. efficiency figures of both optimization are shown in Figure 7.6.

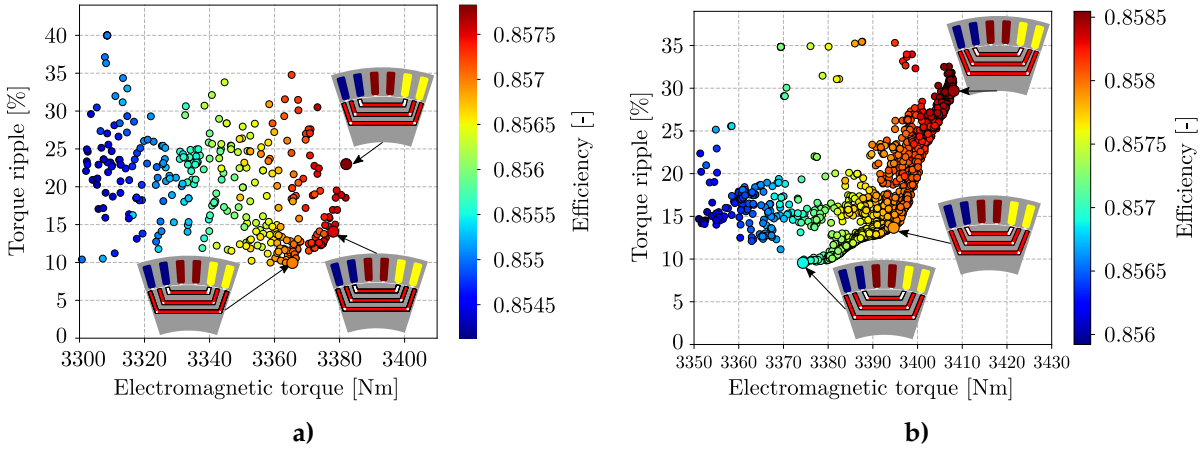

Figure 7.6: The first set of PFs of the limited optimization scenario of 60 slots, 10 poles, HT-FASR machine with the efficiency gradient objective a) MOSOMA and b) NSGA-II

Both optimal solutions have very high efficiency and therefore the reasonable solution to the lower than the desired torque would be to increase the stator current and risk a decrease in efficiency. But because of the already high current density (increased compared to the original machine) and therefore possibly over exceeding the cooling abilities will not the current increase be considered in the following analysis. The following Figure 7.7 presents the average torque vs. TR vs. cos φ.

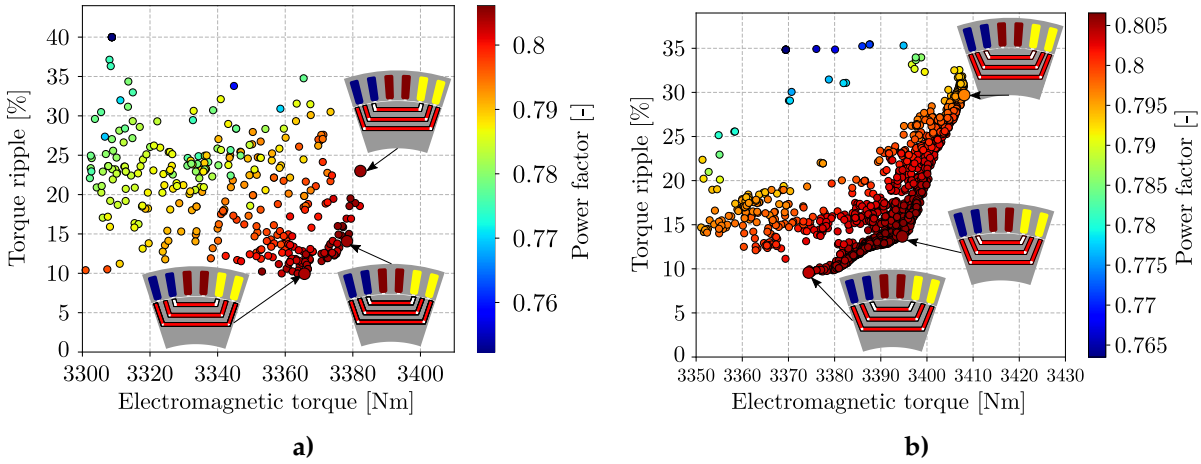

Figure 7.7: The first set of PFs of the limited optimization scenario of 60 slots, 10 poles, HT-FASR machine with the cos φ gradient objective a) MOSOMA and b) NSGA-II

The other set of PF's depicts very similar situation to the previous comparison. The NSGA-II found the solutions with a slightly higher PF, with the difference being (based on the color gradient scale) lower than 0.05. The chosen optimal solutions objectives are compared in Table 7.8.

The desired torque of 3500 Nm at 150 rpm was not achieved due to the optimization limitations, therefore the rated torque had to be decreased to 3395 Nm at the same speed, and the optimized NSGA-II.

Table 7.8: Comparison of the MOSOMA and NSGA-II optimal solutions

Model/Objective	NSGA-II	MOSOMA
Electromagnetic torque, Nm	3395	3377.5
Speed, rpm	150	150
Electromagnetic power, kW	53.33	53.05
Torque ripple, %	14.3	14.9
Efficiency, %	85.09	85.03
Power factor, -	0.823	0.822
Joule losses, W	8075.9	8075.9
Core loss, W	739.04	737.67
Phase voltage, V	194.1	193.8
Inductance in q-axis, mH	15.5	15.5
Inductance in d-axis, mH	38.9	38.9
Magnetic saliency, -	2.51	2.51
Total line-line voltage harmonic distortion, %	8.78	8.54
PM area, mm^2	21779.5	21860.8

7.5 Final optimized motor analysis

The chosen optimized geometry was then analyzed more thoroughly in the dq-axes system. The analyzed characteristics were delivered both in a wide range of currents and at the rated point.

7.5.1 *Dq* mapping analysis

And the most important machine objectives were mapped to investigate the machine behavior in the second quadrant of the dq-system. The stator current distribution is shown in Figure 7.8.

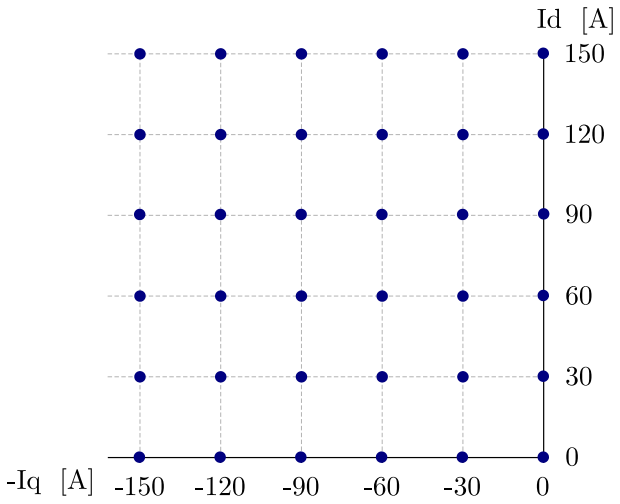

Figure 7.8: dq-currents distribution in the dq-analysis

As the mapping objectives/characteristics it was decided to choose the following:

- Direct(d) axis inductance map - $L_q(I_d, I_q)$

- Quadrature (q) axis inductance map - $L_{\mathrm{d}}(I_{\mathrm{d}}, I_{\mathrm{q}})$
- Efficiency combined with the torque-speed characteristic
- Power-speed characteristic

The first depicted characteristics are the L_{d} and L_{q} inductances maps on Figure 7.9 a) and b) respectively.

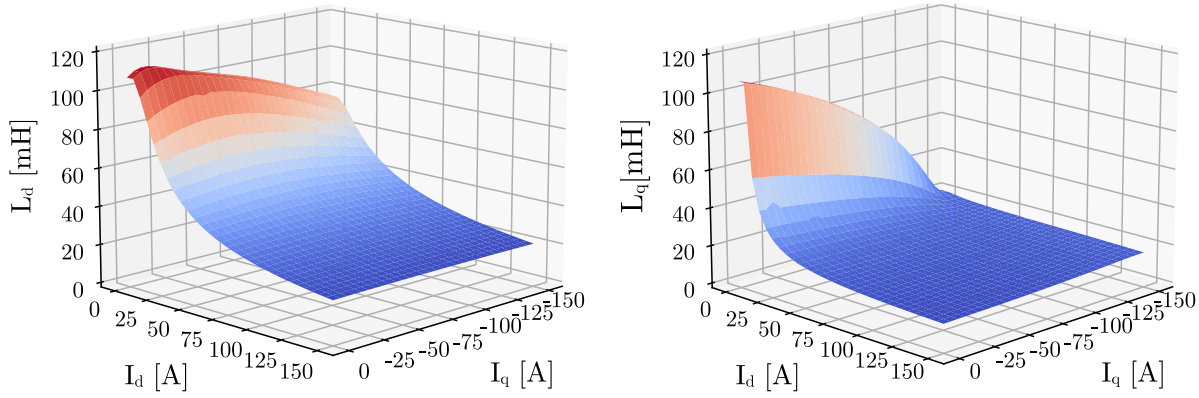

Figure 7.9: a) d-axis and b) q-axis inductance dependences on d- and q-axis currents

The inductance map resulted in the shape, as expected, as a combination of the PM and SynRel machines with the inclination toward the second machine type. For the comparison served the publications [195] and [196], where the IPM d and q inductances in a map form, SynRel dq inductances characteristics respectively were presented. The both inductances are highly dependent on the currents (SynRel characteristics as presented in [195]), but still preserving the IPM characteristics in a form of the concave function with one high point in the d and q axes intersect (both currents have zero values) as shown in [196]. Both these inductances present a good flux-weakening possibilities. This is presented in Figure 7.10 in the both torque vs. speed in Figure 7.10 a) and power vs. speed characteristics in Figure 7.10 b).

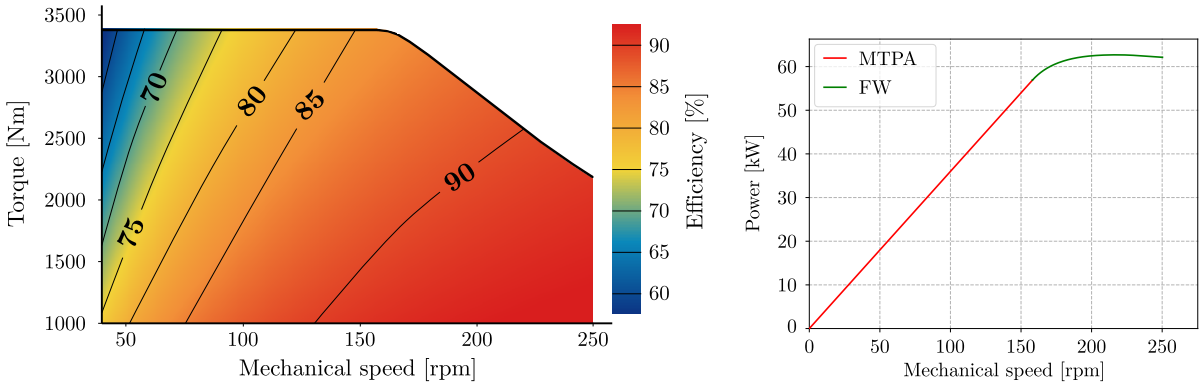

Figure 7.10: a) Torque-speed combined with the efficiency map and b) the power-speed characteristics of the optimized machine

The presented torque-speed characteristic shown, besides a relatively good field weakening possibilities, a good efficiency reaching 90 % at a higher speed. The field weakening starts higher than the rated speed, almost right when the output power reaches the (previously assumed)

rated power of 55 kW. The field weakening region is in the power-speed characteristics distinct by a different stroke color, in the torque-speed characteristics by the knee of the constant characteristic.

7.5.2 Rated point analysis

Further is the machine behavior at the rated speed analyzed and discussed while the most important characteristics were considered:

- The torque behavior comparison derived by the Maxwell tensor and the *dq* derived quantities
- The PM and the reluctance torque parts behavior
- The harmonic analysis of the maxwell torque
- The *dq* inductances behavior
- The line-line voltages and their FFT analysis.

The EM torque behavior affects various motor characteristics and a high torque variation (TR) could lead in certain frequencies to a decreased bearing lifetime, a higher vibration, or noise resulting in an unsatisfactory application experience. Therefore was the torque analysis was performed including the analysis and the results are depicted in Figure 7.11.

The mean values of both torque behaviors are very similar (3372 Nm vs 3374 Nm), but the TR decreased in the torque derived *dq* quantities and is about 9 %, which is nearly 5.5 % lower than in the behavior estimated from Maxwell tensor (14.43 %). The reluctance torque part (visible in Figure 7.11 b) in a blue stroke) has a higher mean value (1841 Nm) and is estimated by the second part of equation 4.4 and has a lower TR. The PM-torque would be, according to the same equation, constant, but for the purpose of this analysis is estimated as the difference between the torque estimated by the Maxwell tensor and the reluctance torque estimated by the inductances in *dq*. Thus this behavior has a higher TR and a lower mean value than the other torque part, the equation 4.4 based PM-torque is presented for comparison as well.
The torque spectrum presented in Figure 7.11 c) presents the torque frequencies up to the 50^{th} order. All the frequencies, except the second one, are the multiplies of the 6^{th} harmonic order, that is in agreement with the [18].
The next characteristics, that are drawn in the comparison are the *dq* inductances analysis in Figure 7.12.

The both inductances behavior are influenced by the slot openings and the resulted saliency is very close to the saliency listed in Table 7.8, the slight nuances could be caused by different time-steps. because, the final analysis was performed with the shorter time step.
The last analysis was focused on the line-line voltages and their Fourier analysis. Both these characteristics are shown in Figure 7.13 a) and b) respectively.

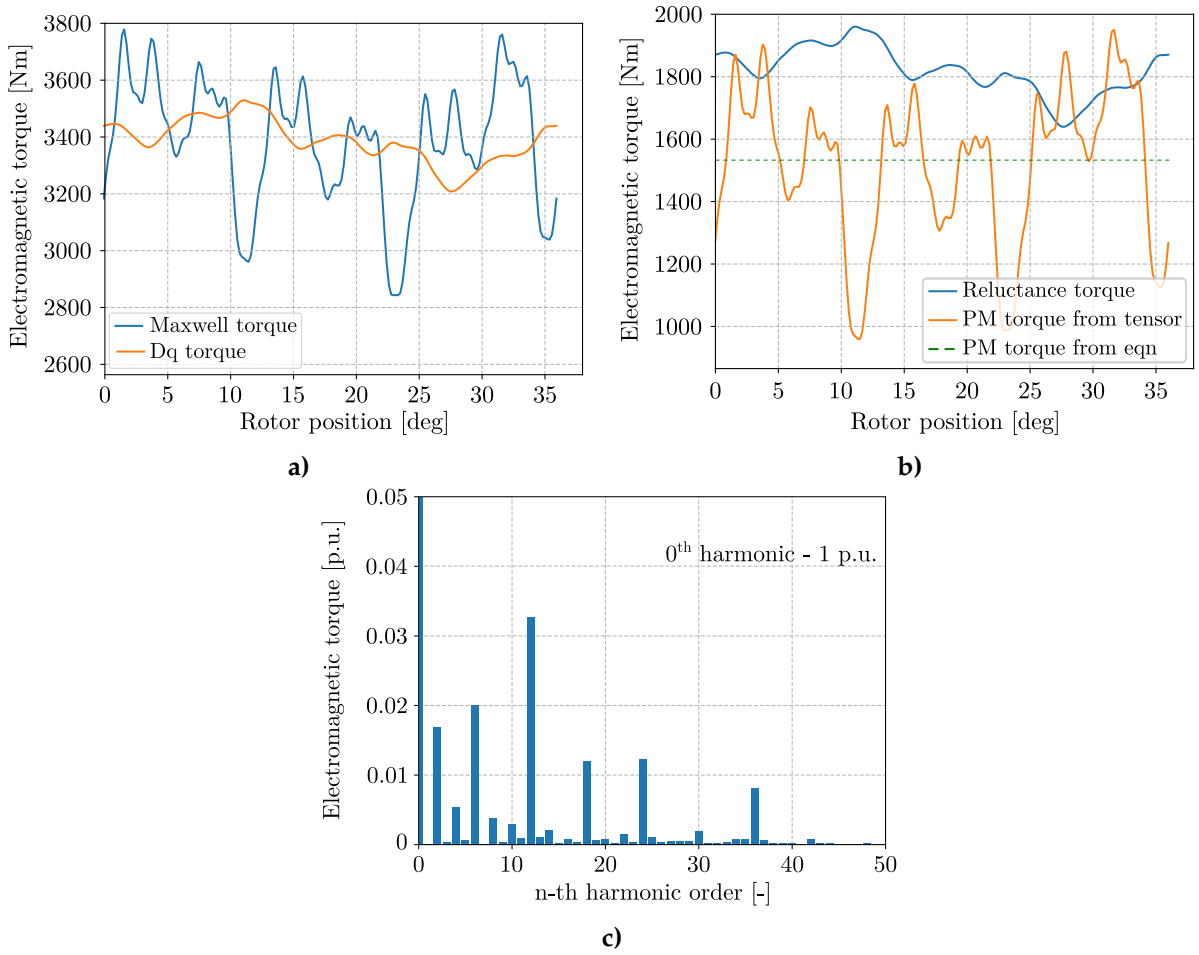

Figure 7.11: a) Electromagnetic torque behavior estimated from the Maxwell tensor and *dq*-coordinates, b) Electromagnetic torque divided into the components and c) FFT of the electromagnetic torque

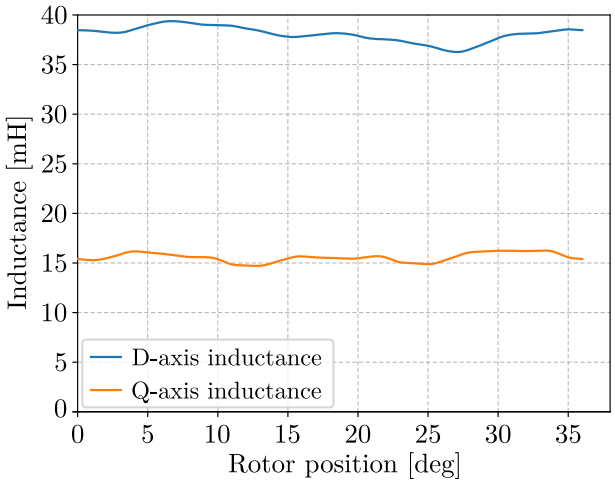

Figure 7.12: *dq*-inductances behavior

The line-line voltages express a smaller distortion than the phase voltage. This is clear when comparing the first harmonics of the phase and the line-line voltages. In the case of the phase voltage (listed in Table 7.8) the first harmonic is equal to 194.1 V and from the Figure 7.13 the first

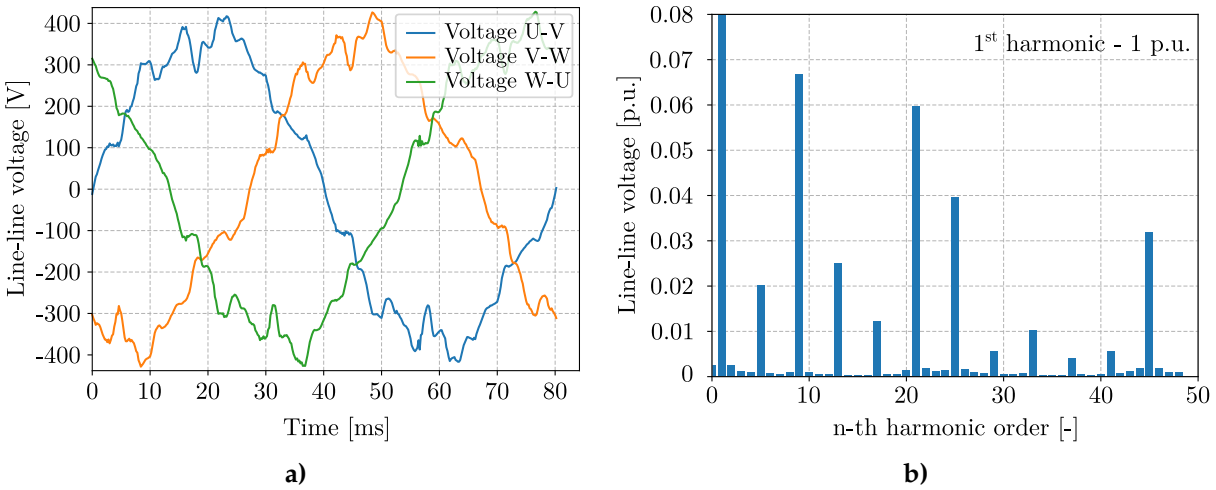

a) **b)**

Figure 7.13: a) Line-line voltage vs. time characteristics and b) the FFT of the line-line voltage

line-line harmonic is 369.9 V. The "standard" ratio, used also in [18], is $\sqrt{3}$ (= 1.707), is different from the ratio between line-line and phase voltage, in this case $\frac{369.9V}{194.1V} = 1.905$. The THD is equal to 8.78 % with the dominant harmonics being 5, 9, 13, 17, 21, 25, 45. The 5^{th} and 13^{th} harmonics are caused by the winding distribution, 9^{th} and 21^{th} are caused by the rotor pole number and 25^{th} with 45^{th} is caused by the number of coil groups of each phase.

8 Measurement

The following chapter deals with the measurement of the high-torque ferrite assisted synchronous reluctance machine. The test bench with the accessories is presented along with the tested machine. The measured characteristics with the data are listed in the tables for different working points of the machine.

8.1 Introduction

Two challenges laid before the HT-FASR measurement. The first one is that based on the literature research, there has been no measurement done on a HT-FASR machine, or at least no measurement data were published. Thus there was no anticipation of the results or a test bench ideal configuration to perform such a test. The second one was set due to the relative difficulty of obtaining the testing equipment. Since the machine operates at a high torque from a low speed, no "conventional" dynamometer could be used as a testing load of the machine. Fortunately, measurement equipment used for testing the mining systems such as boring machine drives in T-Machinery in Ratiškovice, Czech Republic was used. These drive trains, similarly to the designed HT-FASR machine, operate at low speeds with higher torque, therefore the testing benches were ideal to use. The laboratory also included water loop cooling accessories for machine cooling, thus the motor could be tested at the rated point without restrictions. The test with no water cooling at half of the output power was also performed. This test was required by the manufacturer as a standard requirement test for Baumüller electric motors.

8.2 Machine modifications

Since the manufactured machine is used to validate the EM model, it was decided to manufacture a shorter 306 mm stack length version. This decision was done to reduce the cost of the comparison while achieving the same aim - the FEA model validation. Besides the final model modifications (mechanical and manufacturing) were the water cooling canals included in the machine stator yoke. The last modification, that was done in the final machine, was the magnet division in the axial as well as in the radial direction. The final machine visualization is depicted in Figure 8.1.

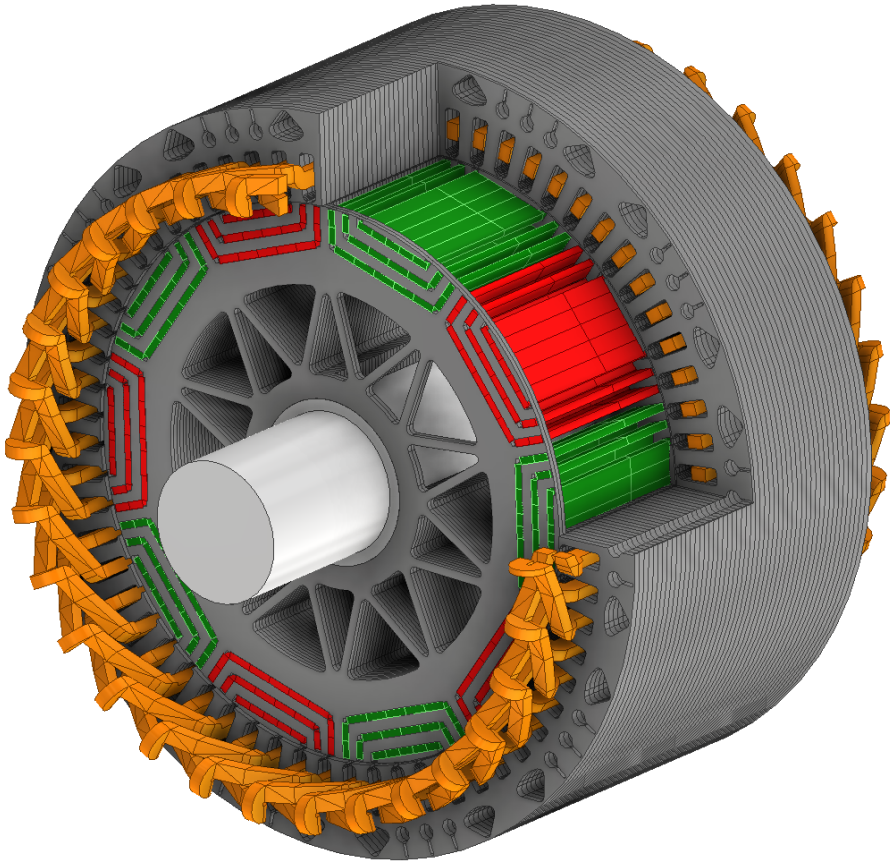

Figure 8.1: 3D sketch of the optimized machine

8.3 Testing bench

The measurement equipment could be divided into three categories:

- Motor driving and cooling accessories
- Measuring equipment of the mechanical objectives
- Measuring equipment of the electrical objectives

All the data from the measurements were handled by the PC, where the communication between the measuring instruments was managed. Besides the measurement data, the control of the water circuit and the dynamometer was also done either by the computer or by the connected accessories.

The mechanical measurement consisted of the developed shaft torque and the rotational speed of the coupled drive. The mechanical measurement was done by the VUES ASD P500 along with the provided accessories from the same manufacturer. The dynamometer provided the loading torque of 3183 Nm from the minimal speed 150 rpm. The data sheet of such a dynamometer along with the important characteristics is in Attachments. The dynamometer was connected via the native software with the working PC, as depicted in Figure 8.2.

The cooling measurement data were the cooling water flow rate, the water pressure, and the water temperature in the reservoir. All the water cooling circuit characteristics were kept constant during the tests as defined by the manufacturers requirement based on the used cooling pipeline arrangement. The measuring devices were built by the company, where the testing bench was located.

The measurement of the electric objectives was done by the power analyzer Yokogawa 1800

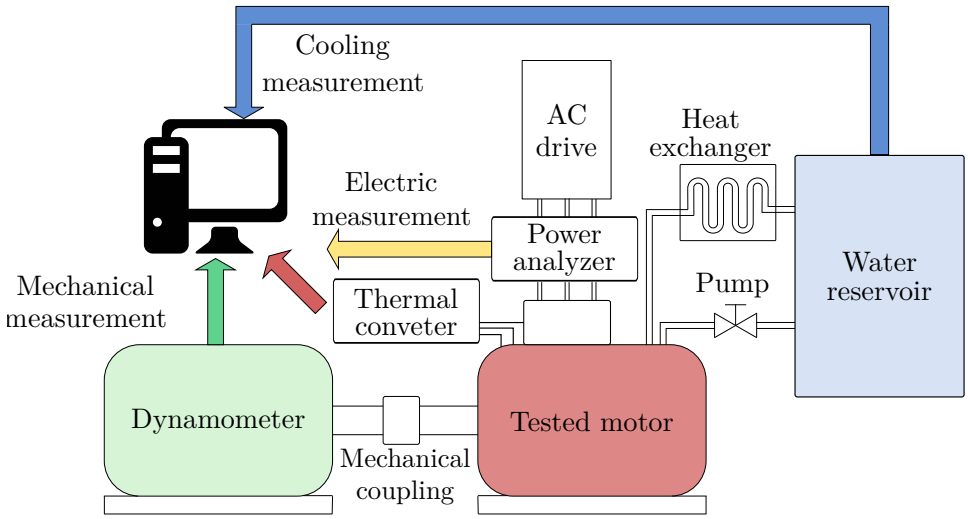

Figure 8.2: Schematics of the testing bench

coupled with the LEM current sensors and, as the figure implies, was connected to the PC and is controlled by the VUES software. The Yokogawa is used for the load tests as well as for the winding resistance measurement to determine the actual winding temperature by the resistance measurement. An electric contractor (not shown in Figure 8.2) was inserted between the AC drive and the Yokogawa to safely disconnect the AC drive from the electric motor to perform the resistance measurement after each test.
The probe converter serves the purpose of converting various temperature probes (in our case the K-type thermocouples and PT-1000 temperature probes) information into the values in the degrees of Celsius. The thermocouples were used for a contact temperature measurement and PT-1000 temperature probes were located in the stator winding. The contact measurement was done on both motor shields, where the bearings are mounted, one thermocouple was used for the resolver temperature measurement and the last one was used for the housing temperature measurement. The placement for the housing temperature measurement was chosen to avoid the location neighboring the cooling pipes, which would significantly influence the measurement because the maximal housing temperatures were aimed to be measured. The winding temperature was measured by the two randomly placed temperature probes into the stator winding. Therefore the real winding temperature could be affected by the probe placement. Therefore the resistance measurement was done after each step in the specific time period to approximate the actual winding temperature from the obtained resistance value and the known value at room temperature.
The testing bench photographs with the device labels are depicted in Figure 8.3.

8.4 AC drive setup process

After the test bench setup comes the AC drive configuration. The AC drive used for the tested application was the Control Techniques Unidrive M700 with a peak output power equal to 90 kW. This drive is capable of controlling both the PM (Nonsalient) and the SynRel (Salient) machines and includes a variable load angle option.
The initial setup was obtained by the "Auto-tune" option, in a salient mode, and according to the results was aimed to find the d-axis of the controlled machine (the lowest electromagnetic torque). The strategy was to supply the stator winding with a current, that rotates the rotor into

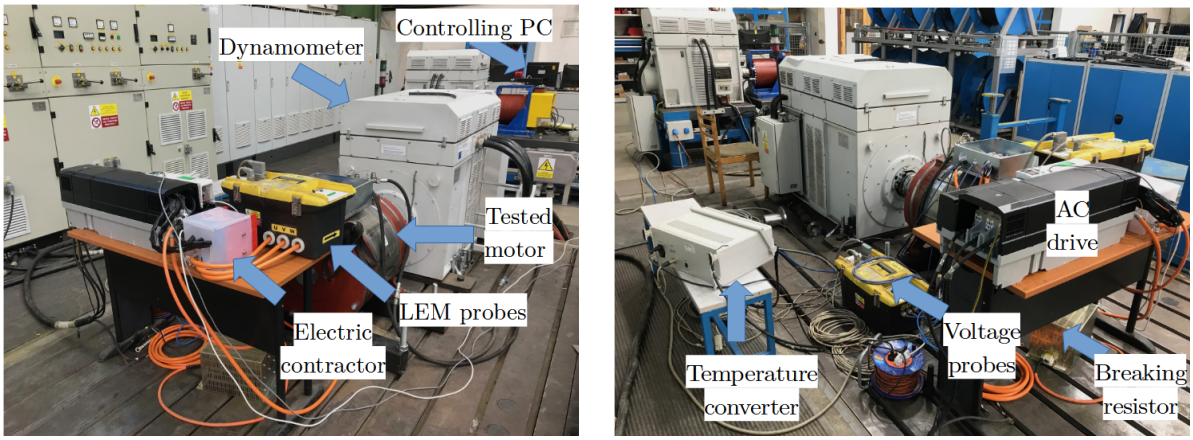

Figure 8.3: Testing room viewed from the right and left with the labeled devices.

the "Zero-torque" position, that the system assumes as the stator and rotor *d*-axis alignment. Since the PMASR machine combines both principles PM and reluctance torque, it is difficult to choose the suitable alignment procedure and decide which principle is more significant in such a machine. Due to the use of ferrite magnets, it was decided to use the salient mode. The figures below in Figure 8.4 a) and b) depict the torque vs. current angle characteristics theoretical situation, that is based on the different behavior - the peak torques at the different current angles and the double "torque variation" of the reluctance torque compared to the PM torque. The behaviors in the figures are divided into parts based on the torque principles and the maximum values in theoretical behaviors are derived from the FEA model. The maximum torque value of the torque parts with respect to the combined maximum torque is 59 % in the case of reluctance torque, 48.4 % in the case of the PM torque respectively.

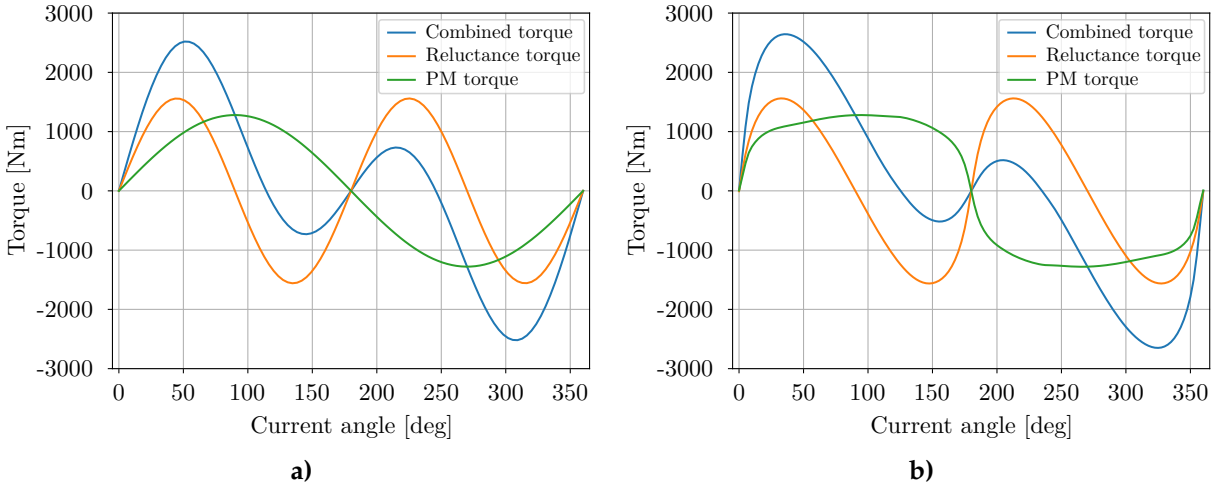

Figure 8.4: a) Torque versus current angle in the PMASR - the theoretical behavior, b) Torque versus the current angle divided into the torque parts - the FEA model.

The different PM torque curve in the FEA model could be caused by the PM pole arrangement. The theoretical approach considers the sinusoidal flux-density distribution in the air-gap. The combination of the two principles introduces uncertainty into the AC drive setup process. The "ideal" situation, where only 3 intersections of the torque-angle curves with the x-axis became more complex and 2 additional intersections are introduced due to the different reluctance

and the PM principles behavior.
The situation was solved in the laboratory conditions by monitoring the rotation direction (to investigate if the developed torque is positive or negative with respect to the dynamometer configuration) and the drained current at the specific torque (evaluating the torque/motor constant). The drained current to develop a certain torque (torque/motor constant) is clearly higher in the case of the smaller torque curve (added due to the principle described above). It can be noted, that the intersections, caused by the reluctance torque and the distance between them are affected by the saliency ratio (the peak value of the reluctance torque), the shape of the magnetic circuit, that is, in this case, distorting the theoretical sinusoidal shape into the almost rectangular shape. The last influence on the intersection could be found in Figure 8.5, where the torque vs. current angles curves was analyzed with a different stator current. This situation was also simulated in the optimized machine with the variation of the stator current from 20 A to the nominal 114 A. Figure 8.5 c) from [197] support such a claim, even though the NdFeB magnets in were used in the publication.

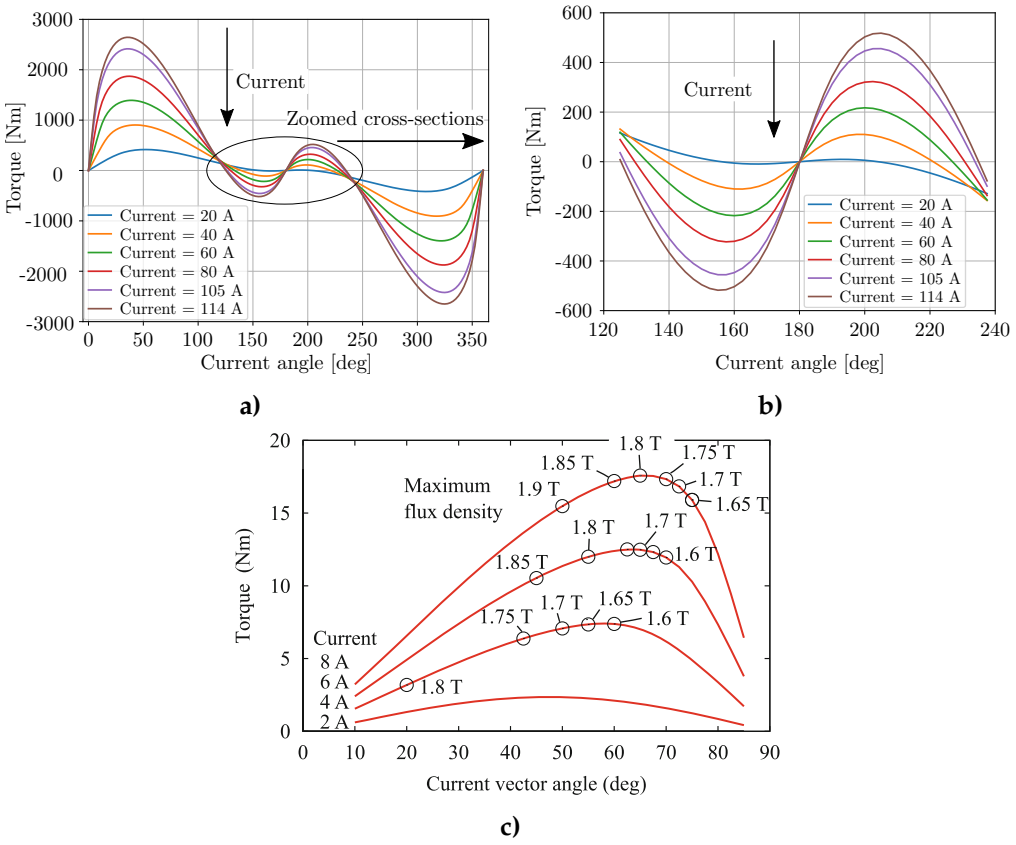

Figure 8.5: a) Torque versus current angle in the PMASR, b) zoomed torque versus current behavior around the 180° angle, c) theoretical behavior with NdFeB from [197].

Therefore the additional torque curves and the x-axis cross-sections cannot be fully mitigated by the decreased stator current used in the setup procedure and a more experimental approach was needed to correctly configure the drive.

8.5 No-load measurement

The no-load measurement consists of the resistance and the back electromotive force (back-EMF), both at the room temperature and their verification with the FEA calculations. Mostly to eliminate the manufacture faults i.e. significantly different number of stator coils turns from the model or significant turns difference between the coils. The second manufacturing fault, that could be diagnosed from the no-load measurement is the potential PM demagnetization caused by the manufacturing process, possibly by the faulty magnetization or by any other damage, that could have been caused by the magnet or motor transportation e.g. shattering of PM elements (PM corners or edges). The measured values and the FEA estimated values are compared in Table 8.1.

Table 8.1: FEA estimated and measured back-EMF

Voltage / Speed, rpm	FEA, V	Measured, V	Difference, %	Error, %
50	40.7	44.5	8.5	0.267
75	61	66.5	8.3	0.267
100	81.3	88.6	8.2	0.267
150	122	132.7	8.1	0.267

Relatively big differences are found in the measured back-EMF, where the measured back-EMF values are on average almost 8.3 % higher than estimated by the FEA. This could be caused by the usage of slightly stronger ferrite magnets or by a higher value of magnetization, which was unfortunately not measured before the manufacturing.

The resistance measurement at the room temperature along with the FEA comparison is depicted in Table 8.2, where the measured value is considered to be more accurate.

Table 8.2: FEA estimated and measured resistances

Resistance / Phase comb.	FEA, mΩ	Measured, mΩ	Difference, %	Error, %
U-V	289	293.9	- 1.67	0.267
U-W	289	294.3	-1.8	0.267
V-W	289	294.2	-1.77	0.267
Average	289	294.1	-1.75	0.267

The measured and estimated resistances values are very similar due to the relatively precise FEA model configuration and close communication with the manufacturing company, that delivered the coil-overlaps dimensions, that was adapted into the model.

8.6 Measured working points

The whole measurement procedure was divided into several measurements. Since many working points were measured and the whole measurement was done in few days, it was necessary to add checking procedures, that ensure the non-faulty motor state, especially the PM demagnetization. The state of PM was verified by the measured terminal voltage induced

back-EMF.
The list of the measured points (MP) is presented in Table 8.3 and the resulted torque-speed characteristics with the labeled MPs are shown in Figure 8.6.

Table 8.3: Measured points of the machine

Speed	Cooled	Not cooled
50 rpm	2777 Nm	1388.5 Nm
75 rpm	2777 Nm	-
100 rpm	2777 Nm	-
150 rpm	2777 Nm	1388.5 Nm

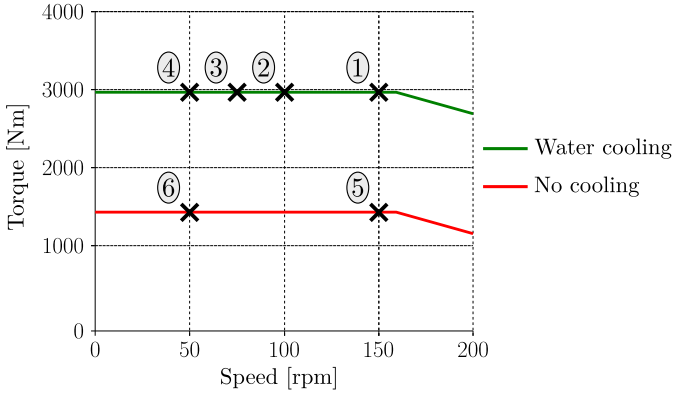

Figure 8.6: Measured working points of optimized machine

Each measurement contains the temperature development over the measurement, the resistance measurement after each MP and the comparison of FEA estimated and measured data. The cooling circuit satisfied the required parameters i.e. system pressure of 6 bars at the water temperature range from 10 to 25 °C for the whole measurement. Throughout the measurement was the water temperature kept around the higher limit - 25 °C.

8.6.1 First measured point

The first MP was at 150 rpm and the expected torque was 2777 Nm at the stable operating temperature, by the standard [198] considered the temperature not exceeding the change of 2 K in an hour. The measurement was sped up by injecting the higher current at the beginning of the measurement and then decreasing the current to reach the desired temperature increase of 100 K, which is required by the Baumüller company. Figure 8.7 a) depicts the current and the temperature development over the whole measurement, and Figure 8.7 b) shows the stator winding "cooling" curve, where the characteristics are extended to the potential temperature at the end of the measurement.

The machine reached its thermally balanced state at nearly 200 minutes since the test started. From the characteristics, it is obvious, that the electric machine cooling cannot sufficiently remove the heat generated by machine losses at the nominal (estimated) load. Therefore the load current had to be decreased to the level, where the cooling was sufficient and the nominal current had to be therefore decreased. The final measured characteristics (at the end of the test) are listed and compared with the FEA model in Table 8.4.

These measured characteristics support the initial claim stated in chapter 4, where the 30 % motor volume increase was required to achieve the same output power. In other words, the machine can in the same volume achieve about 30 % lower output power, compared to the SPM. In this case study the output power decrease is about 19 % lower when compared to the initially designed machine - $1 - \frac{2365.5\ \text{Nm}}{2777\ \text{Nm}} \cdot 100 = 14.9\,\%$. The estimated errors (uncertainties) were derived from the Yokogawa official site [199] guide and from the uncertainty of the current and voltage sensors. The biggest errors can be found in the case of the measured current and

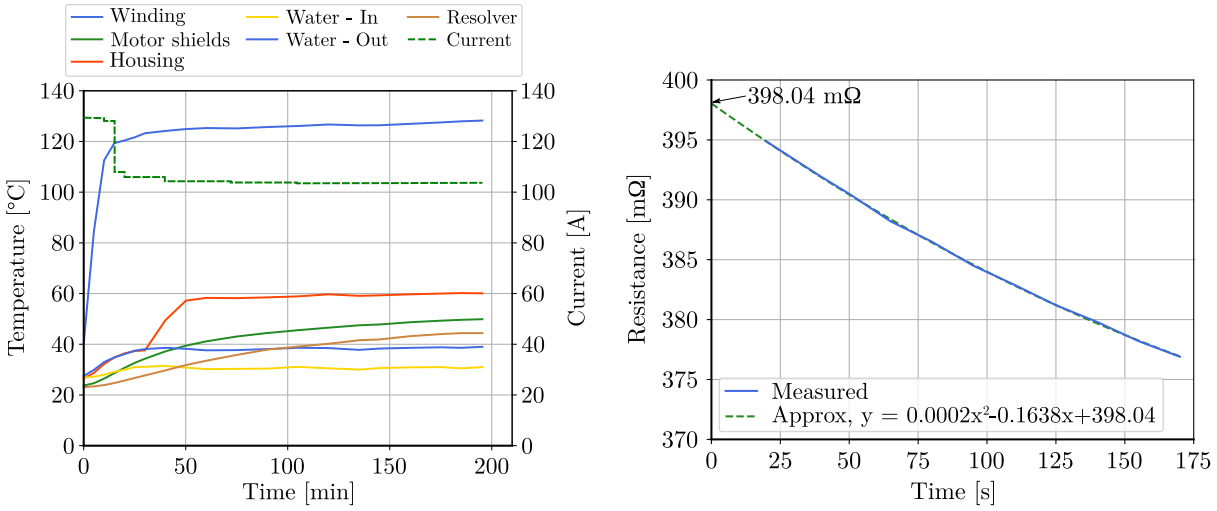

Figure 8.7: a) Temperature and current development during the first MP measurement b) Winding resistance characteristics after the first measurement.

Table 8.4: First MP measurement

Method / Objectives	FEA	Measured	Difference, %	Error, %
Torque, Nm	2362.7	2365.5	0.12	0.05
Speed, rpm	150	150	0	0.02
Current, A	103.7	103.7	0	2.89
Current angle, °el	55	54	-1.85	-
Voltage, V	296.7	316.1	6.14	0.289
Saliency ξ, -	3.52	7.58*	-	-
Input power, kW	44.47	47.58	6.54	1.08
Power factor, -	0.81	0.84	3.57	1.08
Output power, kW	37.1	37.1	0	0.05
Efficiency, %	83.46	81.6	-1.86	1.08
Winding temperature PT-1000, °C	128.2	128.2	0	0.1
Winding temperature from resistance, °C	-	110.6	-	1.08
Magnet temperature from Back-EMF, °C	81.42	81.42	-	0.213
Room temperature, °C	-	26.4	-	0.15

* Note: The magnetic saliency is roughly estimated from AC drive measurement. The measured value is, based on the difference, measured with significant error.

are estimated as 2.89 %.

The measured and the FEA characteristics differences are found in each characteristic except the ones, that were set in the model to validate the FEA accuracy (i.e temperatures, currents). The maximal difference is found in the input power, which "combines" the most uncertainties from other measurements (e.g. currents, voltage, power factor). The measurement was done using the MTPA (maximum torque per ampere) control, thus the same approach was taken in the case of FEA, thus the difference between the current angles. The FEA model achieved the MTPA at a slightly different angle.

The model saliency comparison, even though was measured, is not the objective, since the measurement error would be over 200 %. This is caused, as noted in Table 8.4 by the rough AC drive estimation. The saliency was still listed in the table, solely to point out the significant

measuring error of the AC drive and therefore to propose a rather skeptical consideration of this measured value.
The measured efficiency was nearly 1.9 % lower than estimated by the FEA model. This could be caused by the presence of the higher harmonics injected by the AC drive or by lower mechanical losses, that were estimated as 1 % of the output power, which is a conventionally approved value, and also by [18].
The measured back-EMF was in an average about 9.5 % lower for the same speeds as listed in Table 8.1, that corresponds to the PM temperature increase of 55.02 °C, resulting in the PM temperature of 81.42 °C. The temperature estimated from the resistance measurement is 110.6 °C, which is about 17.6 °C lower than the PT-1000, this could be caused by the sensor placement, but also by the non-equal cooling characteristic of the winding in time. At the beginning is the winding temperature changes steeper and the gradient decreases over time.
The machine housing thermal state was documented with the thermal-camera and the images are shown in Figure 8.8 below.

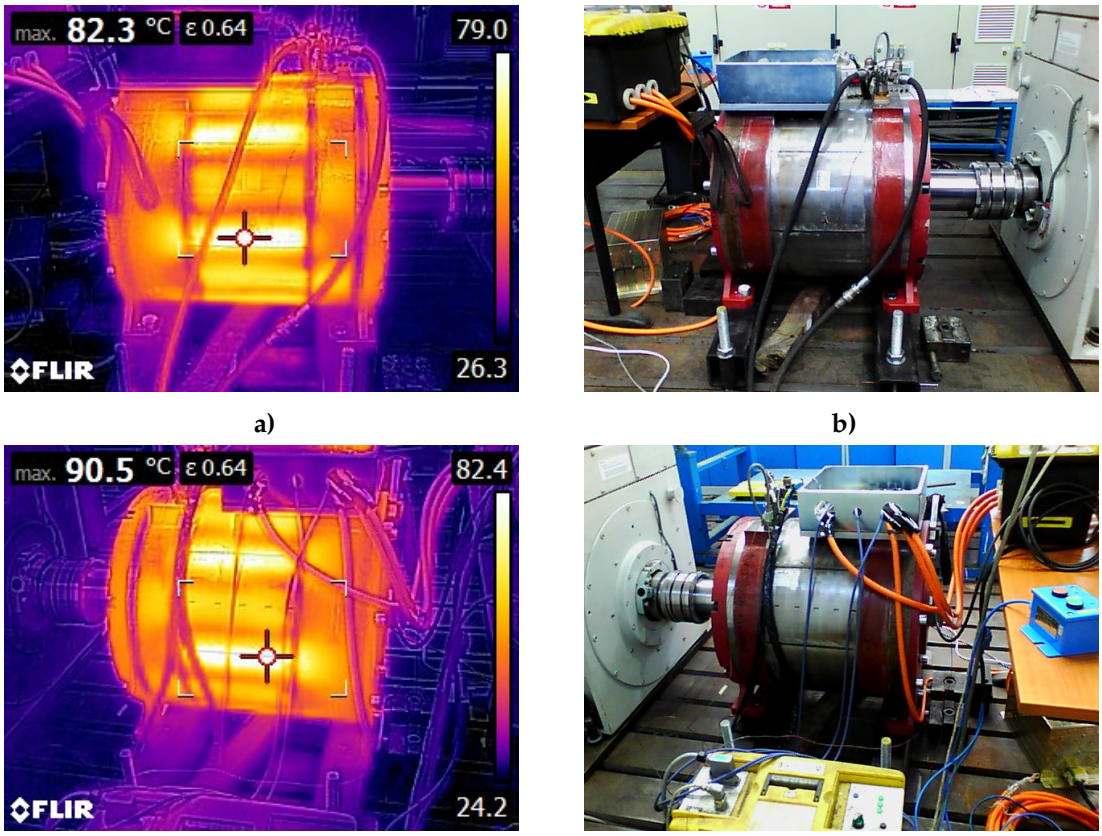

Figure 8.8: Thermal-camera images for the MP at 150 rpm, machine with active cooling a) Right side thermal image from the thermal-camera b) Right side real image from the thermal-camera, c) Left side thermal image from the thermal-camera d) Left side real image from the thermal-camera.

The hottest spot, that the camera was pointed to was equal to 90.5 °C and is located on the left side of the machine.

8.6.2 Second measured point

The second MP took place right after the first point measurement, hence the higher initial temperatures in Figure 8.9. The second point is characterized by 2777 Nm at 100 rpm, that is the same amount of the torque at the lower rotational speed, compared to the first point. The measurement was done using the same approach as the first MP. It was expected to reach a slightly higher electromagnetic torque, due to the possible decrease of the iron losses and the increased loading current (to achieve the same amount of machine losses). The temperature development and the after-test resistance measurement including the approximation are depicted in Figure 8.9 a) and b) respectively.

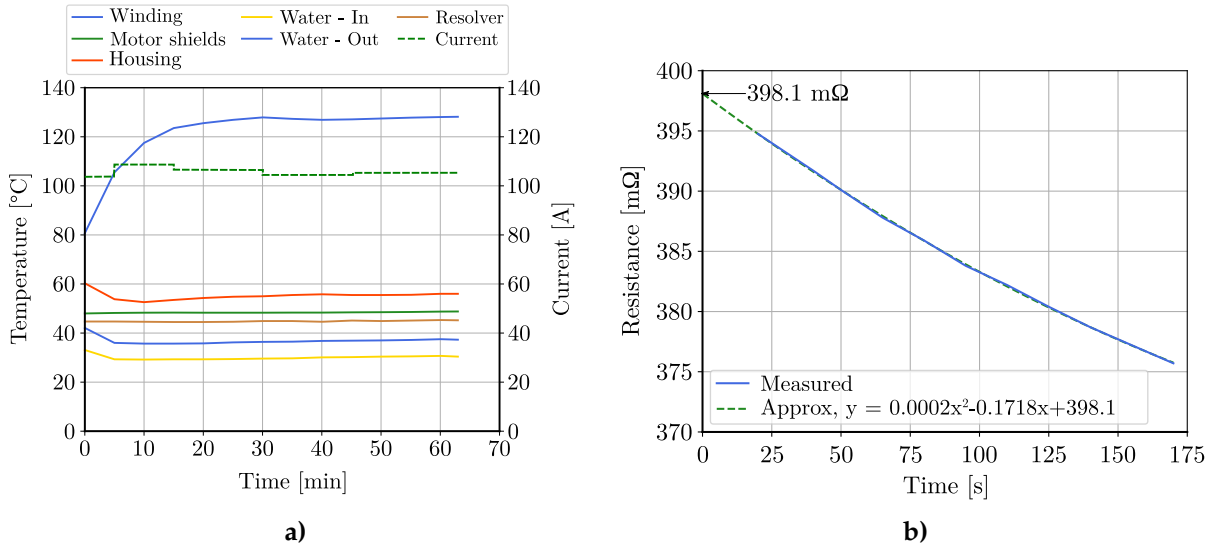

Figure 8.9: a) Temperature and current development during the second MP measurement b) Winding resistance characteristics after the second measurement.

The machine reached an equilibrium in nearly 70 minutes at the slightly higher temperatures compared to the first MP even in the resistance temperature measurement. A current was slightly higher, as expected, and therefore the measured torque has also increased. The initial decrease of the temperatures at the beginning of the measurement was caused by the higher initial temperatures from the first MP measurement. The final measured data comparison with the FEA model are presented in Table 8.5.

The comparison of the measured and FEA characteristics resulted in a similar conclusion to the first measurement. The machine, even though developed a higher shaft torque, was not able to deliver the initial FEA characteristics. But nearly the same results were obtained after modifying the FEA model with the same current. The highest difference occurred in the power factor with the 6.89 % difference. The measured data were higher in nearly all objectives except the efficiency, where the difference was slightly higher (0.24 %) than in the first MP.
All other objectives are in a very close range to the FEA estimated ones. The magnet temperature increased between measurements by 1.5 °C to 82.92 °C. The resistance measurement has shown the temperature 110.7 °C, which is about 17.5 °C less than the PT-1000 result.

Table 8.5: Second MP measurement

Method / Objectives	FEA	Measured	Difference, %	Error, %
Torque, Nm	2396	2420.2	1	0.05
Speed, rpm	100	100	0	0.02
Current, A	105.32	105.32	0	2.89
Current angle, °el	55	53	-	-
Voltage, V	211.1	209.6	0.72	0.243
Input power, kW	32.36	33.56	3.57	0.856
Power factor, -	0.81	0.87	6.89	0.856
Output power, kW	25.1	25.32	1	0.05
Efficiency, %	77.5	75.4	-2.1	0.856
Winding temperature PT-1000, °C	128.2	128.2	0	0.1
Winding temperature from resistance, °C	-	110.7	-	1.08
Magnet temperature from Back-EMF, °C	82.92	82.92	-	0.213
Room temperature, °C	-	27.9	-	0.15

* Note: The magnetic saliency is roughly estimated from AC drive measurement. The measured value is, based on the difference, measured with significant error.

8.6.3 Third measured point

The third MP is defined by the same torque as previous points, 2777 Nm at the 75 rpm speed and was done immediately after the second MP, that causes a similar temperatures behavior to the second measurement. The characteristics from both the load test and the resistance measurement are shown in Figure 8.10 a) and b).

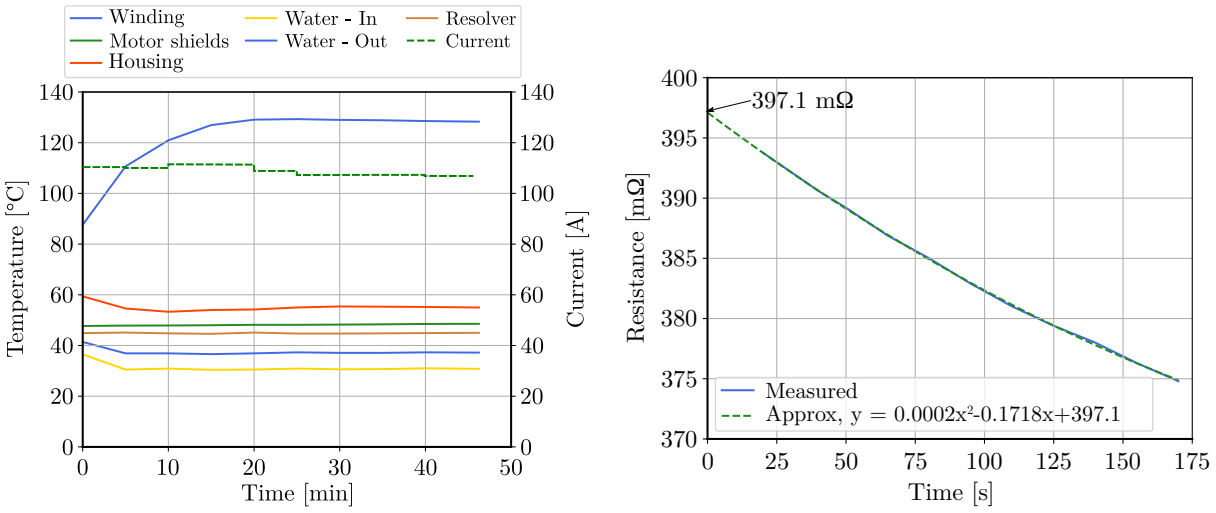

Figure 8.10: a) Temperature and current development during the third MP measurement b) Winding resistance characteristics after the third measurement.

The other temperatures are slightly lower as the same winding temperature is achieved, this can be reasoned by a different losses distribution. In this MP the Joule losses dominate even more over the iron losses, than in the first two MPs, therefore the temperature difference is even higher. The cooling seems to be more sufficient to remove the winding losses than the iron losses, caused by the cooling tubes distribution in the stator core. The data, when the machine

reached the stable state are listed and compared with the FEA in Table 8.6.

Table 8.6: Third MP measurement

Method / Objectives	FEA	Measured	Difference, %	Error, %
Torque, Nm	2447.7	2470.2	0.91	0.05
Speed, rpm	75	75	0	0.02
Current, A	107.9	107.9	0	0. 287
Current angle, °el	55	53	-	-
Voltage, V	169.2	163.4	-3.55	0.279
Input power, kW	26.7	26.97	1	1.03
Power factor, -	0.8	0.82	2.44	1.03
Output power, kW	19.22	19.4	0.93	0.05
Efficiency, %	72	71.9	-0.1	1.03
Winding temperature PT-1000, °C	128.3	128.3	0	0.1
Winding temperature from resistance, °C	-	109.8	-	1.08
Magnet temperature from Back-EMF, °C	85.92	85.92	-	0.213
Room temperature, °C	-	28.4	-	0.15

* Note: The magnetic saliency is roughly estimated from AC drive measurement. The measured value is, based on the difference, measured with significant error.

The third measured data are even closer to the FEA data, while the biggest difference is 3.55 % in the measured voltage, and the lower value is obtained with the manufactured machine. The trend of other objectives is similar to the previous measurement, where the values obtained by the measurement are higher except for the efficiency. The efficiency difference decreased resulting only in 0.1 % in favor of the FEA model.
The temperature deviation between the PT-1000 sensors and the temperature obtained from the winding resistance measurement has slightly increased to 18.5 °C. The magnet temperature has increased as well to 85.92 °C, that is a 3 °C increase from the second MP.

8.6.4 Fourth measured point

The fourth point is the last MP measured with the machine cooling. The testing conditions remained the same when compared to the previously performed measurements. The fourth point is defined by the torque and equals 2777 Nm at the 50 rpm and took place after the third tests checking the PM demagnetization measurement. The data from the temperature and resistance measurements are depicted in Figure 8.11.

Because of the higher stator current and lower iron losses, the temperatures are similar to the previously (in third MP) obtained ones. The temperature difference between the winding and the other parts has very slightly increased, even though the amount of losses in the stator is unchanged (the same cooling conditions and same winding temperature). The resulting data from the load test are listed with the FEA comparison in Table 8.7.

In the fourth measurement are all the measured data above the values achieved by the FEA. The biggest difference, equal to 3.7 %, is found in the $\cos\varphi$ comparison, other objectives are within the 3 % difference range.
The temperature in the PM has also increased since the third measured temperature by nearly 12 °C, due to the higher stator current, that tempered both the machine rotor and the inside space of the machine. The final PM temperature is 97.9 °C.

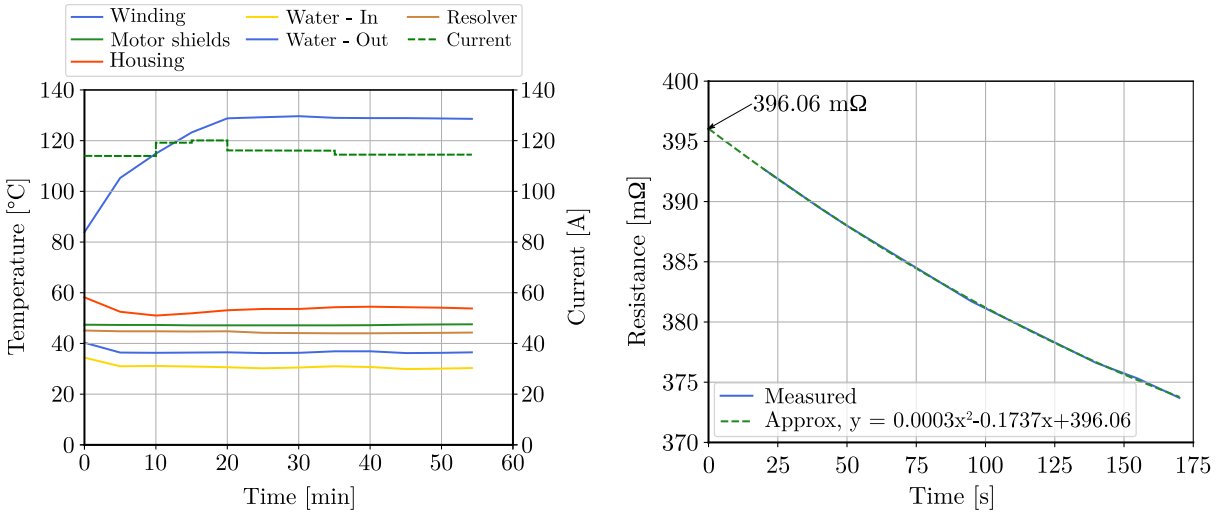

Figure 8.11: a) Temperature and current development during the fourth MP measurement b) Winding resistance characteristics after the fourth measurement.

Table 8.7: Fourth MP measurement

Objectives \ Method	FEA	Measured	Difference, %	Error, %
Torque, Nm	2599.3	2620.7	0.82	0.05
Speed, rpm	50	50	0	0.02
Current, A	115.1	115.1	0	2.88
Current angle, °el	55	54	-	2.88
Voltage, V	129.3	132.9	2.71	0.213
Input power, kW	21.92	21.3	2.91	0.703
Power factor, -	0.78	0.81	3.7	0.703
Output power, kW	13.61	13.7	0.82	0.05
Efficiency, %	62.1	64.7	2.6	0.703
Winding temperature PT-1000, °C	128.6	128.6	0	0.1
Winding temperature from resistance, °C	-	108.9	-	1.08
Magnet temperature from Back-EMF, °C	97.9	97.9	-	0.213
Room temperature, °C	-	29.4	-	0.15

* Note: The magnetic saliency is roughly estimated from AC drive measurement. The measured value is, based on the difference, measured with significant error.

The winding measurement difference between the PT-1000 and the temperature obtained from the resistance has increased to 19.7 °C. The images from the thermal-camera are depicted in Figure 8.12.

The increased winding losses were cooled more sufficiently and thus the hottest spot was found on the left side of the machine and was 63.7 °C.

8.6.5 Fifth measured point

The fifth point is the first, which is measured without water cooling. The motor, based on the Baumüller standards, is expected to deliver half of the cooled motor performance. The fifth point is defined by the 1388.5 Nm at the 150 rpm. But based on the previous tests, it was not

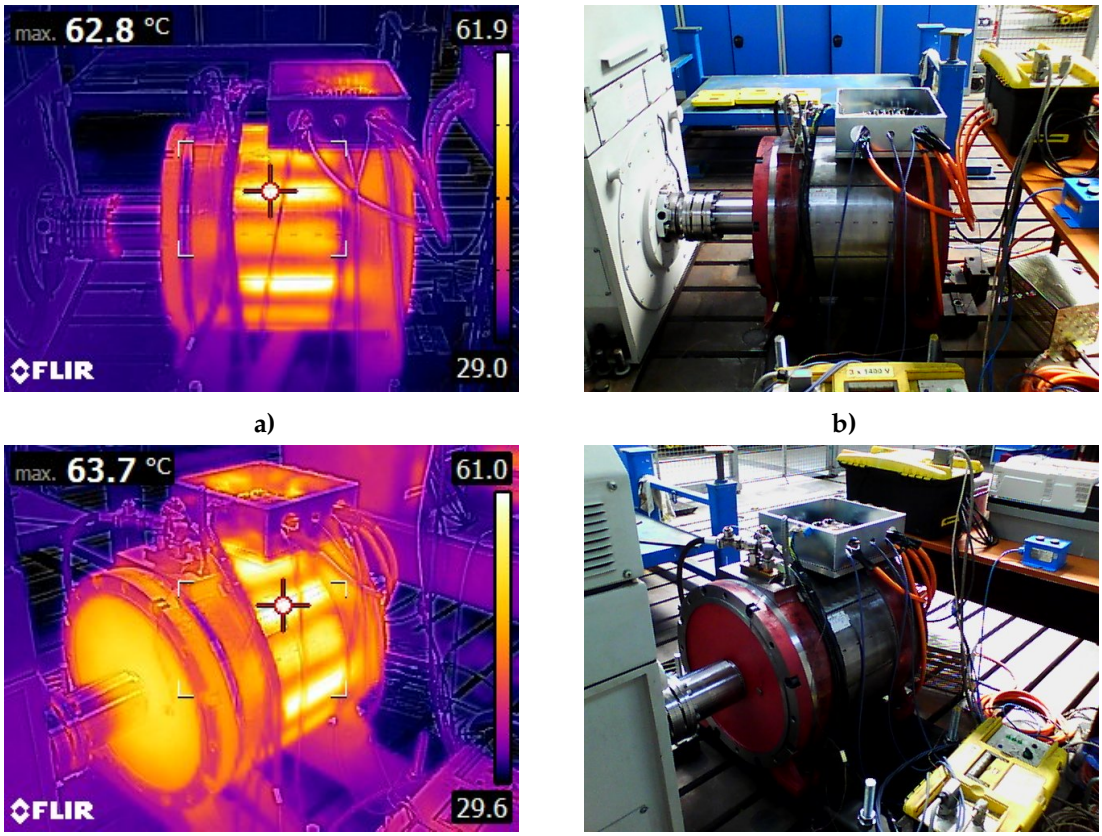

Figure 8.12: Thermal-camera images for the MP at 50 rpm machine with active cooling a) Right side thermal image from the thermal-camera b) Right side real image from the thermal-camera, c) Left side thermal image from the thermal-camera d) Left side real image from the thermal-camera.

expected to achieve the estimated torque. The test was scheduled for the day after the tests with water cooling and after the successful demagnetization checking test. The temperatures and winding resistance characteristics are shown in Figure 8.13 a) and b).

Both the temperature and the resistance test express certain "inconsistencies". These seldom occurrences are caused by the coolant being still present inside the tubing system. Thus for the protection of the motor, the hot coolant was removed, when it reached the temperature close to the boiling point. The potential boiling coolant can damage the motor water tubing.
Two distinctions can be pointed out just from a brief look at the figures compared to the previous points. The first one being the relatively high housing temperature, that even in the worst case in the cooled machine is lower than 60 °C now becomes become nearly 100 °C, thus the coolant protective removing procedure. The second difference can be seen in the winding resistance figure, where the values are much higher (circa by 10 mΩ). Thus the temperature differences between PT-1000 sensors and winding resistance are smaller. The final data are compared with the FEA calculations in Table 8.8.

The fifth MP data listed in the Table 8.8 show the biggest differences equal to nearly 8 % in the terminal voltage and 7.25 % in the measured shaft torque, this error is then carried into the output power difference. Other measured and estimated values do not overcome the 3.1 % difference. The FEA model appears to be relatively accurate even for this kind of machine without the cooling at higher PM temperatures. The measuring machine and the FEA model

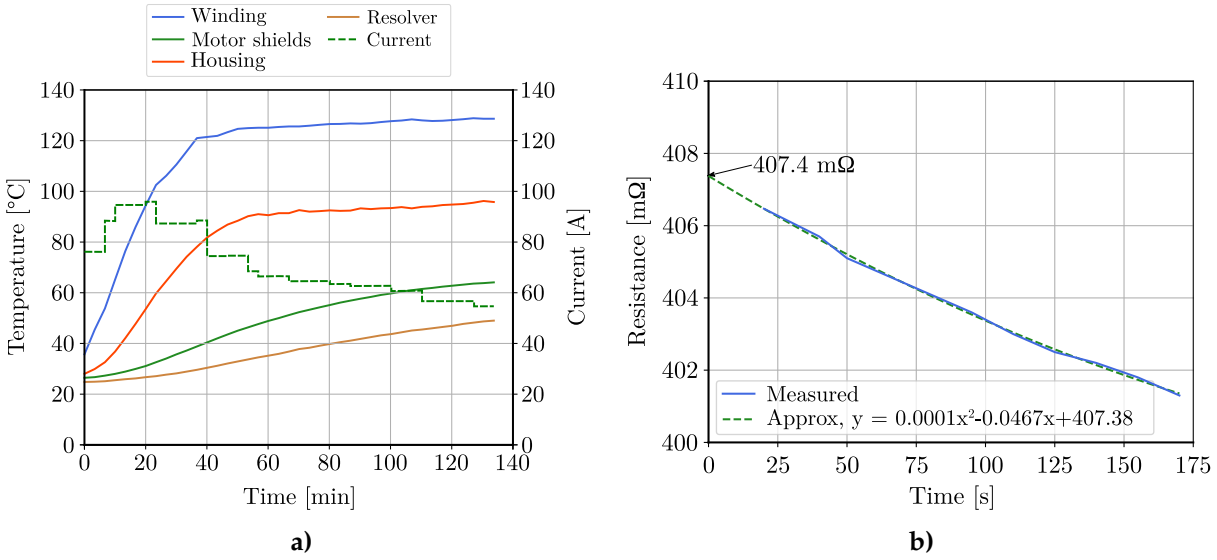

Figure 8.13: a) Temperature and the current development during the fifth MP measurement b) Winding resistance characteristics after the fifth measurement.

Table 8.8: Fifth MP measurement

Objectives \ Method	FEA	Measured	Difference, %	Error, %
Torque, Nm	1179.9	1100.1	-7.25	0.07
Speed, rpm	150	150	0	0.02
Current, A	52.76	52.76	0	2.92
Current angle, °el	50	51	-	2.92
Voltage, V	250.4	231.9	-7.98	0.23
Input power, kW	20.72	20.1	-3.08	0.755
Power factor, -	0.9	0.92	2.17	0.755
Output power, kW	18.53	17.28	-7.25	0.07
Efficiency (First harmonics), %	89.46	89.1	-0.36	0.755
Winding temperature PT-1000, °C	128.6	128.6	-	0.1
Winding temperature from resistance, °C	-	118.8	-	1.08
Magnet temperature from Back-EMF, °C	109.89	109.89	-	0.213
Room temperature, °C	-	25.5	-	0.15

* Note: The magnetic saliency is roughly estimated from AC drive measurement. The measured value is, based on the difference, measured with significant error.

achieves the maximum torque by given stator current at a different current angle with the difference being 1 °.

The motor is not sufficiently cooled without the water cooling and is not capable of providing the 50 % of the rated torque (power), which should be equal to - $\frac{2365.5\text{ Nm}}{2}$ = 1182.8 Nm and is around 7 % lower. The magnet temperature, for the first time, exceeded 100 °C and stabilized at approximately 109.89 °C. This temperature is still much lower than the listed Curie temperature of the PZK454 material (460 °C from [70]). This magnet temperature increase is due to the insufficient heat removal from the stator, which is then kept in the machine. The heat removal could be improved by the black color coating of the machine, which is usually done in most cases of manufacturing. The color coating was not done due to the prototype manufacturing cost reduction.

The stator housing is reaching dangerous temperatures to the touch. In Figure 8.14 are the

thermo-camera images shown for the both machine sides.

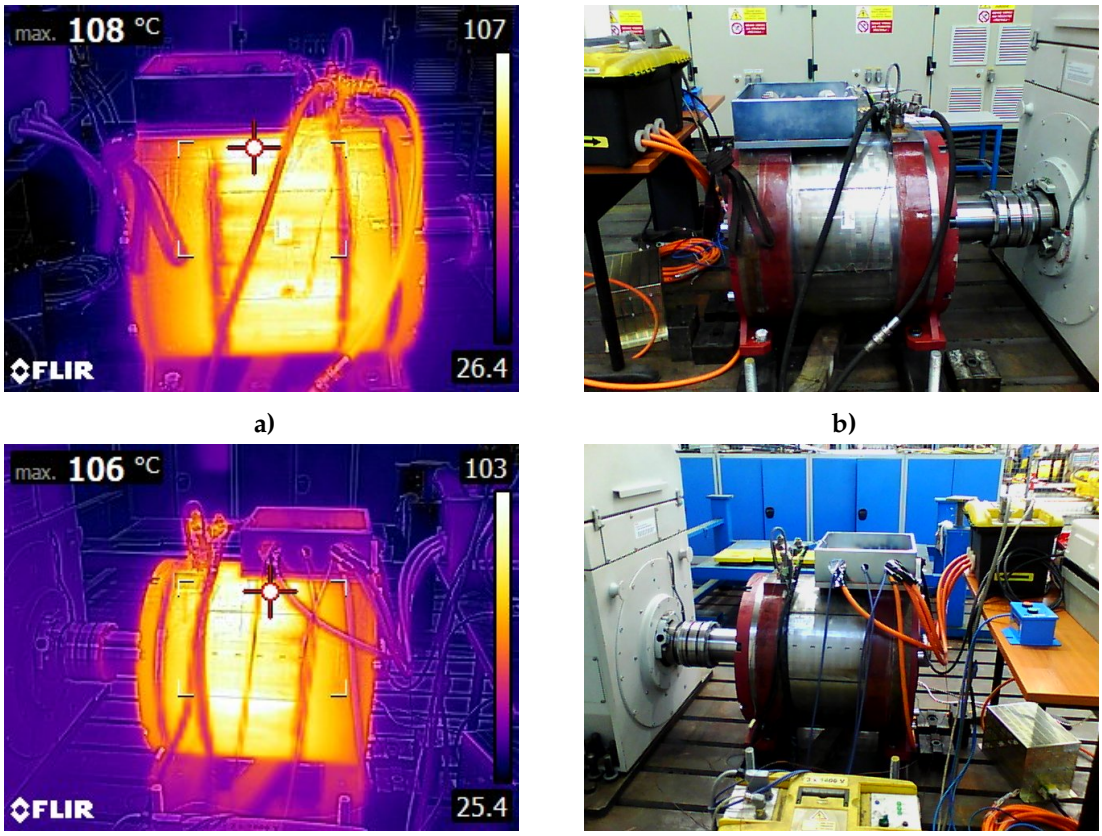

Figure 8.14: Thermal-camera images for MP 150 rpm machine without active cooling a) Right side thermal image from the thermal-camera b) Right side real image from the thermal-camera, c) Left side thermal image from the thermal-camera d) Left side real image from the thermal-camera.

The camera aimed at the hottest spot of the motor housing, which was 108 °C on the right side, 106 °C on the left side respectively.

8.6.6 Sixth measured point

The last MP and the second point that is measured without cooling and is characterized by the 1388.5 Nm at the 150 rpm. This test was scheduled after the fifth MP, thus the initial higher temperatures in the motor parts. The temperature and resistance characteristics are depicted in Figure 8.15.

Both characteristics express a similar behavior to the fifth MP and achieve very similar results. The "inconsistencies" present in the last MP, though less visible, are still present. The machine becomes reasonably stable after the one hour of measurement and therefore the measurement was ended, also due to the already tempered machine from the previous measurement. The machine measured performance characteristics are compared with the FEA data in Table 8.9.

In the last measurement the biggest difference, similarly to the fifth MP, was found in the measured torque, due to the fixed speed, in the output power. The difference was estimated as

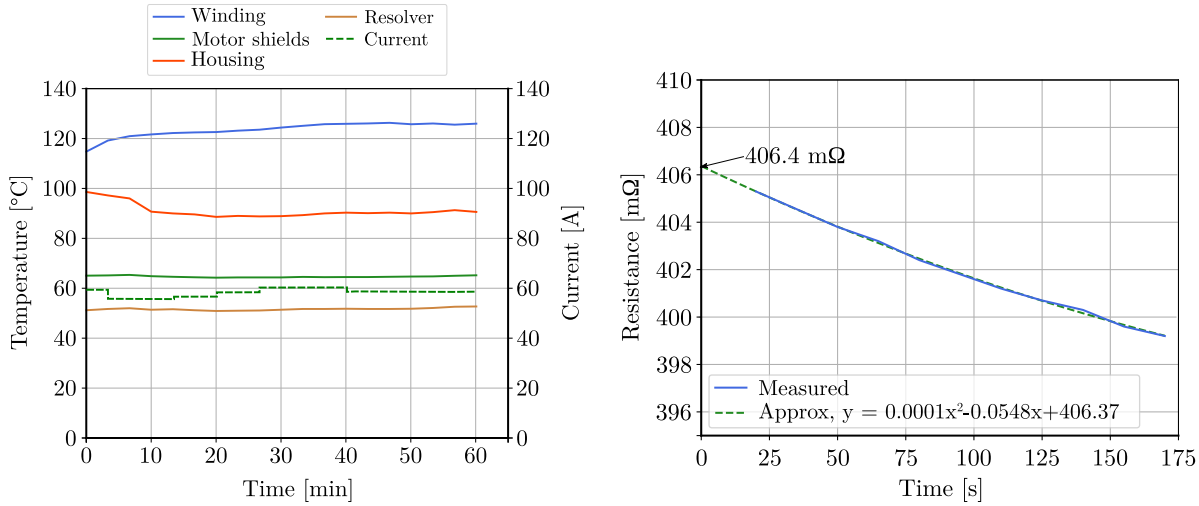

Figure 8.15: a) Temperature and current development during the sixth MP measurement b) Winding resistance measurement characteristics after the sixth measurement

Table 8.9: Sixth MP measurement

Objectives \ Method	FEA	Measured	Difference, %	Error, %
Torque, Nm	1359.8	1300.4	-4.57	0.07 %
Speed, rpm	50	50	0	0.02 %
Current, A	58.65	58.65	0	0.273 %
Current angle, °el	50	48	-	0.273 %
Voltage, V	100.2	101.7	1.47	0.247 %
Input power, kW	9.388	9.31	-0.84	0.794 %
Power factor, -	0.91	0.9	-1.11	0.794 %
Output power, W	7.12	6.8	-4.57	0.07 %
Efficiency (First harmonics), %	75.8	73.1	-2.7	0.794 %
Winding temperature PT-1000, °C	127.6	127.6	0	0.1 %
Winding temperature from resistance, °C	-	117.9	-	1.08 %
Magnet temperature from Back-EMF, °C	117.75	117.75	-	0.213
Room temperature, °C	-	26.8	-	0.15 %

* Note: The magnetic saliency is roughly estimated from AC drive measurement. The measured value is, based on the difference, measured with significant error.

4.57 %, while other differences are within the 3 % range.
The magnet temperature has increased in the sixth MP to 117.75 °C, while the room temperature difference between the fifth MP and sixth MP has increased as well to 26.8 °C.
The motor performance increased to nearly the half of the torque delivered at the same speed with the active cooling. The required torque was $\frac{2620.7\text{ Nm}}{2} = 1310.35$ Nm and is by 0.76 % lower.
The thermal images of the machine at the stable state were taken and are shown in Figure 8.16.

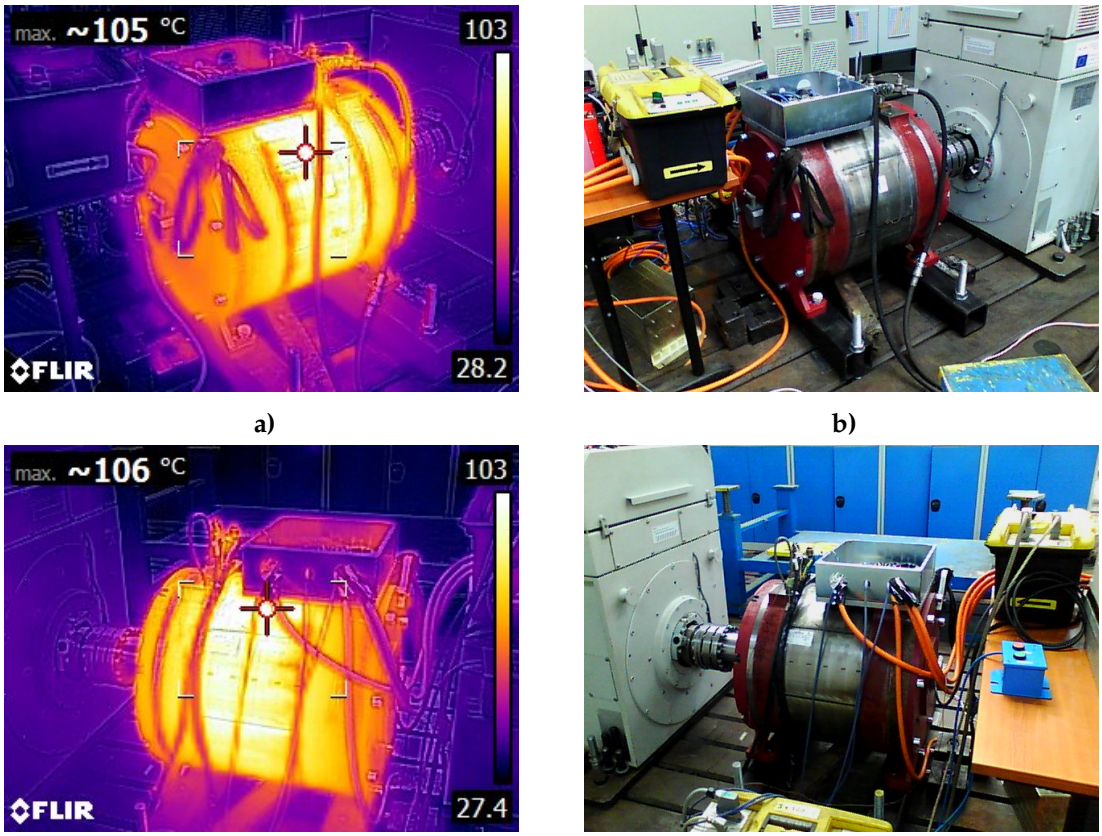

Figure 8.16: Thermal-camera images for the MP at 50 rpm machine without active cooling a) Right side thermal image from the thermal-camera b) Right side real image from the thermal-camera, c) Left side thermal image from the thermal-camera d) Left side real image from the thermal-camera.

9 | Conclusion

This chapter is about to conclude the dissertation thesis and to briefly sum up the accomplished work.

This dissertation thesis introduced the procedure of the design and optimization of the high-torque low-speed permanent magnet-assisted synchronous reluctance motor for the ship propulsion. The desired machine was aimed to achieve the output power of 55 kW at 150 rpm. The work was mainly focused on the design aspects and the aim of a low-cost solution for the mentioned application.
In the beginning of the second chapter, some of the electric motor design challenges were introduced to the reader, purely to underline the importance and the state of the art of the thesis. The proposed topic was, along with the relevant publication research, presented as actual and promising to the future.
The third chapter introduced some basic principles and a broader overview of the permanent magnets used in the field of the electrical machines. This chapter aimed to help the reader to gain an overview of the permanent magnets used for the design, ferrites, in the context of the historical and energy density. Important aspects of all the ferrites used in the electromagnetic design with some brief chemical points of view were depicted as well. At the end of the chapter, a research of the relevant ferrite magnets manufacturers including the stored energy, remanent flux densities, and materials was done. The highest energy densities were found in the TDK manufacturer datasheets, followed closely by the Hitachi manufacturer the first one reaching 44 kJ/m^3 and the second one 43 kJ/m^3 and the remanent flux density equal to 0.475 T, 0.485 T respectively.
The next chapter dealt with a synchronous reluctance motor theory along with the applications and the motor stronger and weaker characteristics and the state of art analysis. The ferrite-assisted machines are found in many applications, some of them aiming at low-speed propulsions.
The title of the richest chapter, solely by the number of pages, could be assigned to the fifth chapter, which dealt with the optimization algorithms. After a brief interview of the optimization with the historical contents, the sorting and commonly used functions with the emphasis put on the description of the most commonly used members in each algorithms branch. This presented the broad topic of optimization to the reader and gave an overview of the used algorithms in electric machines with the pros and cons. The chapter contained a detailed description of the algorithms used by the author, the self-organizing migrating algorithm and genetic algorithms, with the principles and the parameters.
The sixth chapter presented the practical part of the thesis. The design part introduction stated the desired characteristics, the proposed geometry, and the materials chosen for the machine design. As the chapter evolved the ideal slot-poles combination was investigated. The part of the electromagnetic design, that seemed to be overlooked seems to be the comparison with the

other flux-barrier shapes and counts in the designs. This was due to both the limited time for the design and the requirement to achieve the low-cost machine solution. The author's experience with this flux-barrier count lead to the geometry which uses these three barrier topology and seems to be a reasonable solution based on the achieved results. The investigation of the best combination was done in the commonly used winding types - the integral slot winding, the fractional-slot distributed winding, and both the single and dual-layer fractional-slot concentrated windings. The best combinations found in the research, which were then chosen for further analysis, were the 60 slots 10 poles integral slot winding, the 54 slots 12 poles, and the 45 slots 10 poles fractional-slot distributed winding, and the 18 slots 16 poles fractional-slot concentrated single-layer winding. While the best characteristics were found in the combinations with the lower pole number.
The previous chapter was naturally followed by the one dealing with optimization. The purpose is threefold, one is stating the comparison of the ideal versus the preference based multi-objective optimization. This comparison resulted clearly in a favor of the ideal multi-objective algorithms, where only the multi-objective self-organizing migrating algorithm and the non-dominant sorting genetic algorithm were able to find an optimal solution satisfying the desired machine objectives. As the winners of comparison regarding the principle can be seen the genetic algorithms in both modifications. As a clear "no-go" option of the comparison is the self-organizing migrating algorithm probably because of the higher amount of the optimized parameters because this algorithm was able to deliver solid results in other scenarios, as stated in the chapter dealing with the optimization algorithms.
The second chapter's outcome can be seen in the optimization of the geometries chosen in the sixth chapter. These combinations were optimized by the non-dominant sorting genetic algorithm based on the solid results obtained in the first optimization scenario. All four geometries were optimized and delivered solid results, again with the lower-poles combinations dominating over the 16 pole geometry. The rest of the optimized combinations achieved very promising results and all three machines could be built, with some modifications regarding the manufacturing tolerances and mounting holes.
The third goal was to optimize the restricted optimization case of the best and suitable geometry for the application - the 60 slots and 10 poles combination. With the optimization restrictions, it was not possible to find the optimal solutions satisfying the desired objectives with both ideal multi-objective optimization algorithms.
The optimized motor was then deeply analyzed by finite element analysis both in the various speeds and the working points delivering solid results in all depicted objectives.
The final chapter dealt with the testing procedure of the optimized machine. This was performed on the shorter stack length machine than considered in the design process to lower the prototype cost. This chapter introduced the problematic setup of the AC drive and the solutions, test bench, and the testing results with the measurement uncertainties. The designed machine was not able to deliver the characteristics estimated by the finite element analysis. This was mainly due to the non-sufficient cooling of the machine and worse conditions in the testing.

Regardless of failing to deliver the desired test results is the work done in this thesis is considered to be of good value for both researchers and engineers dealing with the ferrite-assisted synchronous reluctance machines for the high-torque and low-speed applications. This thesis proved the claim stated in the chapter 4, that the ferrite assisted reluctance machine is able to deliver about 30 % lower power than the SPM with the same stack length.

9.1 Future work

The development of the high-torque synchronous reluctance motor and the measurement served as an initial step toward the further development that will take place after the dissertation thesis.
The final machine design comes from the currently produced stator by the manufacturer including the water-cooling, which had become the weakest part of the design. Regarding this, the second obvious step would be either to choose the machine designs in the section 7.3 or to use a more efficient cooling.
The other part of the future development could be the test of the different higher energy magnets from other manufacturers to deliver a higher power factor, torque per volume ratio and thus decrease the current loading and Joule losses.
What could be seen as promising for future development is to apply this 30 % power decrease when compared to the SPM that could be taken into account in the second electromagnetic design.
The conclusions drawn in the chapter 8 seems to be very useful regarding the power electronics setup that could be developed for similar ferrite assisted synchronous reluctance machines and lower the risk of demagnetization within the drive setup. A new dq-axes identification procedure needs to be developed for the serial AC drive configuration in order to simplify the setup procedure.

10 Attachments

10.1 The dynamometer ASD P500 datasheet

TYP DYNAMOMETRU řady ASD P			ASD 15K-4 ASD P015-4/0096		ASD 30K-2 ASD P030-2/0036		ASD 46K-4 ASD P046-4/0220		ASD 50K-4 ASD P050-4/0312		ASD 85K-4 ASD P085-4/0541		ASD 100K-4 ASD P100-4/0637		ASD 153K-4 ASD P153-4/0947	
HODNOTY DYNAMOMETRU			**Brzda**	**Motor**	**Brzda**	**Motor**	**Brzda**	**Motor**	**Brzda**	**Motor**	**Brzda**	**Motor**	**Brzda**	**Motor**	**Brzda**	**Motor**
Jmenovitý výkon	P_n	kW	15	13	30	30	46	42	50	45	85	77	100	100	153	145
Výkon v n_{max}	P_{nmax}	kW	6	5,2	30	30	26	20	25	23	40	32	55	52	105	100
Jmenovitý moment	M_{n1}	Nm	93	80,6	35,8	35,8	220	200	312	281	541	490	637	637	974	923
Moment v n_2	M_{n2}	Nm	47,8	56,4	28,7	28,7	108,7	160,4	159	179	225	283	265	281	487	462
Moment v n_{max}	M_{nmax}	Nm	9,5	8,3	28,7	28,7	41,3	31,8	40,0	36,6	64,0	51,0	88	83	201	191
Maximální moment	M_{max}	Nm	150		50		200		450		800		1 000		1 300	
Kalibrační moment	M_{kal}	Nm	100		40		200		300		700		900		1 000	
Jmenovité otáčky	n_1	min^{-1}	1 540	1 540	8 000	8 000	2 000	2 000	1 530	1 530	1 500	1 500	1 500	1 500	1 500	1 500
Otáčky	n_2	min^{-1}	3 000	2 200	10 000	10 000	4 050	2 500	3 000	2 400	3 600	2 600	3 600	3 400	3 000	3 000
Maximální otáčky	n_{max}	min^{-1}	6 000		10 000		6 000		6 000		6 000		6 000		5 000	
Minimální provozní otáčky	n_{min}	min^{-1}	50		50		50		50		50		50		50	
Proud naprázdno	I_0	A	11,6		17,1		25,4		32,9		69,0		76,0		130,0	
Jmenovitý proud	I_{n1}	A	27,1		52,4		82,4		87,1		167,0		180,0		268,4	
Jmenovité napětí	U_{n1}	V	360	360	390	390	345	360	360	360	400	400	400	400	400	400
Napětí v n_2	U_{n2}	V	360	360	390	390	360	360	360	360	400	400	400	400	400	400
Jmenovitá frekvence	f_{n1}	Hz	50	53	132	135	65	68	50	52	49	51	49	51	49	51
Frekvence v n_2	f_{n2}	Hz	100	76	164	169	132	85	98	82	117	89	118	116	98	102
Frekvence v n_{max}	f_{nmax}	Hz	195	203	164	169	198	202	198	202	197	203	198	202	164	169
cos fi		-	0,79		0,88		0,87		0,86		0,78		0,81		0,78	
TECHNICKÁ DATA																
Kalibrační rameno	L_C	m	0,5099		1,0194		1,0194		1,0194		1,0194		1,0194		1,0194	
Kalibrační hmotnost	m_{KAL}	kg	20		4		20		30		70		90		100	
Snímače teploty - vinutí			KTY84		PTC		KTY84		KTY84		KTY84		KTY84		KTY84	
- AS ložisko			Pt100		Pt100		Pt100		Pt100		Pt100		Pt100		Pt100	
- BS ložisko			Pt100		Pt100		Pt100		Pt100		Pt100		Pt100		Pt100	
Moment setrvačnosti	J	kgm^2	0,0766		0,053		0,2626		0,4289		0,445		0,925		0,925	
Barva dynamometru			RAL7035		RAL7035		RAL7035		RAL7035		RAL7035		RAL7035		RAL7035	
Hmotnost	m	kg	235		520		285		450		733		1 220		1 225	
Snímač otáček - typ			ROD426		ERO1420		ROD426		ROD426		ROD426		ROD426		ROD426	
- počet pulzů			1 024		1 024		1 024		1 024		1 024		1 024		1 024	
Snímač síly - typ			SM250		Z6FC3/50		SM250		SM500		Z6FC3 5kN		Z6GC3		Z6GC3	
- jmenovitá síla	F_N	N	1 112		460		1 112		2 224		5 000		5 000		5 000	
Spojka - typ			Rotex, Modulflex		Modulflex		Rotex, Modulflex		Rotex, Modulflex		Modulflex		Modulflex		Modulflex	
MECHANICKÉ ROZMĚRY - mm																
A			312		430		INFO VERTIKÁLNÍ PROVEDENÍ		420		600		700		700	
B			320		406				440		406		510		510	
C			403		588				514		750		852		852	
D			708		715				806		977		1 033		1 033	
E			480		490				506		520		630		630	
F			200		225				250		250		315		315	
G			660		855				766		880		1 000		1 000	
H			38H6		35H6				48H6		45H6		60H6		60H6	
I			80		50				110		50		52		52	
K			1 270		2 400				2 150		2 400		2 570		2 570	

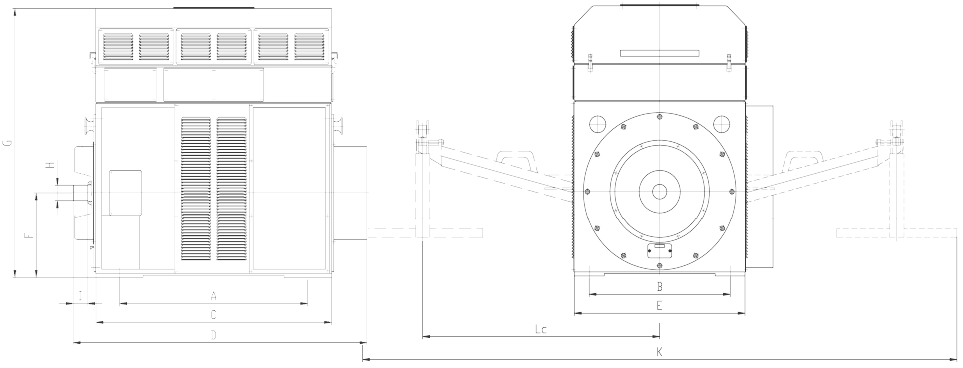

Změna technických údajů vyhrazena.

09-004-0 2/8 REV. 12-08-10

VUES Brno s.r.o. Mostecká 992/26, 657 65 BRNO, Česká republika, tel.: 545 551 111 fax: 545 551 222 e-mail: mail@vues.cz http://www.vues.cz

ASD 200K-4 ASD P200-4/1275		ASD 220K-4 ASD P220-4/0934		ASD 220K-8 ASD P220-8/1868		ASD 330K-8 ASD P330-8/2801		ASD 400K-4 ASD P400-4/1863		ASD 440K-8 ASD P440-8/3735		ASD 500K-4 ASD P500-4/3183		ASD 660K-4 ASD P660-4/4400		ASD 800K-4 ASD P800-4/5496	
Brzda	**Motor**	**Brzda**	**Motor**	**Brzda**	**Motor**	**Brzda**	**Motor**	**Brzda**	**Motor**	**Brzda**	**Motor**	**Brzda**	**Motor**	**Brzda**	**Motor**	**Brzda**	**Motor**
200	190	220	210	220	205	330	315	400	380	440	420	500	500	660	625	800	765
110	105	150	143	120	105	185	170	350	315	260	250	320	320	660	625	800	765
1 275	1 210	934	891	1 868	1 740	2 801	2 674	1 863	1 770	3 735	3 565	3 183	3 183	4 400	4 171	5 496	5 256
529	504	467	501	1 051	1 058	1 576	1 583	849	907	2 101	2 111	1 326	1 326	1 575	1 492	1 910	1 825
175	167	239	228	287	250	505	464	557	501	709	682	509	509	1 575	1 492	1 910	1 825
1 800		1 400		2500		4 000		2500		5 000		4 500		6 000		7 000	
1 500		1 000		2300		3 500		2000		4 500		3500		5000		6 000	
1 500	1 500	2 250	2 250	1 125	1 125	1 125	1 125	2 050	2 050	1 125	1 125	1 500	1 500	1 430	1 430	1 390	1 390
3 600	3 600	4 500	4 000	2 000	1 850	2 000	1 900	4 500	4 000	2 000	1 900	3 600	3 600	4 000	4 000	4 000	4 000
6 000		6 000		4 000		3 500		6 000		3 500		6 000		4 000		4 000	
50		50		5		5		50		5		50		10		10	
153		135		201		281		304		340		378		326		415	
369		380		408		606		684		775		881		756		980	
370	370	380	380	387	400	390	400	400	400	400	400	400	400	585	585	540	540
400	400	380	380	400	400	400	400	400	400	400	400	400	400	660	660	600	600
49	51	74	76	74	76	74	76	68	69	74	76	50	51	47	48	46	47
118	122	148	135	131	125	132	129	148	135	132	128	119	121	132	135	132	134
198	202	198	202	264	269	232	235	198	202	232	235	199	202	132	135	132	134
0,82		0,86		0,76		0,77		0,81		0,79		0,82		0,83		0,85	

1,0194	1,0194	1,0194	1,0194	1,0194	1,0194	1,0194	1,0194	1,0194
150	100	230	350	200	450	350	500	600
KTY84	KTY84	KTY84	KTY84	KTY84	KTY84	KTY84	KTY84	KTY84
Pt100	Pt100	Pt100	Pt100	Pt100	Pt100	Pt100	Pt100	Pt100
Pt100	Pt100	Pt100	Pt100	Pt100	Pt100	Pt100	Pt100	Pt100
1,9	1,8	3,46	6,75	2,441	11,1	7,66	6,56	16,82
RAL7035	RAL7035	RAL7035	RAL7035	RAL7035	RAL7035	RAL7035	RAL7035	RAL7035
1 820	1 180	1 905	2 460	2 080	2 715	2 715	3 140	4 100
ROD426	ROD426	ROD426	ROD426	ROD426	ROD426	ROD426	ROD426	ROD426
2 048	1 024	4 096	4 096	1 024	4 096	1 024	1 024	1 024
Z6GC3	Z6GC3	Z6FC3/10	3410/2000/C3	Z6GC3	3410/2000/C3	3410C3	3420-G	3420-G
5 000	5 000	10 000	20 000	10 000	20 000	20 000	44 483	44 483
Modulflex	Modulflex	Modulflex	Modulflex	Modulflex	Modulflex	Modulflex	Modulflex	Modulflex

790	700	790	850	890	950	1 100	1 100	1 230
610	510	610	686	610	686	686	686	750
992	852	992	1 052	1 092	1 152	1 302	1 320	1 460
1 234	1 060	1 234	1 301	1 336	1 401	1 551	1 551	1 760
740	630	740	820	740	820	820	820	880
355	315	355	400	355	400	400	400	450
1 130	1 005	1 130	1 220	1 130	1 220	1 220	1 220	1 350
65H6	60H6	65H6	85H6	65H6	85H6	85H6	85H6	95H6
60	52	60	70	60	70	70	70	85
2 570	2 570	2 570	2 700	2 570	2 700	2 700	2 700	2 900

Příslušenství pohonu s dynamometrem

Řídicí jednotka s měřením M350

Napájecí měniče SIEMENS

Napájecí měniče Controltechniques

VUES Brno s.r.o. Mostecká 992/26, 657 65 BRNO, Česká republika, tel.: 545 551 111 fax: 545 551 222 e-mail: mail@vues.cz http://www.vues.cz

Bibliography

[1] J. Pecho and W. Hofmann. Analysis of start-up of line-start permanent magnet synchronous machines with anisotropic rotor reluctance. In *2018 XIII International Conference on Electrical Machines (ICEM)*, pages 72–78, 2018.

[2] D. Mingardi, N. Bianchi, and L. Alberti. Optimal choice of stack length and conductors of line start synchronous motors. In *8th IET International Conference on Power Electronics, Machines and Drives (PEMD 2016)*, pages 1–6, 2016.

[3] J. Montonen, S. Sinkko, P. Lindh, and J. Pyrhönen. Design of a traction motor with two-step gearbox for high-torque applications. In *2014 International Conference on Electrical Machines (ICEM)*, pages 1069–1075, September 2014.

[4] J. Barta, N. Uzhegov, P. Losak, C. Ondrusek, M. Mach, and J. Pyrhonen. Squirrel cage rotor design and manufacturing for high-speed applications. *IEEE Transactions on Industrial Electronics*, pages 1–1, 2018.

[5] O. Ocak, M. Onsal, and M. Aydin. Development of a 7.5kw high speed interior permanent magnet synchronous spindle motor for CNC milling machine. In *2018 XIII International Conference on Electrical Machines (ICEM)*, pages 704–709, September 2018.

[6] K. Kawanishi, K. Matsuo, T. Mizuno, K. Yamada, T. Okitsu, and K. Matsuse. Development and performance of high-speed SPM synchronous machine. In *2018 International Power Electronics Conference (IPEC-Niigata 2018 -ECCE Asia)*, pages 169–176, May 2018.

[7] C. Babetto, G. Bacco, and N. Bianchi. Synchronous reluctance machine optimization for high-speed applications. *IEEE Transactions on Energy Conversion*, 33(3):1266–1273, September 2018.

[8] W. Zhu, X. Yang, and Z. Lan. Structure optimization design of high-speed BLDC motor using taguchi method. In *2010 International Conference on Electrical and Control Engineering*, pages 4247–4249, June 2010.

[9] A. Castagnini, P. S. Termini, G. Secondo, and N. Bianchi. Replacing SPM by PMAREL machines in low-speed high-torque applications. In *2016 IEEE Energy Conversion Congress and Exposition (ECCE)*, pages 1–8, September 2016.

[10] F. A. Himmelstoss and O. Amtmann. DC motor drive with high torque at low speeds. In *2011 IEEE EUROCON - International Conference on Computer as a Tool*, pages 1–4, April 2011.

[11] S. Sayeef, G. Foo, and M. F. Rahman. Svm direct torque control of IPM synchronous machines at very low speeds. In *2008 4th IET Conference on Power Electronics, Machines and Drives*, pages 296–300, April 2008.

[12] M. Ahmad, M. R. Khan, and A. Iqbal. A doubly fed induction motor as high torque low speed drive. In *2006 International Conference on Power Electronic, Drives and Energy Systems*, pages 1–3, December 2006.

[13] Siemens - complete torque motors.

[14] M. Novák, J. Novák, Z. Cerovský, and J. Chyský. Dynamic properties of high-speed electrical motor supercharger. In *2011 IEEE International Conference on Industrial Technology*, pages 153–158, 2011.

[15] T. Noguchi, Y. Takata, Y. Yamashita, and S. Ibaraki. 160,000-r/min, 2.7-kw electric drive of supercharger for automobiles. In *2005 International Conference on Power Electronics and Drives Systems*, volume 2, pages 1380–1385, November 2005.

[16] J. S. Thongam, M. Tarbouchi, A. F. Okou, D. Bouchard, and R. Beguenane. Trends in naval ship propulsion drive motor technology. In *2013 IEEE Electrical Power Energy Conference*, pages 1–5, August 2013.

[17] Jiyoung Lee, Jongmoo Kim, and Byungchul Woo. Optimal design of in-wheel motor for an e-bike. In *2016 IEEE Transportation Electrification Conference and Expo, Asia-Pacific (ITEC Asia-Pacific)*, pages 441–443, June 2016.

[18] Pyrhonen Juha, Tapani Jokinen, and Hrabovcova Valeria. *Design of rotating electrical machines*. Wiley, 2014.

[19] C. Cho, J. Ahn, and D. Lee. Self-excitation system using high-efficiency low-power PM generator. In *2018 IEEE 18th International Power Electronics and Motion Control Conference (PEMC)*, pages 428–433, August 2018.

[20] W. L. Soong, S. Kahourzade, C. Liaw, and P. Lillington. Interior PM generator for portable AC generator sets. *IEEE Transactions on Industry Applications*, 52(2):1340–1349, March 2016.

[21] N. Baloch and B. Kwon. A distributed winding wound field pole-changing vernier machine for variable speed application. *IEEE Transactions on Magnetics*, pages 1–6, 2019.

[22] M. Choi and B. Kim. Calculation of PM vernier motors using an improved air-gap permeance function. *IEEE Transactions on Magnetics*, pages 1–5, 2019.

[23] M. Meribout and S. Sonowan. Optimal halbach magnet array design for portable NMR targeting multiphase flow metering applications. *IEEE Transactions on Magnetics*, 55(1):1–7, January 2019.

[24] L. Jing, T. Zhang, Y. Gao, R. Qu, Y. Huang, and T. Ben. A novel HTS modulated coaxial magnetic gear with eccentric structure and halbach arrays. *IEEE Transactions on Applied Superconductivity*, 29(5):1–5, August 2019.

[25] A. Kersten, Y. Liu, D. Pehrman, and T. Thiringer. Rotor design of line-start synchronous reluctance machine with round bars. *IEEE Transactions on Industry Applications*, 55(4):3685–3696, July 2019.

[26] Y. Hu, B. Chen, Y. Xiao, J. Shi, L. Li, and X. Li. Rotor design and optimization of the three-phase line-start synchronous reluctance motor. In *2019 22nd International Conference on Electrical Machines and Systems (ICEMS)*, pages 1–6, August 2019.

[27] Viviana Fernandez. Rare-earth elements market: A historical and financial perspective. *Resources Policy*, 53:26–45, September 2017.

[28] F. Wu and A. M. EL-Refaie. Permanent magnet vernier machines: A review. In *2018 XIII International Conference on Electrical Machines (ICEM)*, pages 372–378, September 2018.

[29] A. Nematsaberi and J. Faiz. A novel linear stator-PM vernier machine with spoke-type magnets. *IEEE Transactions on Magnetics*, 54(11):1–5, November 2018.

[30] C. Shi, R. Qu, Y. Gao, D. Li, L. Jing, and Y. Zhou. Design and analysis of an interior permanent magnet linear vernier machine. *IEEE Transactions on Magnetics*, 54(11):1–5, November 2018.

[31] M. Chen, G. H. Liu, W. X. Zhao, Q. Chen, W. X. Zhao, and Y. Zeng. Cost reduction of vernier permanent-magnet machine with ferrite magnets. In *2015 IEEE International Conference on Applied Superconductivity and Electromagnetic Devices (ASEMD)*, pages 94–95, November 2015.

[32] K. Sato, R. Hosoya, and S. Shimomura. Improved ferrite magnet vernier machine for an in-wheel machine. In *2012 IEEE International Conference on Power and Energy (PECon)*, pages 414–419, December 2012.

[33] W. Liu and T. A. Lipo. Alternating flux barrier design of vernier ferrite magnet machine having high torque density. In *2017 IEEE Electric Ship Technologies Symposium (ESTS)*, pages 445–450, August 2017.

[34] C. Heister and M. Henke. Topology comparison of ferrite magnet synchronous machines with consideration of low inertia. In *2016 Eleventh International Conference on Ecological Vehicles and Renewable Energies (EVER)*, pages 1–7, April 2016.

[35] Z. S. Du and T. A. Lipo. Design of an improved dual-stator ferrite magnet vernier machine to replace an industrial rare-earth ipm machine. *IEEE Transactions on Energy Conversion*, 34(4):2062–2069, December 2019.

[36] G. Bacco, N. Bianchi, and F. Luise. High-torque low-speed permanent magnet assisted synchronous reluctance motor design. In *2019 IEEE International Electric Machines Drives Conference (IEMDC)*, pages 644–649, May 2019.

[37] A. Castagnini, P. S. Termini, G. Secondo, and N. Bianchi. Replacing SPM by PMAREL machines in low-speed high-torque applications. In *2016 IEEE Energy Conversion Congress and Exposition (ECCE)*, pages 1–8, September 2016.

[38] N. Morimura, H. Suzuki, and M. Morishita. Single halbach field magnet desined from dual halbach field magnet for rotating machines. In *2018 21st International Conference on Electrical Machines and Systems (ICEMS)*, pages 27–30, October 2018.

[39] S. Alshibani. Application of particle swarm optimization in the design of halbach permanent magnet synchronous generators for megawatt level wind turbines. In *2018 7th International Conference on Renewable Energy Research and Applications (ICRERA)*, pages 865–868, October 2018.

[40] X. Liu, J. Qiu, H. Chen, X. Xu, Y. Wen, and P. Li. Design and optimization of an electromagnetic vibration energy harvester using dual halbach arrays. *IEEE Transactions on Magnetics*, 51(11):1–4, November 2015.

[41] J. Wang, G. W. Jewell, and D. Howe. Design optimisation and comparison of tubular permanent magnet machine topologies. *IEE Proceedings - Electric Power Applications*, 148(5):456–464, 2001.

[42] Z. Q. Zhu and D. Howe. Halbach permanent magnet machines and applications: a review. *IEE Proceedings - Electric Power Applications*, 148(4):299–308, 2001.

[43] Helena A. Khazdozian, Ravi L. Hadimani, and David C. Jiles. Development of rare earth free permanent magnet generator using halbach cylinder rotor design. *Renewable Energy*, 112:84–92, November 2017.

[44] Q. Wu, K. Lu, P. O. Rasmussen, and K. F. Rasmussen. A new application and experimental validation of moulding technology for ferrite magnet assisted synchronous reluctance machine. In *2016 IEEE Energy Conversion Congress and Exposition (ECCE)*, pages 1–8, September 2016.

[45] M. M. Rahman, K. Kim, and J. Hur. Design and optimization of neodymium-free spoke-type motor with segmented wing-shaped pm. *IEEE Transactions on Magnetics*, 50(2):865–868, February 2014.

[46] Y. Shen and Z. Q. Zhu. Analysis of electromagnetic performance of halbach pm brushless machines having mixed grade and unequal height of magnets. *IEEE Transactions on Magnetics*, 49(4):1461–1469, April 2013.

[47] G. Liu, M. Shao, W. Zhao, Q. Chen, and L. Mo. Cost reduction of a new fault-tolerant halbach permanent magnet machine using ferrite magnet. *IEEE Transactions on Magnetics*, 50(11):1–4, November 2014.

[48] M. Galea, Z. Xu, C. Tighe, T. Hamiti, C. Gerada, and S. Pickering. Development of an aircraft wheel actuator for green taxiing. In *2014 International Conference on Electrical Machines (ICEM)*, pages 2492–2498, 2014.

[49] M. Galea, T. Hamiti, and C. Gerada. Torque density improvements for high performance machines. In *2013 International Electric Machines Drives Conference*, pages 1066–1073, 2013.

[50] H. Tahanian, M. Aliahmadi, and J. Faiz. Ferrite permanent magnets in electrical machines: Opportunities and challenges of a non-rare-earth alternative. *IEEE Transactions on Magnetics*, 56(3):1–20, 2020.

[51] World energy resources, 2013.

[52] A. T. de Almeida, F. J. T. E. Ferreira, and G. Baoming. Beyond induction motors—technology trends to move up efficiency. *IEEE Transactions on Industry Applications*, 50(3):2103–2114, May 2014.

[53] Council of European Union. Council regulation (EU) no 640/2009, 2009. https://eur-lex.europa.eu/legal-content/EN/TXT/PDF/?uri=CELEX:32009R0640&from=EN.

[54] Council of European Union. Council regulation (EU) no 2019/1781, 2019. https://eur-lex.europa.eu/legal-content/EN/TXT/PDF/?uri=CELEX:32019R1781&from=EN.

[55] X. Lu, K. L. V. Iyer, K. Mukherjee, and N. C. Kar. Development of a novel magnetic circuit model for design of premium efficiency three-phase line start permanent magnet machines with improved starting performance. *IEEE Transactions on Magnetics*, 49(7):3965–3968, 2013.

[56] J. Lee, S. Rhyu, I. Jung, and Y. Kim. Design of high efficiency line start permanent magnet motor for submersible pumps. In *2016 IEEE 16th International Conference on Environment and Electrical Engineering (EEEIC)*, pages 1–4, 2016.

[57] M. Villani, M. Santececca, and F. Parasiliti. High-efficiency line-start synchronous reluctance motor for fan and pump applications. In *2018 XIII International Conference on Electrical Machines (ICEM)*, pages 2178–2184, 2018.

[58] H. Liu and J. Lee. Optimum design of an ie4 line-start synchronous reluctance motor considering manufacturing process loss effect. *IEEE Transactions on Industrial Electronics*, 65(4):3104–3114, 2018.

[59] R. T. Ugale, A. Bhanuji, and B. N. Chaudhari. A novel line start permanent magnet synchronous motor using two-part rotor. In *TENCON 2009 - 2009 IEEE Region 10 Conference*, pages 1–5, 2009.

[60] M. Lin, D. Li, X. Ren, K. Xie, and R. Qu. Dual-stator line-start vernier permanent magnet synchronous machine. In *2019 IEEE International Electric Machines Drives Conference (IEMDC)*, pages 2239–2244, 2019.

[61] B. Poudel, E. Amiri, and P. Rastgoufard. Design and analysis of line start synchronous reluctance motor with dual saliency. In *2018 IEEE Transportation Electrification Conference and Expo (ITEC)*, pages 385–388, 2018.

[62] Mineral commodity summaries 2015, January 2015.

[63] Mineral commodity summaries 2020, January 2020.

[64] Xibo Wang, Yalin Lei, Jianping Ge, and Sanmang Wu. Production forecast of chinas rare earths based on the generalized weng model and policy recommendations. *Resources Policy*, 43, 03 2015.

[65] B. D. Cullity. *Introduction to Magnetic Materials*. Wiley-IEEE Press, December 2008.

[66] Alex Goldman. *Handbook of Modern Ferromagnetic Materials*. Springer US, 1999.

[67] O Gutfleisch. Controlling the properties of high energy density permanent magnetic materials by different processing routes. *Journal of Physics D: Applied Physics*, 33(17):R157–R172, August 2000.

[68] J. M. D. Coey. Hard magnetic materials: A perspective. *IEEE Transactions on Magnetics*, 47(12):4671–4681, December 2011.

[69] Rollin J. Parker and Robert J. Studders. *Permanent Magnets and Their Application*. John Wiley and Sons, 1962.

[70] PZK Brno a.s. Ferrite permanent magnets. Available at https://www.pzk-magnets.com/ferrite-permanent-magnets.

[71] Adams Magnetic Products Co. Magnetic products for engineering performance, innovation and design. Available at https://www.adamsmagnetic.com/sites/default/files/Adams-Materials-Catalog.pdf.

[72] Ltd. Hitachi Metals. Permanent magnets. Available at http://www.hitachi-metals.co.jp/e/products/auto/el/pdf/hg-a27-j.pdf.

[73] PZK Brno a.s. AlNiCo permanent magnets. Available at https://www.pzk-magnets.com/alnico-permanent-magnets.

[74] PZK Brno a.s. SmCo permanent magnets. Available at https://www.pzk-magnets.com/ferrite-permanent-magnets.

[75] Advanced Magnet Source Corp. Neodymium NdFeB magnets disks - advanced magnet source. Available at https://advancedmagnetsource.com/neodymium-ndfeb-magnets-disks/.

[76] IMA Magnets UK. AlNiCo permanent magnets. Available at https://www.imamagnets.com/en/blog/uses-applications-alnico-magnets/,.

[77] Ltd. Hitachi Metals. Alnico. Available at https://www.hitachimetals.com/materials-products/permanent-magnets/alnico.php.

[78] Eclipse Magnetics Ltd. Alnico. Available at https://www.eclipsemagnetics.com/media/wysiwyg/datasheets/magnet_materials_and_assemblies/alnico_magnets_datasheet_rev2.pdf.

[79] Eclipse Magnetics Ltd. Samarium cobalt SmCo. Available at https://www.eclipsemagnetics.com/row/magnetic-materials-samarium-cobalt-smco/.

[80] Arnold Magnetic Technologies. Samarium cobalt SmCo - RECOMA. Available at https://www.arnoldmagnetics.com/wp-content/uploads/2017/10/Recoma-35E-160205-final.pdf.

[81] P. Giangrande, A. Al-Timimy, A. Galassini, S. Papadopoulos, M. Degano, and M. Galea. Design of PMSM for EMA employed in secondary flight control systems. In *2018 IEEE International Conference on Electrical Systems for Aircraft, Railway, Ship Propulsion and Road Vehicles International Transportation Electrification Conference (ESARS-ITEC)*, pages 1–6, 2018.

[82] H. Lin, H. Guo, and H. Qian. Design of high-performance permanent magnet synchronous motor for electric aircraft propulsion. In *2018 21st International Conference on Electrical Machines and Systems (ICEMS)*, pages 174–179, 2018.

[83] Arnold Magnetic Technologies. Samarium cobalt SmCo. Available at https://www.arnoldmagnetics.com/products/recoma-samarium-cobalt-magnets/.

[84] Eclipse Magnetics Ltd. Ndfeb magnets/neodymium iron boron magnets datasheet. Available at https://www.eclipsemagnetics.com/media/wysiwyg/datasheets/magnet_materials_and_assemblies/ndfeb_neodymium_iron_boron-standard_ndfeb_range_datasheet_rev1.pdf.

[85] Arnold Magnetic Technologies. Neodymium iron boron magnet catalog. Available at https://www.arnoldmagnetics.com/wp-content/uploads/2019/06/Arnold-Neo-Catalog.pdf.

[86] M. Barcaro and N. Bianchi. Interior PM machines using ferrite to replace rare-earth surface PM machines. *IEEE Transactions on Industry Applications*, 50(2):979–985, March 2014.

[87] Mahnaz Amiri, Masoud Salavati-Niasari, and Ahmad Akbari. Magnetic nanocarriers: Evolution of spinel ferrites for medical applications. *Advances in Colloid and Interface Science*, 265:29–44, 2019.

[88] Mohammad Nur-E-Alam, Mikhail Vasiliev, Vladimir Belotelov, and Kamal Alameh. Properties of ferrite garnet (bi, lu, y)3(fe, ga)5o12 thin film materials prepared by RF magnetron sputtering. *Nanomaterials*, 8(5):355, May 2018.

[89] Majid [Niaz Akhtar], Muhammad [Azhar Khan], Mukhtar Ahmad, G. Murtaza, Rizwan Raza, S.F. Shaukat, M.H. Asif, Nadeem Nasir, Ghazanfar Abbas, M.S. Nazir, and M.R. Raza. Y3fe5o12 nanoparticulate garnet ferrites: Comprehensive study on the synthesis and characterization fabricated by various routes. *Journal of Magnetism and Magnetic Materials*, 368:393–400, 2014.

[90] Robert C. Pullar. Hexagonal ferrites: A review of the synthesis, properties and applications of hexaferrite ceramics. *Progress in Materials Science*, 57(7):1191–1334, 2012.

[91] Poorva Sharma, R. Masrour, A. Jabar, Jiyu Fan, Ashwini Kumar, Langsheng Ling, Chunlan Ma, Caixia Wang, and Hao Yang. Structural and magnetocaloric properties of rare-earth orthoferrite perovskite: Tmfeo3. *Chemical Physics Letters*, 740:137057, 2020.

[92] Ümit Özgür, Yahya Alivov, and Hadis Morkoç. Microwave ferrites, part 1: fundamental properties. *Journal of Materials Science: Materials in Electronics*, 20(9):789–834, June 2009.

[93] Robert C. Pullar. Hexagonal ferrites: A review of the synthesis, properties and applications of hexaferrite ceramics. *Progress in Materials Science*, 57(7):1191–1334, September 2012.

[94] A. Cochardt. Recent ferrite magnet developments. *Journal of Applied Physics*, 37(3):1112–1115, March 1966.

[95] V. Adelskold. X-ray studies on magneto-plumbite, pbo6fe2o3, and other substances resembling "beta-alumina", na2o11al2o3. *Ark. Kem. Mineral. Geol*, 12A-29, 1938.

[96] PA USA International Centre for Diffraction Data, Newton Square. Pdf no. 84-1531 (srfe 12 o 19), 84-757 (bafe 12 o 19), 84-2046 (pbfe 12 o 19).

[97] J. Dufour, R. Latorre, C. Negro, E.M. Alcalá, A. Formoso, and F. López-Mateos. Protocol for the synthesis of ba-hexaferrites with prefixed coercivities. *Journal of Magnetism and Magnetic Materials*, 172(3):308–316, August 1997.

[98] J. Dufour, R. Latorre, E.M. Alcalá, C. Negro, A. Formoso, and F. López-Mateos. Synthesis of m-type hexaferrites from steel pickling liquors (ID 109). *Journal of Magnetism and Magnetic Materials*, 157-158:125–126, May 1996.

[99] W. A. Kaczmarek and B. W. Ninham. Application of mechanochemistry in ferrite materials technology. *Le Journal de Physique IV*, 07(C1):C1–47–C1–48, March 1997.

[100] O ABE. Mechanochemically assisted preparation process of barium hexaferrite powders. *Solid State Ionics*, 101-103:103–109, November 1997.

[101] Takashi Yamaguchi. *Ferrites : proceedings of the ICF 6 : main conference, Sept. 29-Oct. 2, 1992, Tokyo, Japan, sattellite conference, Oct. 5-Oct. 7, 1992, Kyoto, Japan*. Japan Society of Powder and Powder Metallurgy, Place of publication not identified, 1992.

[102] J. Dufour, R. Latorre, C. Negro, E.M. Alcalá, A. Formoso, and F. López-Mateos. Protocol for the synthesis of ba-hexaferrites with prefixed coercivities. *Journal of Magnetism and Magnetic Materials*, 172(3):308–316, August 1997.

[103] U. KREIBIG. ANOMALOUS FREQUENCY AND TEMPERATURE DEPENDENCE OF THE OPTICAL ABSORPTION OF SMALL GOLD PARTICLES. *Le Journal de Physique Colloques*, 38(C2):C2–97–C2–103, July 1977.

[104] B. T. Shirk and W. R. Buessem. Temperature dependence of ms and k1 of BaFe12o19 and SrFe12o19 single crystals. *Journal of Applied Physics*, 40(3):1294–1296, March 1969.

[105] T. Takabatake, F. Iga, T. Yoshino, Y. Echizen, K. Katoh, K. Kobayashi, M. Higa, N. Shimizu, Y. Bando, G. Nakamoto, H. Fujii, K. Izawa, T. Suzuki, T. Fujita, M. Sera, M. Hiroi, K. Maezawa, S. Mock, H.v. Löhneysen, A. Brückl, K. Neumaier, and K. Andres. Ce- and yb-based kondo semiconductors. *Journal of Magnetism and Magnetic Materials*, 177-181:277–282, January 1998.

[106] R.C Pullar, M.D Taylor, and A.K Bhattacharya. A halide free route to the manufacture of microstructurally improved m ferrite (BaFe12o19 and SrFe12o19) fibres. *Journal of the European Ceramic Society*, 22(12):2039–2045, November 2002.

[107] H. Yamamoto, H. Kumehara, R. Takeuchi, and H. Nishio. Magnetic properties of sr-m ferrite fine particles. *Le Journal de Physique IV*, 07(C1):C1–535–C1–536, March 1997.

[108] H. Taguchi, T. Takeishi, K. Suwa, K. Masuzawa, and Y. Minachi. High energy ferrite magnets. *Le Journal de Physique IV*, 07(C1):C1–311–C1–312, March 1997.

[109] TDK. Ferrite magnets summary. Online, May 2014. Online.

[110] J. K. Kostko. Polyphase reaction synchronous motors. *Journal of the American Institute of Electrical Engineers*, 42(11):1162–1168, November 1923.

[111] Reza Rajabi Moghaddam. *Synchronous reluctance machine (SynRM) in variable speed drives (VSD) applications*. Electrical Engineering, KTH Royal Institute of Technology, 2011.

[112] G. Bacco and N. Bianchi. Design criteria of flux-barriers in synchronous reluctance machines. *IEEE Transactions on Industry Applications*, pages 1–1, 2018.

[113] C. Lopez-Torres, G. Bacco, N. Bianchi, A. G. Espinosa, and L. Romeral. A parallel analytical computation of synchronous reluctance machine. In *2018 XIII International Conference on Electrical Machines (ICEM)*, pages 25–31, September 2018.

[114] L. Knebl, J. Barta, and C. Ondrusek. An improved nonlinear analytical model of the PM-assisted synchronous reluctance motor focused on torque behavior accuracy. In *2018 XIII International Conference on Electrical Machines (ICEM)*, pages 541–546, September 2018.

[115] Knebl Ladislav. Design of synchronous reluctance machine with permanent magnets. Master's thesis, BUT, 2017.

[116] L. Knebl, C. Ondrusek, and J. Kurfürst. Ferrite assisted synchronous reluctance motor design, manufacturing and material influence on motor characteristics. In *2018 18th International Conference on Mechatronics - Mechatronika (ME)*, pages 1–6, December 2018.

[117] Jordi-Roger Riba, Carlos López-Torres, Luís Romeral, and Antoni Garcia. Rare-earth-free propulsion motors for electric vehicles: A technology review. *Renewable and Sustainable Energy Reviews*, 57:367–379, May 2016.

[118] B. Ban, S. Stipetić, and M. Klanac. Synchronous reluctance machines: Theory, design and the potential use in traction applications. In *2019 International Conference on Electrical Drives Power Electronics (EDPE)*, pages 177–188, 2019.

[119] J. Li, M. Xin, Z. Fan, and R. Liu. Design and experimental evaluation of a 12 kw large synchronous reluctance motor and control system for elevator traction. *IEEE Access*, 8:34256–34264, 2020.

[120] S. M. de Pancorbo, G. Ugalde, J. Poza, and A. Egea. Comparative study between induction motor and synchronous reluctance motor for electrical railway traction applications. In *2015 5th International Electric Drives Production Conference (EDPC)*, pages 1–5, 2015.

[121] A. D. Chernyshev, T. A. Lisovskaya, and R. A. Lisovskiy. Comparative analysis of different electrical motor types as a traction drive part in electrical transmission. In *2017 International Conference on Industrial Engineering, Applications and Manufacturing (ICIEAM)*, pages 1–5, 2017.

[122] F. N. Jurca, M. Ruba, and C. Marţiş. Design and control of synchronous reluctances motors for electric traction vehicle. In *2016 International Symposium on Power Electronics, Electrical Drives, Automation and Motion (SPEEDAM)*, pages 1144–1148, 2016.

[123] C. P. Riley, N. P. Sawant, D. Ilea, A. Venskus, A. M. Bedford, A. M. Michaelides, X. Vinamata, P. J. Topping, J. M. Soler-Vizan, E. Odvarka, J. D. Wale, D. J. Hawke, and J. M. Reeve. Simulation based design of reluctance motors for traction applications in hybrid and electric vehicles. In *7th IET International Conference on Power Electronics, Machines and Drives (PEMD 2014)*, pages 1–6, 2014.

[124] N. Bianchi, S. Bolognani, E. Carraro, M. Castiello, and E. Fornasiero. Electric vehicle traction based on synchronous reluctance motors. *IEEE Transactions on Industry Applications*, 52(6):4762–4769, 2016.

[125] F. N. Jurca, R. Mircea, C. Martis, R. Martis, and P. P. Florin. Synchronous reluctance motors for small electric traction vehicle. In *2014 International Conference and Exposition on Electrical and Power Engineering (EPE)*, pages 317–321, 2014.

[126] K. Grace, S. Galioto, K. Bodla, and A. El-Refaie. Carbon-fiber-wrapped synchronous reluctance traction motor. In *2017 IEEE Energy Conversion Congress and Exposition (ECCE)*, pages 3913–3920, 2017.

[127] M. Obata, S. Morimoto, M. Sanada, and Y. Inoue. Performance of pmasynrm with ferrite magnets for ev/hev applications considering productivity. *IEEE Transactions on Industry Applications*, 50(4):2427–2435, 2014.

[128] H. Cai, B. Guan, and L. Xu. Low-cost ferrite pm-assisted synchronous reluctance machine for electric vehicles. *IEEE Transactions on Industrial Electronics*, 61(10):5741–5748, 2014.

[129] Masayuki Sanada, Yukinori Inoue, and Shigeo Morimoto. Structure and characteristics of high-performance pmasynrm with ferrite magnets. *IEEJ Transactions on Industry Applications*, 131:1401–1407, 01 2011.

[130] Xiping Liu, Ya Li, and Zhangqi Liu. Performance evaluation of a permanent magnet-assisted synchronous reluctance machine with hybrid magnets of ferrite magnets and rare-earth PMs. January 2017.

[131] S. Ooi, S. Morimoto, M. Sanada, and Y. Inoue. Performance evaluation of a high-power-density pmasynrm with ferrite magnets. *IEEE Transactions on Industry Applications*, 49(3):1308–1315, 2013.

[132] Wei Dai and Daniel Berleant. Benchmarking contemporary deep learning hardware and frameworks: A survey of qualitative metrics. In *2019 IEEE First International Conference on Cognitive Machine Intelligence (CogMI)*. IEEE, December 2019.

[133] Randy Haupt. *Practical genetic algorithms*. John Wiley, Hoboken, N.J, 2004.

[134] Ivan Zelinka. *Evolucni vypocetni techniky: principy a aplikace*. BEN - technicka literatura, 2009.

[135] Kalyanmoy Deb. *Multi-objective optimization using evolutionary algorithms*. John Wiley & Sons, Chichester New York, 2001.

[136] Julia Roberts & Mykel Kochenderfer. Penalty functions. https://web.stanford.edu/group/sisl/k12/optimization/MO-unit5-pdfs/5.6penaltyfunctions.pdf.

[137] Jiri Kurfürst. *Optimalizace stroje s permanentními magnety na rotoru pomocí umělé inteligence*. PhD thesis, Brno University of Technology, 2012.

[138] K. Deb, A. Pratap, S. Agarwal, and T. Meyarivan. A fast and elitist multiobjective genetic algorithm: Nsga-ii. *IEEE Transactions on Evolutionary Computation*, 6(2):182–197, 2002.

[139] David Goldberg. *Genetic algorithms in search, optimization, and machine learning*. Addison-Wesley Publishing Company, Reading, Mass, 1989.

[140] Donald Davendra and Ivan Zelinka. *Self-Organizing Migrating Algorithm: Methodology and Implementation*, volume 626. 01 2016.

[141] Chengfu Sun. An improved differential evolution and novel crowding distance metric for multi-objective optimization. In *2010 Third International Symposium on Knowledge Acquisition and Modeling*, pages 265–268, 2010.

[142] J. Zhang and H. Li. A global-crowding-distance based multi-objective particle swarm optimization algorithm. In *2014 Tenth International Conference on Computational Intelligence and Security*, pages 1–6, 2014.

[143] K. Deb and H. Jain. An evolutionary many-objective optimization algorithm using reference-point-based nondominated sorting approach, part i: Solving problems with box constraints. *IEEE Transactions on Evolutionary Computation*, 18(4):577–601, 2014.

[144] F. E. Curtis and K. Scheinberg. Adaptive stochastic optimization: A framework for analyzing stochastic optimization algorithms. *IEEE Signal Processing Magazine*, 37(5):32–42, 2020.

[145] A. Pal, L. Zhu, Y. Wang, and G. G. Zhu. Multi-objective stochastic bayesian optimization for iterative engine calibration*. In *2020 American Control Conference (ACC)*, pages 4893–4898, 2020.

[146] F. Gao and G. B. Sheble. Stochastic optimization techniques for economic dispatch with combined cycle units. In *2006 International Conference on Probabilistic Methods Applied to Power Systems*, pages 1–8, 2006.

[147] Lauren Hannah. Lecture notes in computational statistics, April 2014.

[148] Kurt Marti. Stochastic optimization methods. In *Stochastic Optimization Methods*, pages 1–35. Springer Berlin Heidelberg, 2015.

[149] Maurice Clerc. *Particle swarm optimization*. ISTE, London Newport Beach, 2006.

[150] James Kennedy and Russell Eberhart. Particle swarm optimization. In *Proceedings of ICNN'95-International Conference on Neural Networks*, volume 4, pages 1942–1948. IEEE, 1995.

[151] Bruno Seixas Gomes de Almeida and Victor Coppo Leite. Particle swarm optimization: A powerful technique for solving engineering problems. In *Swarm Intelligence - Recent Advances, New Perspectives and Applications*. IntechOpen, December 2019.

[152] Bernell K. Stone. A linear programming formulation of the general portfolio selection problem. *The Journal of Financial and Quantitative Analysis*, 8(4):621, September 1973.

[153] Christodoulos A. Floudas. Global optimization in design and control of chemical process systems. *Journal of Process Control*, 10(2-3):125–134, April 2000.

[154] E. Sandgren. Nonlinear integer and discrete programming in mechanical design optimization. *Journal of Mechanical Design*, 112(2):223–229, June 1990.

[155] Hill climbing algorithm in ai - javatpoint.

[156] Bowei Xi, Zhen Liu, Mukund Raghavachari, Cathy H. Xia, and Li Zhang. A smart hill-climbing algorithm for application server configuration. In *Proceedings of the 13th conference on World Wide Web - WWW '04*. ACM Press, 2004.

[157] Mona Fronita, Rahmat Gernowo, and Vincencius Gunawan. Comparison of genetic algorithm and hill climbing for shortest path optimization mapping. *E3S Web of Conferences*, 31:11017, 2018.

[158] Andrés Cano, Manuel Gómez, Serafín Moral, and Joaquín Abellán. Hill-climbing and branch-and-bound algorithms for exact and approximate inference in credal networks. *International Journal of Approximate Reasoning*, 44(3):261–280, March 2007.

[159] G. Bramerdorfer, A. Zăvoianu, S. Silber, E. Lughofer, and W. Amrhein. Possibilities for speeding up the fe-based optimization of electrical machines—a case study. *IEEE Transactions on Industry Applications*, 52(6):4668–4677, 2016.

[160] G. Bramerdorfer and A. Zăvoianu. Surrogate-based multi-objective optimization of electrical machine designs facilitating tolerance analysis. *IEEE Transactions on Magnetics*, 53(8):1–11, 2017.

[161] Oliver Kramer. *Genetic algorithm essentials*. Springer, Cham, Switzerland, 2017.

[162] John Holland. *Adaptation in natural and artificial systems : an introductory analysis with applications to biology, control, and artificial intelligence*. MIT Press, Cambridge, Mass, 1992.

[163] Rudy Clausen, Emmanuel Sapin, Kenneth A. De Jong, and Amarda Shehu. Evolution strategies for exploring protein energy landscapes. In *Proceedings of the 2015 Annual Conference on Genetic and Evolutionary Computation*, GECCO '15, page 217–224, New York, NY, USA, 2015. Association for Computing Machinery.

[164] Sebastian HØlt Bak, Nina Rask, and Sebastian Risi. Towards adaptive evolutionary architecture. In *Proceedings of the 5th International Conference on Evolutionary and Biologically Inspired Music, Sound, Art and Design - Volume 9596*, page 47–62, Berlin, Heidelberg, 2016. Springer-Verlag.

[165] Mateus A. M. Teixeira, Fillipe Goulart, and F. Campelo. Evolutionary multiobjective optimization of winglets. In *GECCO '16*, 2016.

[166] F. R. Ismagilov, V. Y. Vavilov, and V. V. Ayguzina. Genetic algorithms for electrical machine optimal design. In *2018 International Conference on Industrial Engineering, Applications and Manufacturing (ICIEAM)*, pages 1–6, 2018.

[167] Gregory Morse and Kenneth O. Stanley. Simple evolutionary optimization can rival stochastic gradient descent in neural networks. In *Proceedings of the Genetic and Evolutionary Computation Conference 2016*, GECCO '16, page 477–484, New York, NY, USA, 2016. Association for Computing Machinery.

[168] Charles Darwin. *On the origin of species by means of natural selection, or, The preservation of favoured races in the struggle for life*. London :John Murray, Albemarle Street,, 1859.

[169] Yong Deng, Yang Liu, and Deyun Zhou. An improved genetic algorithm with initial population strategy for symmetric TSP. *Mathematical Problems in Engineering*, 2015:1–6, 2015.

[170] Royad Parvez. Selection in evolutionary algorithm.

[171] Gilbert Syswerda. Simulated crossover in genetic algorithms. In L. DARRELL WHITLEY, editor, *Foundations of Genetic Algorithms*, volume 2 of *Foundations of Genetic Algorithms*, pages 239–255. Elsevier, 1993.

[172] Eckart Zitzler, Marco Laumanns, and Lothar Thiele. Spea2: Improving the strength pareto evolutionary algorithm. 2001.

[173] Filip Rudzinski. Finding sets of non-dominated solutions with high spread and well-balanced distribution using generalized strength pareto evolutionary algorithm. In *Proceedings of the 2015 Conference of the International Fuzzy Systems Association and the European Society for Fuzzy Logic and Technology*. Atlantis Press, 2015.

[174] N. David and M. Lubomír. Self - organizing migrating algorithm used to control a semi-batch chemical reactor. In *2013 13th International Conference on Control, Automation and Systems (ICCAS 2013)*, pages 1266–1269, 2013.

[175] P. Varacha and I. Zelinka. Analytic programming powered by distributed self-organizing migrating algorithm application. In *2008 7th Computer Information Systems and Industrial Management Applications*, pages 99–100, 2008.

[176] J. Kurfürst, J. Duroň, M. Skalka, M. Janda, and Č. Ondrůšek. Magnet shape optimization of brushless machine by self-organizing migrating algorithm. In *2011 International Conference on Power Engineering, Energy and Electrical Drives*, pages 1–5, 2011.

[177] Q. B. Diep. Self-organizing migrating algorithm team to team adaptive – SOMA T3A. In *2019 IEEE Congress on Evolutionary Computation (CEC)*, pages 1182–1187, 2019.

[178] T. Kadavy, M. Pluhacek, R. Senkerik, and A. Viktorin. Introducing self-adaptive parameters to self-organizing migrating algorithm. In *2019 IEEE Congress on Evolutionary Computation (CEC)*, pages 2908–2914, 2019.

[179] Poonam Garg. A comparison between memetic algorithm and genetic algorithm for the cryptanalysis of simplified data encryption standard algorithm. 2009.

[180] P. Kadlec and Z. Raida. Multi-objective self-organizing migrating algorithm applied to the design of electromagnetic components. *IEEE Antennas and Propagation Magazine*, 55(6):50–68, 2013.

[181] P. Kadlec and Z. Raida. Comparison of novel multi-objective self organizing migrating algorithm with conventional methods. In *Proceedings of 21st International Conference Radioelektronika 2011*, pages 1–4, 2011.

[182] K. Wang, Z. Q. Zhu, G. Ombach, M. Koch, S. Zhang, and J. Xu. Optimal slot/pole and flux-barrier layer number combinations for synchronous reluctance machines. In *2013 Eighth International Conference and Exhibition on Ecological Vehicles and Renewable Energies (EVER)*, pages 1–8, 2013.

[183] Jian Gao, Yanan Yu, and Shoudao Huang. Winding layers and slot/pole combination in fractional slot/pole pmsm—effects on motor performance. In *2009 International Conference on Electrical Machines and Systems*, pages 1–4, 2009.

[184] L. Knebl, C. Ondrusek, J. Barta, and O. Vitek. High-torque ferrite assisted reluctance machine winding comparison. In *2020 International Conference on Electrical Machines (ICEM)*, volume 1, pages 1567–1572, 2020.

[185] L. Alberti, M. Barcaro, and N. Bianchi. Design of a low-torque-ripple fractional-slot interior permanent-magnet motor. *IEEE Transactions on Industry Applications*, 50(3):1801–1808, May 2014.

[186] L. Knebl, C. Ondrusek, and J. Kurfürst. Ferrite assisted synchronous reluctance motor design, manufacturing and material influence on motor characteristics. In *2018 18th International Conference on Mechatronics - Mechatronika (ME)*, pages 1–6, December 2018.

[187] H. Murakami, Y. Honda, H. Kiriyama, S. Morimoto, and Y. Takeda. The performance comparison of SPMSM, IPMSM and SynRM in use as air-conditioning compressor. In

Conference Record of the 1999 IEEE Industry Applications Conference. Thirty-Forth IAS Annual Meeting (Cat. No.99CH36370), volume 2, pages 840–845 vol.2, October 1999.

[188] E. Castagnaro, G. Bacco, and N. Bianchi. Impact of geometry on the rotor iron losses in synchronous reluctance motors. *IEEE Transactions on Industry Applications*, 55(6):5865–5872, November 2019.

[189] Y. Wang, G. Bacco, and N. Bianchi. Geometry analysis and optimization of PM-assisted reluctance motors. *IEEE Transactions on Industry Applications*, 53(5):4338–4347, September 2017.

[190] G. Bramerdorfer, S. Silber, G. Weidenholzer, and W. Amrhein. Comprehensive cost optimization study of high-efficiency brushless synchronous machines. In *2013 International Electric Machines Drives Conference*, pages 1126–1131, 2013.

[191] G. Bacco and N. Bianchi. Choice of flux-barriers position in synchronous reluctance machines. In *2017 IEEE Energy Conversion Congress and Exposition (ECCE)*, pages 1872–1879, 2017.

[192] Emetor web based analytical tool newly developed by royal institute of technology. Stockholm; http://www.emetor.org.

[193] Nicola Bianchi. *Electrical Machine Analysis Using Finite Elements*. CRC Press, Hoboken, 2005.

[194] Ladislav Knebl, Nicola Bianchi, Giacomo Bacco, and Cestmir Ondrusek. Synchronous reluctance motor analytical model cross-saturation and magnetization analysis. *Journal of Electrical Engineering & Technology*, 2019.

[195] W.L. Soong and N. Ertugrul. Inverterless high-power interior permanent-magnet automotive alternator. *IEEE Transactions on Industry Applications*, 40(4):1083–1091, July 2004.

[196] Pavel Ponomarev, Ilya Petrov, and Juha Pyrhonen. Influence of travelling current linkage harmonics on inductance variation, torque ripple and sensorless capability of tooth-coil permanent-magnet synchronous machines. *IEEE Transactions on Magnetics*, 50(1):1–8, January 2014.

[197] Gianmario Pellegrino, Thomas M. Jahns, Nicola Bianchi, Wen Soong, and Francesco Cupertino. *The Rediscovery of Synchronous Reluctance and Ferrite Permanent Magnet Motors*. Springer International Publishing, 2016.

[198] ISO Central Secretary. Systems and software engineering – Lifecycle profiles for Very Small Entities (VSEs) – Part 1: Overview. Standard ISO/IEC 60034, International Standard, Geneva, CH, 2016.

[199] Yokogawa Test and Measurement Corporation. *Power Analyzer Accuracy and Basic Uncertainty Calculator*. https://tmi.yokogawa.com/library/resources/faqs/power-analyzer-accuracy-and-basic-uncertainty-calculator/.